5-1999

Close Formation Flight Control

Andrew W. Proud

Recommended Citation

Proud, Andrew W., "Close Formation Flight Control" (1999). *Theses and Dissertations*. 5261.
https://scholar.afit.edu/etd/5261

AFIT/GE/ENG/99M-24

CLOSE FORMATION FLIGHT CONTROL

THESIS

Andrew W. Proud
Captain, USAF

AFIT/GE/ENG/99M-24

Approved for public release; distribution unlimited

19990413 104

AFIT/GE/ENG/99M-24

CLOSE FORMATION FLIGHT CONTROL

Andrew W. Proud, B.S. Electrical Engineering
Captain, USAF

Approved:

M. Pachter — March 5, 1999

Dr. Meir Pachter
Committee Chairman — Date

John J. D'Azzo — 3/5/99

Dr. John J D'Azzo
Committee Member — Date

AFIT/GE/ENG/99M-24

CLOSE FORMATION FLIGHT CONTROL

THESIS

Presented to the Faculty of the School of Engineering
of the Air Force Institute of Technology
Air University
In Partial Fulfillment of the
Requirements for the Degree of
Master of Science in Electrical Engineering

Andrew W. Proud, B.S. Electrical Engineering
Captain, USAF

March, 1999

Acknowledgements

I would like to thank God and His Son, my Lord and Saviour Jesus Christ, who has blessed me more than I deserve and made it possible for me to complete this work. By believing in Him, I obtained eternal life. By trusting in Him, I obtained peace and happiness. I am also grateful to my mom, Virginia, my brother Tim, and my sister Kim for their strength and encouragement during the rough times when schoolwork kept increasing, sleep kept decreasing and frustrations grew high. I would also like to thank my thesis advisor, Dr. Pachter for his direction and guidance. Many times I doubted him; not once did I prove him wrong, yet. I would also like to thank Dr. D'Azzo for his help in my follow on assignment search and my thesis. Finally, I would like to thank my classmates; without their help it would have been more difficult and not as much fun.

Andrew W. Proud

Table of Contents

Page

List of Figures

Figure Page

Figure Page

List of Tables

List of Symbols

Symbol	Page
τ_{ψ} heading time constant	2-1
τ_{v} velocity time constant	2-1
τ_{h} altitude time constant	2-2
$\dot{R}_{i}$ vector velocity in the i reference frame	2-7
$\dot{R}_{p}$ vector position as seen from the p reference frame	2-7
ω_{ip} vector angular velocity of p with respect to i	2-7
R_{p} vector position in the p reference frame	2-7
V_{WL}^{W} lead velocity with respect to the Wing aircraft	2-10
ω_{W}^{W} angular velocity of Wing	2-10
R_{WL}^{W} position of leader with respect to the Wing aircraft	2-10
V_{W}^{W} inertial velocity of the Wing aircraft	2-10
V_{L}^{W} inertial velocity of the Lead aircraft	2-10
ψ_{E} heading error	2-12
V_{L}^{L} velocity of lead aircraft	2-12
V_{WC} velocity command from PI controller	2-16
ψ_{WC} heading command from PI controller	2-16
h_{WC} altitude command from PI controller	2-16
Δx_{E} x error	2-16
Δy_{E} y error	2-16
Δz_{E} z error	2-16
K_{X_p} x channel proportional gain	2-16
K_{X_I} x channel integral gain	2-16
K_{Y_p} y channel proportional gain	2-16
K_{Y_I} y channel integral gain	2-16
K_{Z_p} altitude proportional gain	2-16

Symbol	Page
K_{Z_I} altitude integral gain	2-16
e_X longitudinal channel mixed error	2-17
k_V velocity error signal gain	2-17
k_x x separation error gain	2-17
e_Y lateral channel mixed error	2-17
k_ψ heading error signal gain	2-17
k_y y separation error gain	2-17
e_Z vertical channel error	2-17
k_z z separation error gain	2-17
$\vec{W}$ induced velocity	3-2
Γ vortex strength per unit length	3-2
r_c distance from filament to point	3-2
b wingspan	3-2
b' corrected wingspan	3-3
$\hat{y}$ y unit vector	3-4
$\hat{z}$ z unit vector	3-4
$\bar{W}_{UW}$ Total Induced Upwash	3-4
$\bar{x}$ nominal separation distance in the $\hat{x}$ direction	3-4
$\bar{y}$ nominal separation distance in the $\hat{y}$ direction	3-4
$\bar{z}$ nominal separation distance in the $\hat{z}$ direction	3-4
$\bar{V}_{SW}$ Total Induced Sidewash	3-4
$\bar{V}_{SW_{avg}}$ Average Induced Sidewash	3-5
$y' \equiv \frac{\bar{y}}{b}$ Non-dimensional y	3-6
$z' \equiv \frac{\bar{z}}{b}$ Non-dimensional z	3-6
ΔD_W Change in Drag	3-6
$\bar{q}$ Dynamic pressure	3-7
S Surface Area of Wing	3-7

Symbol Page

AFIT/GE/ENG/99M-24

Abstract

In this research the close formation flight control problem is addressed. The formation consists of a lead and wing aircraft, where the wing flies in close formation with the lead, such that the lead's vortices produce aerodynamic coupling effects, and a reduction in the formation's drag is achieved. A controller, i.e., a formation-hold autopilot for the wing aircraft, is designed such that the formation's geometry is maintained in the face of lead aircraft maneuvers. In the formation flight control system, the wing and lead aircraft dynamics are coupled due to kinematic effects, and, in the case of close formations, additional aerodynamic coupling effects are introduced. In the research these additional aerodynamic coupling effects are properly modeled. The most significant aerodynamic coupling effect introduced by close formation flight entails the coupling of the lateral/directional channel into the altitude-hold autopilot channel. It is shown that formation hold autopilots designed ignoring the aerodynamic coupling effects, yield satisfactory performance in close formation flight.

CLOSE FORMATION FLIGHT CONTROL

I. Introduction

1.1 Overview of Thesis

The introduction and review of previous research related to this subject are discussed in Chapter I. The equations of motion describing the kinematics between the aircraft in the formation as well as the flight control system equations for the aircraft are provided in Chapter II. The derivation of the Lead aircraft's effects on the Wing aircraft is developed in Chapter III. This includes derivations for upwash and sidewash effects caused by the Lead's wing vortex on the Wing aircraft and the development of the modified Wing aircraft flight control system. In Chapter IV the close formation flight controller along with the complete simulation model is developed. An analysis of stability and robustness is presented. Simulations are conducted and a performance evaluation of results is presented in Chapter V. Analysis, conclusions, and recommendations for further research are presented in Chapter VI.

1.2 Background

Previous research has been performed by several AFIT graduate students on the subject of formation flight control [1] - [12]. The motivation for their work was based primarily on the needs of special operations forces (SOF). SOF missions require pilots to fly many hours over long distances in a large formation usually in the dark at low altitudes and at times in poor weather. These flying requirements combined with the complexities of todays modern aircraft are very stressful and can lead to pilot saturation. A second motivation for this research was the need to fly multiple unmanned aerial vehicles (UAV) in a formation. These UAVs may be flying a surveillance mission or patroling a no-fly zone. Current UAVs are limited in the number of payloads they can carry at one time. This makes it necessary to fly multiple UAVs to obtain a complete set of data. A formation controller offers two potential benefits. First, if used for close formations, it can reduce fuel consumption of the formation; secondly, it can keep the aircraft in a known position with respect to each other, making correlation of data easier for fusion from multiple sensor payloads in multiple UAVs. In general, this could also help any formation of aircraft flying long distances.

In previous work, the formation flight control problem was introduced and attention was given to the kinematic coupling effects-see, e.g., [1]-[12]. Multiple versions of formation flight controllers were designed and developed. These controllers consisted of both feedback and feedforward designs as well as energy conserving designs. Simulations demonstrated that these controllers work well for large formations in which the separations are more than a wingspan. However, they were not designed for close formations, in which the lateral separation between aircraft is less than a wingspan.

1.3 Problem Statement

An aircraft while flying causes spiral like disturbances in the air. Two disturbances are projected backward perpendicular to it's wing and one is parallel to the wing. The spiral disturbances are cylindrical in shape and dissipate slowly over time. The air in the disturbances flows in a circular pattern starting at the tip of the wing, flowing up circularly towards the body of the aircraft and continuing to circularly flow down back to the wing tip. This leads to a clockwise flow in the disturbance created by the left wing and a counter-clockwise flow from the disturbance created by the right wing, as observed from behind. These disturbances created by the wing of the aircraft are often called a horseshoe vortex, see Figure 1.1. The air flow directly between the two disturbances is almost purely downwash. The flow of the air on the outside of the horseshoe vortex is a mixture of upwash and sidewash. Aircraft flying into a vortex created by another aircraft can experience substantial aerodynamic forces. The FAA has even developed a separation criteria to reduce the danger of accidents from other aircraft flying into the wake caused by aircraft landing and taking off [16].

Prandtl, a German scientist was one of the first to analyze the effects of these vortices on other aircraft. It has been hypothesized that geese fly in their inverted 'V' formation to take advantage of the upwash created by the vortex from each leading goose. Another aircraft flying in the vortex can, if positioned correctly, experience a reduction in drag and an increase in lift [13]. Therefore, alternating aircraft in and out of the lead position can potentially increase the range and endurance of a formation of aircraft. The formation of the two aircraft is shown in Figure 1.2. The aircraft creating the vortex is the Lead and the aircraft flying behind and into the vortex is the Wing. Indeed, the vortex shed by the Lead aircraft induces an upwash on the Wing aircraft's wing, which is responsible for reducing the Wing's induced drag.

The difficulty in taking advantage of this upwash for drag reduction by another aircraft is the fact it requires very precise positioning with respect to the aircraft generating the vortex. There is a small cylindrical window with a radius of about ten percent of the wingspan in which a benefit can be achieved for the Wing aircraft [13]. However, these vortices have substantial force and the flight control system needs to be able to reject these disturbances and keep the aircraft stable and in the proper location.

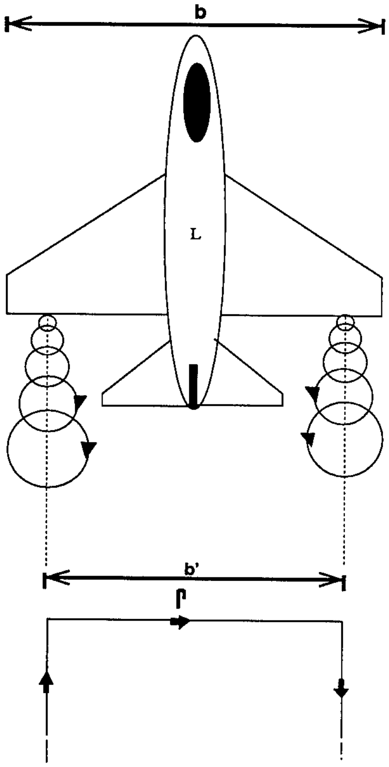

Figure 1.1 Horse Shoe Vortex

This thesis is a change in direction from the previous work on formation flight control. The main problem focus in this research is to analyze the effects of close formation flying on the wing aircraft's flight control system and develop a close formation flight controller robust enough to handle these effects and maintain the close formation. This will primarily include the need to analyze the vortex created by the Lead and determine its change in strength based on a change in position in the formation. Secondly, the necessary modifications to be applied to a formation flight control system to maintain a close formation during flight must be determined.

1.4 Research Objectives and Questions

The primary objective of this research is to apply a formation flight controller, previously developed for large formation, to this problem in which a close formation is required. Flight control system models previously developed will also be modified for use in this research.

The primary question to be answered from this work is, "can a close formation flight controller developed without due consideration of vortex effects control a close formation?". A secondary question is: "which is stronger, kinematic cross coupling or vortex aerodynamic cross coupling?".

1.5 Assumptions

There are ten main assumptions listed in order of development. These assumptions reduce the complexity and scope of the problem. This allows a focused study on the research objectives. These assumptions do not negate the reasonableness of the results achieved. An unlisted objective is to keep this research as realistic as possible. Hopefully, the results can be applied to the development of an actual formation flight controller for use in future aircraft and UAVs.

- Formation flight controller resides on Wing aircraft.
- Each aircraft is modeled as a point mass. This means that moment effects are not considered.

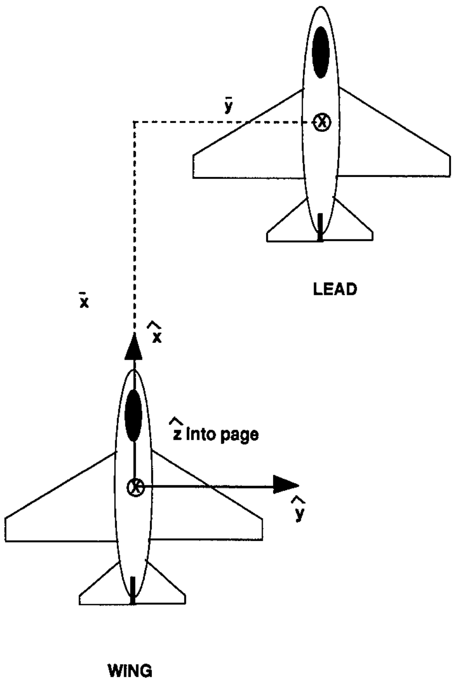

Figure 1.2 Formation Geometry

- The aircraft flight control system is assumed to be composed of three independent autopilots: Mach hold, heading hold, and altitude hold.
- Rotating coordinate frame is attached to the wing aircraft: $\hat{x}$ out the nose, $\hat{y}$ out the right wing, and $\hat{z}$ down, see Figure 1.2.
- A sensor capable of measuring the separation distances as well as the velocity, heading and altitude of the lead aircraft is attached to the wing aircraft.
- The Horseshoe vortex is modeled as two filaments originating near each wing tip and proceeding backward for an infinite distance. The magnitude of the parallel filament effect, that normally completes the horseshoe, is assumed to be negligible. These filaments are shown in Figure 1.1.
- The disturbances created by the Wing on the Lead are ignored.
- The Wing aircraft is assumed to be in the most "optimal" position. "Optimal" means that the Wing is in a position of maximum reduction in drag.

- The wing flight control system is trimmed for straight and level flight at this "optimal" position in the formation.
- The Lead maneuvering envelope is : +/- 30 degree heading change, +/- 50 ft/sec velocity change, and +/- 1000 ft altitude change.

1.6 Approach/Methodology

Systems developed by previous AFIT students are used as the building blocks for this research [11], [1], and [3]. These blocks include a Flight Control System (FCS) and Formation Flight Controller (FFC). The FCS model originally developed by Rohs [11] was a first order model based on C-130 aircraft models provided by Lockheed. Buzogany [1] developed a second order flight control system model through system identification techniques. This second order model was reduced from a fourteenth order model that was developed based on actual aircraft specifications provided by Lockheed. The complete flight control system used in this research is composed of the first order Heading hold autopilot developed by Rohs and the first order Mach hold autopilot and the second order Altitude hold model developed by Buzogany. These three autopilots constitute the complete flight control system used for both the Lead and Wing aircraft. In his thesis [3], Dargan developed a FFC using mixed feedback compensation. The controller was a three channel controller for controlling the horizontal x and y separation distances and the vertical z separation distance in the formation. The formation controller contained a proportional plus integral (PI) compensator on each channel with a linear mixer for the inputs to the PI compensators. The flight control system developed by Rohs and Buzogany and the formation flight controller developed by Dargan are modified and used as the foundations for this research.

The research analysis begins with the development of a simulation using the first order flight control system developed by Rohs and the formation flight controller developed by Dargan. An initial simulation model is developed in Simulink [17]. This model is used to verify the results achieved by Dargan. This ensures the flight control system model and the formation flight controller are accurately modeled. Once confidence is gained in the complete simulation model, the FCS models are adjusted to represent an F-16 class aircraft. The derivation for the effects of the horseshoe vortex are developed for a close formation. These effects are then integrated into the simulation as disturbances to the wing and the FFC is assessed. The FFC is adjusted to obtain the best performance.

Simulations are performed using Matlab version 4.21 Simulink package by The MathWorks [17]. Simulink allows use of simple blocks to form a frequency domain representation of a complex system. The non-linear differential equations are integrated using a fourth order Runge-Kutta technique and an Adams technique contained in Matlab Simulink. Both have an error limiting capability and step size control to ensure accurate results of integrations.

II. Model and Simulation Development

This chapter outlines the models, kinematic equations, and basic controller used in the nonlinear simulation. The majority of Section 2.1 has been taken from [12]. Models and figures have been changed to reflect the use of an F-16 class aircraft instead of a C-130 class aircraft. Sections 2.2, 2.3 and 2.4 have been taken directly from [12]; however, some figures have been modified slightly for the reasons stated above and a few paragraphs have been added to provide additional information. Section 2.5 contains a description of the controller developed by Dargan and walks through his controller design process. Sufficient information is provided to enable the reader to reproduce the results of this research.

2.1 Aircraft/Autopilot Models

The development of the aircraft/autopilot models was accomplished by Rohs [11] and Buzogany [1]. Since autopilot models were not explicitly available, models were obtained by designing a custom autopilot system around C-130H aircraft models provided by Lockheed. The autopilot system included Heading-hold, Mach-hold, and Altitude-hold autopilots. Due to the inherent properties of aircraft autopilots, the models exhibited overdamped, decoupled responses [11]. Using system identification techniques, first-order models were developed using rate limited, decoupled, first-order differential equations. The first-order aircraft/autopilot models are specified as:

$$\dot{V} = -\frac{1}{\tau_v}V + \frac{1}{\tau_v}V_c \tag{2.1}$$

$$\dot{\psi} = -\frac{1}{\tau_\psi}\psi + \frac{1}{\tau_\psi}\psi_c \tag{2.2}$$

$$\dot{h} = -\frac{1}{\tau_h}h + \frac{1}{\tau_h}h_c \tag{2.3}$$

where,

τ_ψ = heading time constant

τ_v = velocity time constant

τ_h = altitude time constant

The first-order aircraft/autopilot models are illustrated in Figure 2.1.

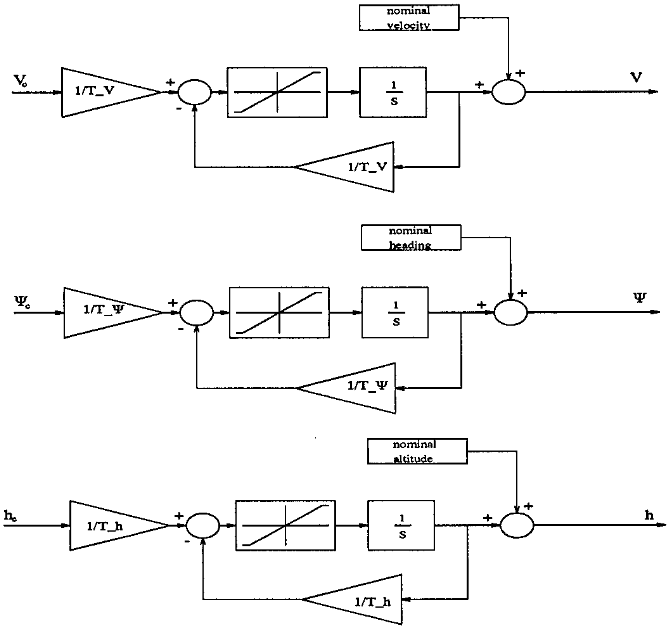

Figure 2.1 First-Order Aircraft Models

Second-order aircraft/autopilot models were developed by Buzogany [1] in order to more accurately represent the "true" aircraft/autopilot system. The most disturbing problem with first-order models is the presence of instantaneous heading rate and vertical velocity changes. Figure 2.2 compares an overdamped second-order response with a first-order response. While heading and altitude response was significantly improved using second-order models, it was found that velocity response was modeled more precisely using a first-order model with a larger time constant. Thus, the "second-order" models and time constants are specified as:

$$\dot{V} = -\frac{1}{\tau_v}V + \frac{1}{\tau_v}V_c \tag{2.4}$$

$$\ddot{\psi} = -\left(\frac{1}{\tau_{\psi_a}} + \frac{1}{\tau_{\psi_b}}\right)\dot{\psi} - \frac{1}{\tau_{\psi_a}\tau_{\psi_b}}\psi + \frac{1}{\tau_{\psi_a}\tau_{\psi_b}}\psi_c \tag{2.5}$$

$$\ddot{h} = -\left(\frac{1}{\tau_{h_a}} + \frac{1}{\tau_{h_b}}\right)\dot{h} - \frac{1}{\tau_{h_a}\tau_{h_b}}h + \frac{1}{\tau_{h_a}\tau_{h_b}}h_c \tag{2.6}$$

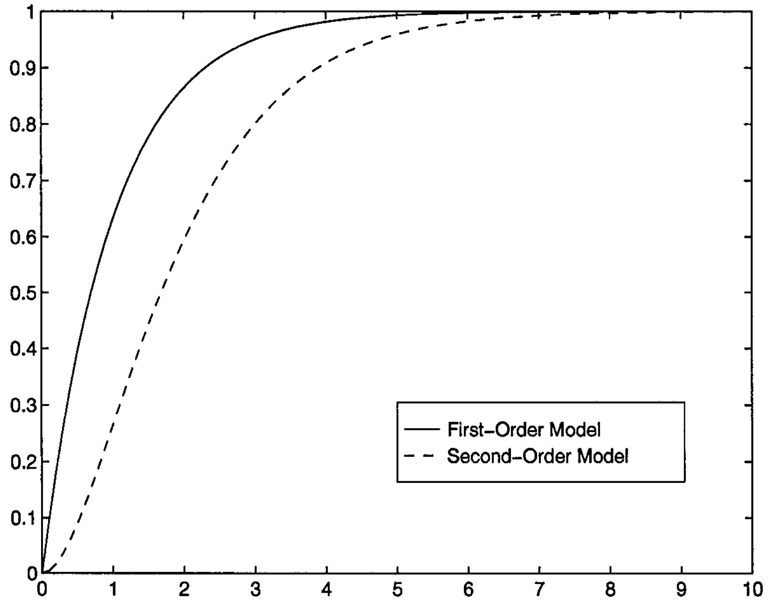

Figure 2.2 Comparison of First and Second-Order Responses

There are multiple ways to model a second order system containing nonlinear saturations caused by actuators. The models illustrated in Figure 2.3 were found to be the best representation of a true aircraft response. Comparison of these models with models not including saturations are almost identical for the envelope of maneuvers analyzed in this research.

The complete flight control system is composed of Rohs' first order Heading hold autopilot model and Buzogany's first order Mach-hold and second order Altitude-hold autopilot models.

$$\dot{V} = -\frac{1}{\tau_v}V + \frac{1}{\tau_v}V_c \tag{2.7}$$

$$\dot{\psi} = -\frac{1}{\tau_\psi}\psi + \frac{1}{\tau_\psi}\psi_c \tag{2.8}$$

$$\ddot{h} = -\left(\frac{1}{\tau_{h_a}} + \frac{1}{\tau_{h_b}}\right)\dot{h} - \frac{1}{\tau_{h_a}\tau_{h_b}}h + \frac{1}{\tau_{h_a}\tau_{h_b}}h_c \tag{2.9}$$

These models represented a C-130 class aircraft. The C-130 aircraft is a transport and responds slowly in comparison to an F-16 class aircraft. Since Rohs' and Buzogany's models are used in this research, the time constants and saturation values need to reflect the

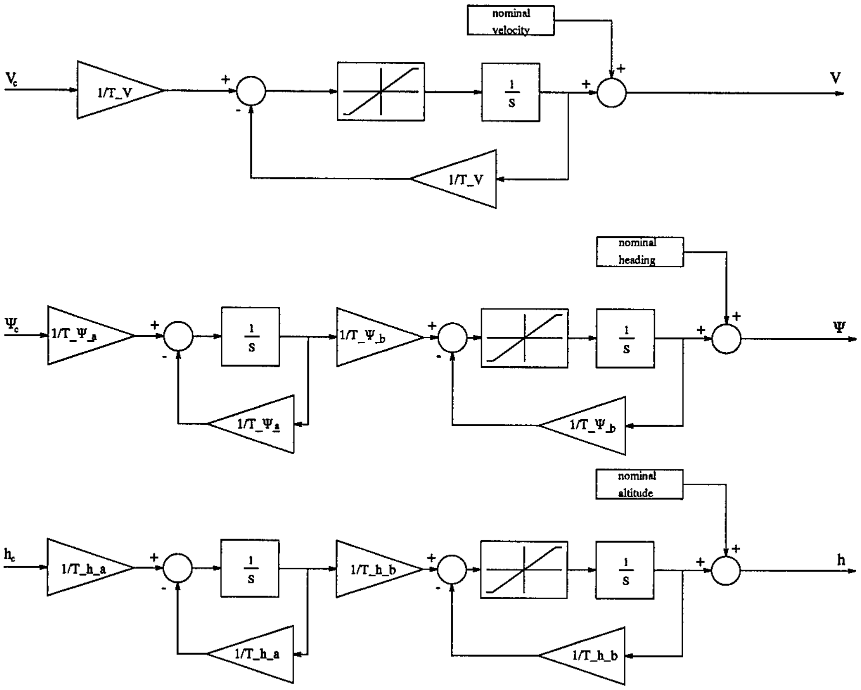

Figure 2.3 Second-Order Aircraft/Autopilot Models

Table 2.1 F-16 Class Composite Aircraft/Autopilot Parameters

Parameter	Value
τ_{ψ}	0.33 sec
τ_{v}	5 sec
τ_{h_a}	0.307 sec
τ_{h_b}	3.843 sec

performance characteristics for an F-16 class aircraft versus a C-130. First, this consisted of simply halving the time constants of the C-130 models to speed up the system response. This should be reasonable since an F-16 class aircraft responds much faster than C-130 aircraft. Secondly, the saturations were changed to match the maneuvering capability of an F-16 class aircraft. In general the saturations are about two to three times greater than those of a C-130 class aircraft. These new saturation values should also be reasonable since the maneuvering envelope of an F-16 is much greater than that of a C-130. Tables 2.1 and 2.2 show the F-16 class aircraft time constants and saturation values used in this research respectively. Figure 2.4 shows the complete F-16 class aircraft flight control system model used in this research.

Table 2.2 F-16 Class Composite Aircraft/Autopilot Saturation Values

Parameter	Lower Limit	Upper Limit
Acceleration	$-10\frac{ft}{sec^2}$	$5\frac{ft}{sec^2}$
Turn Rate	-6 $\frac{deg}{sec}$	$6\frac{deg}{sec}$
Vertical Velocity	$-126\frac{ft}{sec}$	$100\frac{ft}{sec}$

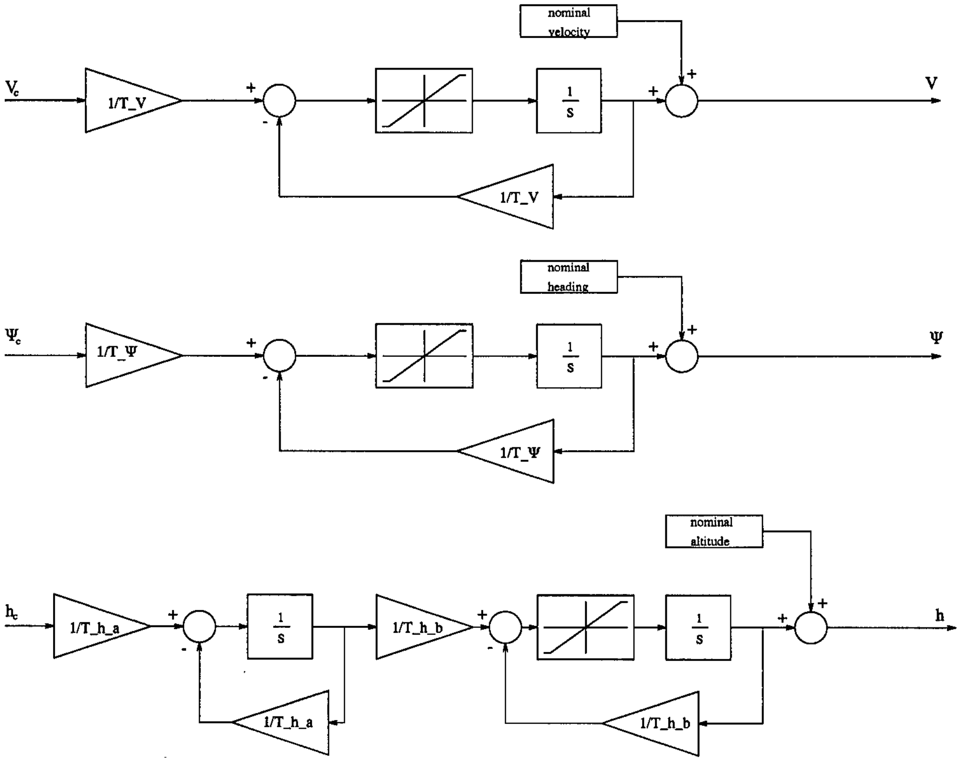

Figure 2.4 F-16 Class Composite Flight Control System Model

2.2 Equation of Coriolis

In order to express the formation flight control problem kinematics, reference frames must be established in the inertial and wing aircraft frames. Figure 2.5 shows the inertial and wing aircraft frames and the angular rotation vector. The subsequent rotations caused by maneuvering aircraft within the formation require a mathematical function relating vectors in different, rotating frames. The Equation of Coriolis performs this function.

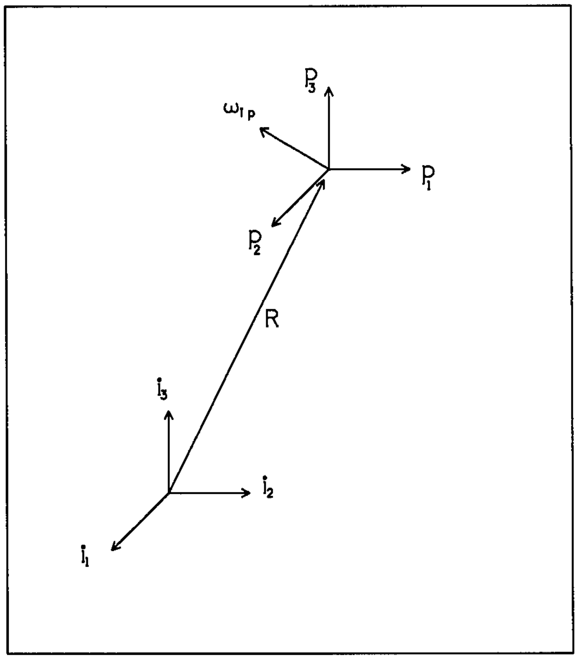

Figure 2.5 Inertial and Rotating Frames of Reference [3:Figure 1.7]

According to Blakelock [15], "The motion of an object as viewed from a reference frame is equal to the motion as seen from the moving frame, plus the motion resulting from the relative angular velocity of the moving frame with respect to the reference frame" [15]. This equation provides the basis for converting individual aircraft heading and velocity into separation distances. This is an essential part of the design process. The Equation of Coriolis is:

$$\dot{R}_i = \dot{R}_p + \omega_{ip} \times R_p \tag{2.10}$$

where

- $\dot{R}_i$ = the vector velocity of the point in the i reference frame
- $\dot{R}_p$ = the vector position of the point in question as seen from the p reference frame
- ω_{ip} = the vector angular velocity of the p reference frame with respect to the i reference frame
- R_p = the vector position of a point in the p frame

2.3 Formation Coordinate System

The coordinate system used in this thesis is identical to that of Dargan [3], Buzogany [1], and Reyna [9]. The analysis of the system kinematics uses two coordinate frames:

- Inertial base frame
- Rotating reference frame centered on wing aircraft

The base frame is an inertial North-East-Down system. For the purposes of this research, the earth is considered to be flat and inertially fixed. The inertial reference frame and separation distances are shown in Figure 2.6.

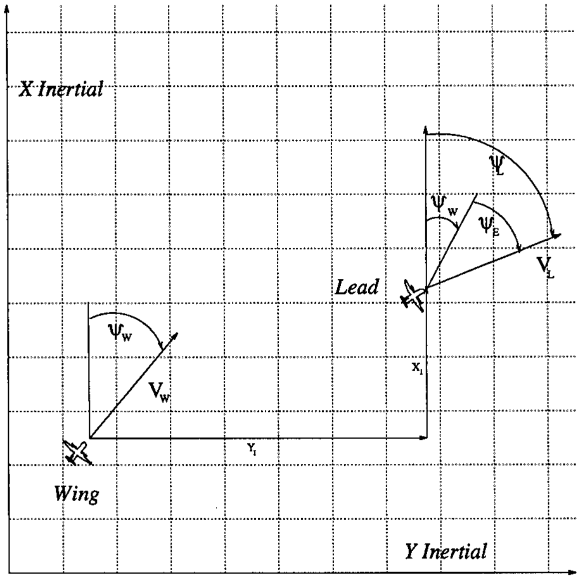

Figure 2.6 Inertial Reference Frame and Separation Distances

The wing aircraft frame is centered on the wing aircraft. The x axis is in the flight direction (i.e., aligned with the velocity vector), the y axis points out the starboard wing, and the z axis points toward the earth. The x and y separation distances are measured in the wing frame Figure 2.7.

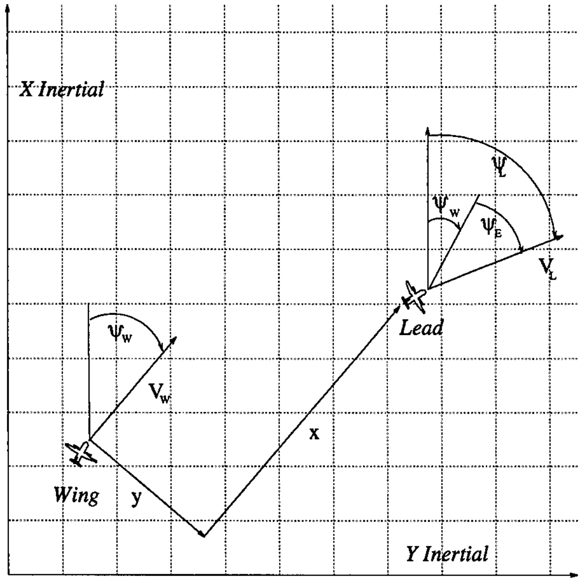

Figure 2.7 Wing's Rotating Reference Frame and Separation Distances

2.4 Kinematic Equations

In order to simulate the kinematics associated with the formation flight control model, kinematic equations must be derived. This has already been done by Dargan [3], Buzogany [1], and Reyna [9]. Reyna's derivation is repeated here to ensure clarity (from [9], pages 3:6-10).

Using the Equation of Coriolis (Chapter II), the velocity of the lead with respect to the wing has been found by Dargan as

$$V_{WL}^{W} = V_{L}^{W} - \omega_{W}^{W} \times R_{WL}^{W} - V_{W}^{W} + \omega_{W}^{W} \times R_{W}^{W} \tag{2.11}$$

where the following convention is followed:

- The superscript indicates the reference frame.
- The subscript indicates the parameter described by the vector or a relation between two parameters.

For example,

- V_{WL}^{W} = velocity of the lead aircraft with respect to the Wing, in the Wing's reference frame
- ω_{W}^{W} = angular velocity of the wing aircraft in the wing's reference frame
- R_{WL}^{W} = position of the Lead aircraft with respect to the Wing in the Wing's reference frame
- V_{W}^{W} = inertial velocity of the Wing aircraft in its own reference frame
- V_{L}^{W} = inertial velocity of the Lead aircraft in the Wing's reference frame

The development of the kinematic equations is based on the geometry defined in Figure 2.8.

The following relationships are defined:

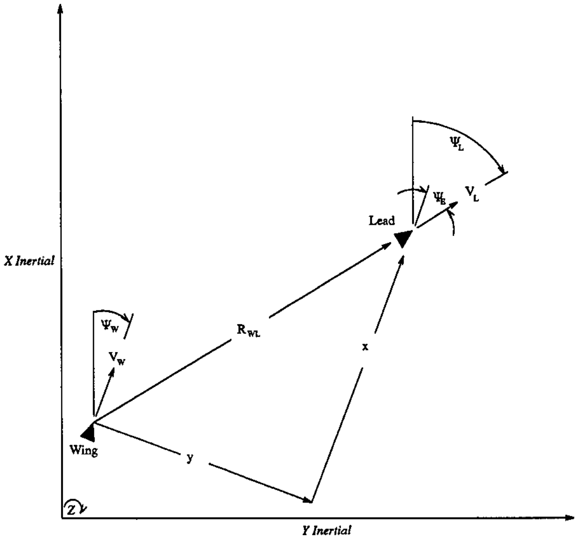

Figure 2.8 Relative Motion Diagram

$$\psi_E = \psi_L - \psi_W \tag{2.12}$$

$$\omega_W^W = \begin{bmatrix} 0 \\ 0 \\ \dot{\psi}_W \end{bmatrix} \tag{2.13}$$

$$R_{WL}^W = \begin{bmatrix} x^W \\ y^W \\ z^W \end{bmatrix} \tag{2.14}$$

$$V_W^W = \begin{bmatrix} V_W \\ 0 \\ 0 \end{bmatrix} \tag{2.15}$$

$$V_L^L = \begin{bmatrix} V_L \\ 0 \\ 0 \end{bmatrix} \tag{2.16}$$

$$R_W^W = \begin{bmatrix} 0 \\ 0 \\ 0 \end{bmatrix} \tag{2.17}$$

where,

ψ_E = heading error

V_L^L = velocity of the lead aircraft in its own reference frame

In order to solve Equation (2.11), V_L^L must be transformed into the wing reference frame. A Direction Cosine Matrix (DCM), developed by Dargan [3], is used to perform the rotation. Dargan found the DCM to be

$$C_L^W = \begin{bmatrix} cos\psi_E & -sin\psi_E & 0 \\ sin\psi_E & cos\psi_E & 0 \\ 0 & 0 & 1 \end{bmatrix} \tag{2.18}$$

V_L^W is found using by substituting (2.16) and (2.18) into the following equation

$$V_L^W = C_L^W V_L^L = \begin{bmatrix} V_L cos\psi_E \\ V_L sin\psi_E \\ 0 \end{bmatrix} \tag{2.19}$$

Substituting (2.13)-(2.15), (2.17), and (2.19) into equation (2.11) yields

$$V_{WL}^W = \begin{bmatrix} V_L cos\psi_E \\ V_L sin\psi_E \\ 0 \end{bmatrix} - \begin{bmatrix} 0 \\ 0 \\ \dot{\psi}_W \end{bmatrix} \times \begin{bmatrix} x^W \\ y^W \\ z^W \end{bmatrix} - \begin{bmatrix} V_W \\ 0 \\ 0 \end{bmatrix} + \begin{bmatrix} 0 \\ 0 \\ \dot{\psi}_W \end{bmatrix} \times \begin{bmatrix} 0 \\ 0 \\ 0 \end{bmatrix} \tag{2.20}$$

$$V_{WL}^W = \begin{bmatrix} V_L cos\psi_E \\ V_L sin\psi_E \\ 0 \end{bmatrix} - \begin{bmatrix} -\dot{\psi}_W y^W \\ \dot{\psi}_W x^W \\ 0 \end{bmatrix} - \begin{bmatrix} V_W \\ 0 \\ 0 \end{bmatrix} \tag{2.21}$$

Separating (2.21) into scalar components yields

$$\dot{x}^W = V_L cos\psi_E + \dot{\psi}_W y^W - V_W \tag{2.22}$$

$$\dot{y}^W = V_L sin\psi_E - \dot{\psi}_W x^W \quad (2.23)$$

$$\dot{z}^W = 0 \quad (2.24)$$

Equations (2.22) - (2.24) describe the kinematics of the formation (x and y separations) in terms of the individual aircraft's heading and velocity. The altitude (z) separations are non-dynamic and are simply the difference between the aircraft altitudes.

2.5 Formation Flight Controller

Each aircraft is controlled through the inputs to the flight control system. These inputs are the settings normally supplied by the pilot. The control strategy implemented by Dargan was a two tiered structure as shown in Figure 2.9. The upper tier is for control of the formation as a whole, and the lower tier is for control of the individual aircraft within the formation [3]. The upper tier is used to control the guidance of the formation. This consists of the velocity, heading, and altitude for the formation. The lower tier is used to control the actual formation geometry. This consists of the x, y and, z separation distances between the Lead and Wing aircraft in the formation.

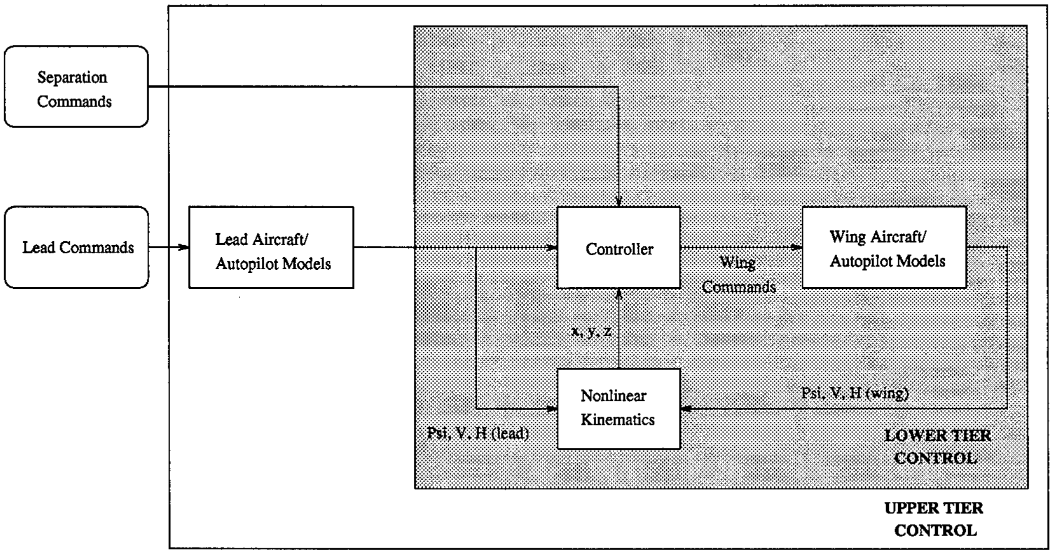

Figure 2.9 FFC Structure

Dargan [3] separated the controller into three control channels: longitudinal, lateral and vertical. The longitudinal or x-channel was composed of the longitudinal x separation distance and the relative velocity between the lead and wing aircraft. The lateral or y-channel was composed of the lateral y separation distance and the relative heading angle between the lead and wing aircraft. The vertical or z-channel was simply the separation distance between the lead and wing aircraft. In all channels the lead responds to the formation level commands while the wing responds to the separation commands.

Dargan iteratively improved the controller design in stages. First, he choose a series of test cases to use for measuring performance between each design. This consisted of cases for changes in the x, y, and z separation distances and cases for changes in the velocity, heading, and altitude of the formation. Then, he analyzed the open loop response and used this as the baseline for all subsequent designs. The open loop control response verified that the system required some form of feedback. The formation maneuver commands could be followed with zero steady-state errors, but the formation separation distances could not be maintained.

Dargan then implemented state feedback for the formation commands of velocity, heading, and altitude. A cascade compensator was not included in the feedback loop. The longitudinal channel response for a change in the separation distance resulted in no steady-state error. The response for a change in velocity resulted in a steady-state error in the x separation distance. Therefore, the longitudinal channel required some compensation due to the steady state error from a change in velocity. The lateral channel response was similar to the response of the longitudinal channel. A change in y separation resulted in no error. Heading change caused a steady-state tracking error in the y separation distance. Again, some form of compensation was needed for the lateral channel as well. The vertical channel had a steady-state error for both a change in vertical separation distance as well as a change in altitude. Compensation was also required for this channel. Overall, state feedback was not enough and some form of compensation was required for each channel.

Dargan next added a Proportional plus Integral (PI) compensator for control of separation errors. This was composed of three independent PI controllers; one for each channel. This controller resulted in a zero steady-state separation error for a change in the separation distance and a change in formation maneuver for each channel. However, the responses for the longitudinal and lateral channels had undesirable overshoots. Dargan labeled this controller as the *unmixed* controller. The unmixed controller equations are

$$V_{WC}(t) = (K_{X_p})\Delta x_E + (K_{X_I}) \int_0^t \Delta x_E dt \tag{2.25}$$

$$\psi_{WC}(t) = (K_{Y_p})\Delta y_E + (K_{Y_I}) \int_0^t \Delta y_E dt \tag{2.26}$$

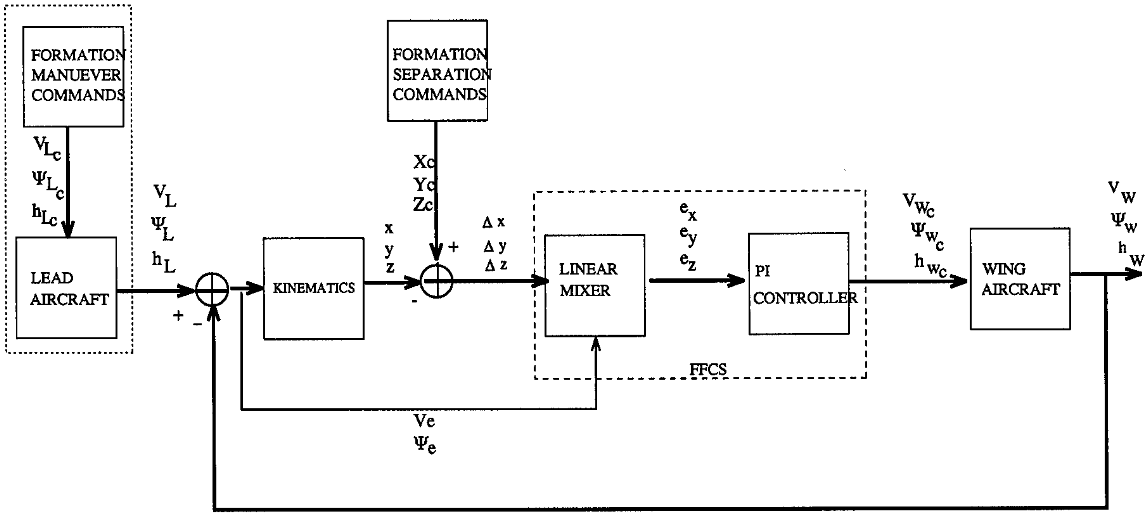

Figure 2.10 Dargan FFCS Block Diagram

$$h_{WC}(t) = (K_{Z_p})\Delta z_E + (K_{Z_I}) \int_0^t \Delta z_E dt \tag{2.27}$$

where,

- V_{WC} is the wing aircraft velocity command from the PI controller
- ψ_{WC} is the wing aircraft heading command from the PI controller
- h_{WC} is the wing aircraft altitude command from the PI controller
- Δx_E, Δy_E and Δz_E are the respective x, y, and z separation errors.
- K_{X_p} and K_{X_I} are the x channel proportional and integral gains
- K_{Y_p} and K_{Y_I} are the y channel proportional and integral gains
- K_{Z_p} and K_{Z_I} are the wing aircraft z channel proportional and integral gains.

Lastly, Dargan developed a controller that used a mixture of separation errors and formation errors. This was a *mixed* controller as opposed to the previous unmixed controller. The mixed controller included a linear mixer cascaded with the PI controller as seen in Figure 2.10. This controller worked the same way as any other PI controller. It attempts to null out an error between the commanded input and the system response. The unmixed controller attempted to null out the error between the commanded separation distances and the actual separation distance. The linear mixer combines the separation distance errors and the maneuver errors for each channel and feeds this mixed error signal to the PI controller to be nulled out. The separation errors for the longitudinal and lateral channels are replaced with the mixed error signals below

$$e_X = k_V V_E + k_x \Delta x_E \tag{2.28}$$

$$e_Y = k_\psi \psi_E + k_y \Delta y_E \tag{2.29}$$

$$e_Z = k_z \Delta z_E \tag{2.30}$$

where:

- e_X is the longitudinal channel input to the PI controller
- k_V is the gain on the velocity error signal, V_E
- k_x is the gain on the x separation error signal, Δx_E
- e_Y is the lateral channel input to the PI controller
- k_ψ is the gain on the heading error signal, ψ_E
- k_y is the gain on the y separation error signal, Δy_E
- e_Z is the vertical channel input to the PI controller
- k_z is the gain on the z separation error signal, Δz_E

The mixed control laws are

$$V_{WC}(t) = K_{X_p} e_X + K_{X_I} \int_0^t e_X dt \tag{2.31}$$

$$\psi_{WC}(t) = K_{Y_p} e_Y + K_{Y_I} \int_0^t e_Y dt \tag{2.32}$$

$$h_{WC}(t) = K_{Z_p} e_Z + K_{Z_I} \int_0^t e_Z dt \tag{2.33}$$

The linear mixer and PI controller are shown in Figure 2.11. The x- and y-channels are identical except the V_E term is replaced with the ψ_e term and Δy_e replaces Δx_e. The only difference between the z-channel and the x and y-channels is the z-channel does not have an altitude error term since the z separation and the altitude difference are synonymous.

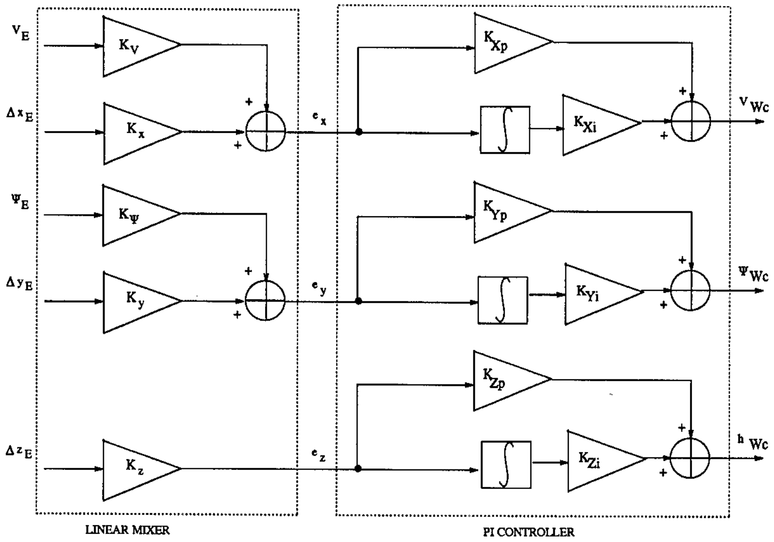

Figure 2.11 Dargan FFCS Lateral channel

Through iteration, Dargan determined the gains to achieve the best performance [3]. The longitudinal channel still had an overshoot/undershoot, but the magnitude of the overshoot/undershoot was reduced and the response was faster. The lateral channel resulted in similar improvements. The magnitude of the undershoot/overshoot was reduced and a faster time response was achieved. The mixed controller achieved the desired response and concludes the controller designs developed by Dargan[1].

2.6 Summary

In this chapter, the composite F-16 class flight control system for the Lead and the Wing aircraft was developed. The large formation flight controller design process was discussed. Finally, the mixed formation flight controller to be applied to this research was developed.

---

[1] Please note Dargan's k_x and k_y gains are negative for a negative feedback system model.

III. Upwash and Sidewash Effects on Formation

This chapter outlines the method used to determine the upwash and sidewash created by the Lead's vortex on the Wing aircraft. The upwash and sidewash are then used to determine the new close formation stability derivatives. The new close formation stability derivatives are then applied to the Wing FCS.

3.1 Upwash and Sidewash Derivations

An aircraft moving through the air creates vortices behind the wing. These vortices can be seen in Figure 1.1 and are repeated here in Figure 3.1. These vortices exert aerodynamic forces on the Wing aircraft in the formation. The formation geometry is determined by the Lead's $\bar{x}$, $\bar{y}$, and $\bar{z}$ position relative to the Wing aircraft, in a rotating frame of reference attached to the Wing as shown in Figure 1.2.

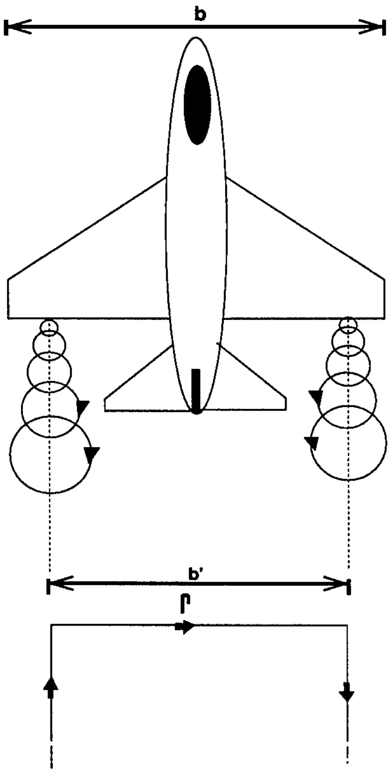

Figure 3.1 Horse Shoe Vortex

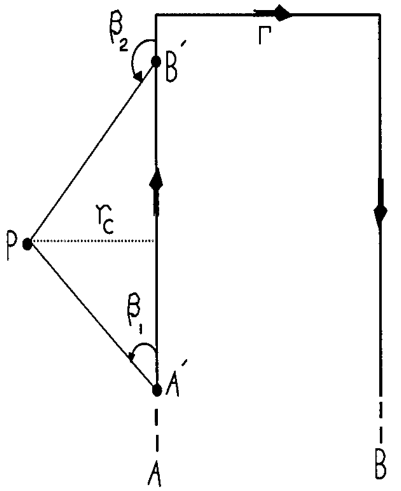

Figure 3.2 Field Strength at Point P due to Filament A

3.1.1 Biot-Savart. This section outlines the method used to calculate the upwash and sidewash created by the Lead aircraft on the Wing aircraft. The derivation of the effect of the Lead aircraft's wing vortex on the wingman's wing is determined by using an analogy with electric field strength produced by an electric current in electromagnetics. A vortex filament from Fig. 3.1 is redrawn in Fig. 3.2. The angles β_1 and β_2 determined by the vortex filament segment [A' B'] and the point P are shown in Fig. 3.2. The fluid dynamics analogue of the **Biot-Savart** law from electromagnetics states that the induced velocity $\vec{W}$ from vortex filament A is given by

$$\vec{W} = \frac{\hat{\Phi}\Gamma}{4\pi r_c}(\cos\beta_1 - \cos\beta_2) \tag{3.1}$$

where the vortex strength per unit length is Γ, r_c is the distance from the vortex filament to the point P, and the velocity of the air wash caused by the vortex filament at point P and out of the page is $\vec{W}$. The unit vector $\hat{\Phi}$ is orthogonal to the radius vector r_c. When point A' is at $-\infty$, the angle $\beta_1 = 0$, and when point B' is at $+\infty$, the angle $\beta_2 = \pi$. Asssuming that the longitudinal separation in the formation is large, i.e., greater than two wingspans, is tantamount to saying that point B' is effectively at $+\infty$. When the actual distance between the tail of the Leader and the nose of the Wing is greater than 2b, where b is the wingspan, this effectively places point B' at $+\infty$. Then the Lead aircraft's spanwise contribution to the flow field near the Wing aircraft can be neglected. Similarly, the Wing

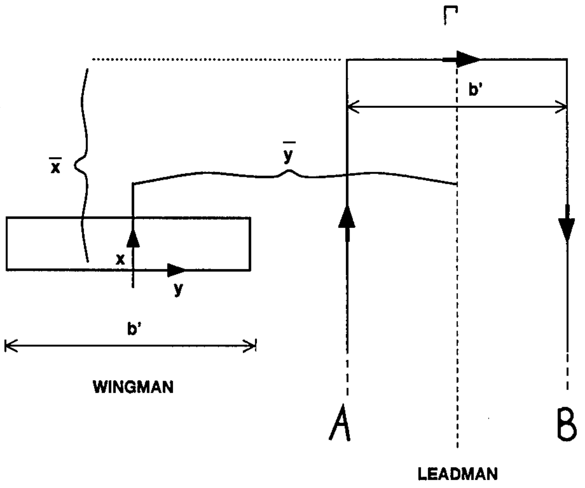

Figure 3.3 View from above the two aircraft

aircraft's influence on the flow field near the Lead aircraft's wing can be neglected. These are the main assumptions used in this research for the location of the Wing aircraft's wing with respect to the vortices caused by the Lead aircraft's wing. The vortex goes back a great distance before it is diffused, validating the assumption that point A' is essentially at $-\infty$. This reduces Eq. 3.1 to the simplified form of the Biot-Savart law,

$$\vec{W} = \frac{\hat{\Phi}\Gamma}{2\pi r_c} \tag{3.2}$$

The wash vector, $\vec{W}$, at the point P for the geometry of Fig. 3.2, is out of the page. This would be the special case of no sidewash and all upwash at point P on the page.

Fig. 3.3 is a view from above the two aircraft which contains both the Lead aircraft replaced by its horse shoe vortex approximation, with the sides of the horse shoe represented by the A and B filaments. The Wing aircraft is represented by its elliptical wing approximation. The reduced wingspan of the Wing aircraft is represented by b'. This is the corrected value for an elliptical lift distribution on a wing and is

$$b' = \frac{\pi}{4} b \tag{3.3}$$

Fig. 3.4 shows the view from behind the two aircraft. The radius vectors, $\vec{r_c}$, from each vortex filament to the wing, disregarding the $\hat{x}$ component due to the infinite length of the

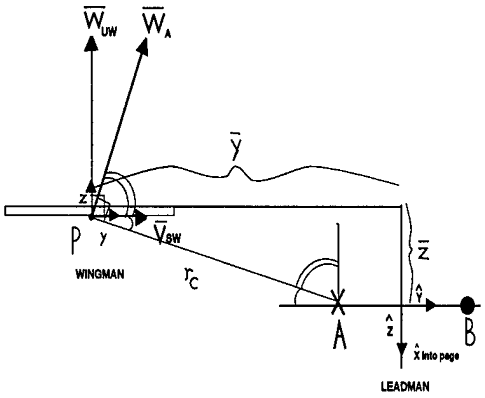

Figure 3.4 Behind view showing $\vec{W}_A$ field

filaments, are for filaments A and B

$$\vec{r}_A = (\bar{y} - \frac{b'}{2} - y)\hat{y} + (\bar{z} - z)\hat{z} \tag{3.4}$$

$$\vec{r}_B = (\bar{y} + \frac{b'}{2} - y)\hat{y} + (\bar{z} - z)\hat{z} \tag{3.5}$$

where, $\hat{y}$ and $\hat{z}$ are the unit directional vectors. Based on Figures 3.4 and 3.5 and with a bit of geometrical insight, it can be shown that the total induced upwash $\bar{W}_{UW}$ at station (y,0) from both filaments emanating from the Lead's wing is

$$\vec{W}_{UW} = \frac{\Gamma_L}{2\pi}\left[\frac{\left[(\bar{y} - \frac{b'}{2} - y)\right]}{\left[\sqrt{(\bar{y} - \frac{b'}{2} - y)^2 + \bar{z}^2}\right]} - \frac{\left[(\bar{y} + \frac{b'}{2} - y)\right]}{\left[\sqrt{(\bar{y} + \frac{b'}{2} - y)^2 + \bar{z}^2}\right]}\right](-\hat{z}); -\frac{1}{2}b' \leq y \leq \frac{1}{2}b' \tag{3.6}$$

where $\bar{x}$ is the separation distance in the $\hat{x}$ direction, $\bar{y}$ is the separation distance in the $\hat{y}$ direction, and $\bar{z}$ is the separation distance in the $\hat{z}$ direction. The total induced sidewash $\bar{V}_{SW}$ at station (0,z) from both filaments is

$$\vec{V}_{SW} = \frac{\Gamma_L}{2\pi}\left[\frac{[(\bar{z} - z)^2]}{\left[\sqrt{(\bar{y} - \frac{b'}{2})^2 + (\bar{z} - z)^2}\right]} - \frac{[(\bar{z} - z)^2]}{\left[\sqrt{(\bar{y} + \frac{b'}{2})^2 + (\bar{z} - z)^2}\right]}\right]\hat{y}; 0 \geq z \geq -h_z \tag{3.7}$$

3.1.2 Average Upwash and Sidewash. The average induced upwash on the Wing aircraft's wing is thus calculated by integrating Eq. (3.6):

$$\vec{W}_{UW_{avg}} = \frac{\Gamma_L}{2\pi b}\int_{-\frac{b'}{2}}^{\frac{b'}{2}} \left[\frac{\left[(\bar{y} - \frac{b'}{2} - y)\right]}{\left[\sqrt{(\bar{y} - \frac{b'}{2} - y)^2 + \bar{z}^2}\right]} - \frac{\left[(\bar{y} + \frac{b'}{2} - y)\right]}{\left[\sqrt{(\bar{y} + \frac{b'}{2} - y)^2 + \bar{z}^2}\right]} \right] dy(-\hat{z}) \qquad (3.8)$$

After changing the variables to $u = ((\bar{y} - \frac{b'}{2} - y)^2 + \bar{z}^2)$ for the first term and similarly $u' = ((\bar{y} + \frac{b'}{2} - y)^2 + \bar{z}^2)$ for the second term, and changing the limits to match with the new variables u and u', the integral in Eq. (3.8) is evaluated as

$$\vec{W}_{UW_{avg}} = \frac{\Gamma_L}{4\pi b'}\left[\ln\frac{\bar{y}^2 + \bar{z}^2}{(\bar{y} - b')^2 + \bar{z}^2} - \ln\frac{(\bar{y} + b')^2 + \bar{z}^2}{\bar{y}^2 + \bar{z}^2}\right](-\hat{z}) \qquad (3.9)$$

Similarly, averaging by integrating from the bottom of the tail at 0 to the top of the tail at $-h_z$ yields the average sidewash, $\bar{V}_{SW_{avg}}$, at the vertical tail

$$\vec{V}_{SW_{avg}} = \frac{\Gamma_L}{4\pi h_z}\left[\ln\frac{(\bar{y} - \frac{b'}{2})^2 + \bar{z}^2}{(\bar{y} - \frac{b'}{2})^2 + (\bar{z} + h_z)^2} - \ln\frac{(\bar{y} + \frac{b'}{2})^2 + \bar{z}^2}{(\bar{y}^2 + \frac{b'}{2}) + (\bar{z} + h_z)^2}\right]\hat{y} \qquad (3.10)$$

3.1.3 Corrected Average Upwash and Sidewash. A correction term, μ^2, needs to be included in both the numerator and denominator of each term contained in the natural logarithms in Eqs. (3.9) and (3.10) in order to take into account physical viscosity effects and to make the mathematical derivation more accurately follow the experimental data [13],[14]. This is a dimensionless number and requires both the numerator and denominator terms inside the logarithm to be non-dimensionalized. To make the terms non-dimensional, both the numerators and denominators are divided by b^2. The correction term, μ^2, is then added to both numerators and denominators. The resulting equations are

$$\vec{W}_{UW_{avg}} = \frac{\Gamma_L}{4\pi b}\left[\ln\frac{y'^2 + z'^2 + \mu^2}{(y' - \frac{\pi}{4})^2 + z'^2 + \mu^2} - \ln\frac{(y' + \frac{\pi}{4})^2 + z'^2 + \mu^2}{y'^2 + z'^2 + \mu^2}\right](-\hat{z}) \qquad (3.11)$$

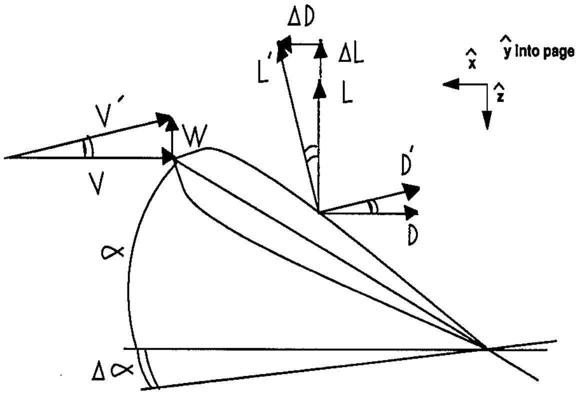

Figure 3.5 Sideview of Wingman's wing lift rotation

and

$$\vec{V}_{SW_{avg}} = \frac{\Gamma_L}{4\pi h_z}\left[\ln\frac{(y'-\frac{\pi}{8})^2+z'^2+\mu^2}{(y'-\frac{\pi}{8})^2+(z'+\frac{h_z}{b})^2+\mu^2} - \ln\frac{(y'+\frac{\pi}{8})^2+z'^2+\mu^2}{(y'+\frac{\pi}{8})^2+(z'+\frac{h_z}{b})^2+\mu^2}\right]\hat{y} \quad (3.12)$$

where now the nondimensional formation geometry parameters are $y' \equiv \frac{\bar{y}}{b}$ and $z' \equiv \frac{\bar{z}}{b}$.

3.2 Calculation of Change in Lift and Drag

The upwash on the wing causes a change in the angle of attack of the wing. This causes a rotation in the lift and drag vectors.

3.2.1 Change in Drag. In Fig. 3.5, V is the velocity of the aircraft, W is the upwash, and V' is the composite velocity of the air at the surface of the wing. The original lift and drag vectors are represented by L and D and the rotated lift and drag are represented by L' and D', respectively. It can be seen from Fig. 3.5 that the change in angle of attack is

$$\Delta\alpha = \arctan\left(\frac{|\vec{W}_{UW}|}{V}\right) \approx \frac{|\vec{W}_{UW}|}{V} \quad (3.13)$$

where the approximation for small angles has been applied. It can also be seen from Fig. 3.5 that consequently the change in drag, ΔD_W,due to the rotation of the lift vector is

$$\Delta D_W = -L_W \tan\Delta\alpha \approx -L_W\left(\frac{|\vec{W}_{UW}|}{V}\right)\hat{x} \quad (3.14)$$

where again, the small angle approximation is used. Dividing both sides by the dynamic pressure $\bar{q}$ and the surface area S of the wing, the non-dimensional coefficient of drag increment ΔC_{D_W} is

$$\Delta C_{D_W} = \frac{\Delta D_W}{\bar{q}S} = -\frac{L_W}{\bar{q}S}\frac{|\vec{W}_W|}{V} = -C_{L_W}\frac{\vec{W}_W}{V} \tag{3.15}$$

Also, the vortex strength per unit length can be expressed as

$$\Gamma = \frac{L_L}{\rho V b'} = \frac{L_L}{\rho V \frac{\pi}{4} b} = \frac{\frac{1}{2}\rho V^2 S C_{L_L}}{\rho V \frac{\pi}{4} b} = \frac{2}{\pi}\frac{S}{b^2} C_{L_L} V b = \frac{2}{\pi A_R} C_{L_L} V b \tag{3.16}$$

where S = area of wing, b = wing span, V = airspeed of formation, A_R = aspect ratio of wing, and C_{L_L} = lift coefficient of the Lead aircraft. Substituting the above equation for vortex strength and also substituting the previously derived upwash expression into the change in drag equation, yields

$$\Delta C_{D_W} = \frac{1}{\pi A_R} C_{L_L} C_{L_W} \frac{2}{\pi^2}\left[\ln\frac{y'^2 + z'^2 + \mu^2}{(y' - \frac{\pi}{4})^2 + z'^2 + \mu^2} - \ln\frac{(y' + \frac{\pi}{4})^2 + z'^2 + \mu^2}{y'^2 + z'^2 + \mu^2}\right] \tag{3.17}$$

3.2.2 Change in Lift. The change in lift, ΔC_{L_W}, is given by

$$\Delta C_{L_W} = \Delta\alpha a_W = \frac{|\vec{W}_{UW}|}{V} a_W \tag{3.18}$$

where a_W is the lift curve slope of the wing. Substitution of the upwash and vortex strength values as before, results in

$$\Delta C_{L_W} = \frac{a_W}{\pi A_R} C_{L_L} \frac{2}{\pi^2}\left[\ln\frac{y'^2 + z'^2 + \mu^2}{(y' - \frac{\pi}{4})^2 + z'^2 + \mu^2} - \ln\frac{(y' + \frac{\pi}{4})^2 + z'^2 + \mu^2}{y'^2 + z'^2 + \mu^2}\right] \tag{3.19}$$

This is the change in lift coefficient of the Wing from the upwash created by the Lead aircraft.

3.2.3 Change in Side Force.

The sidewash created by the Lead also causes a change in the force on the vertical tail. This change in side force, ΔF_Y, is

$$\Delta \vec{F}_Y = \eta \bar{q} S_{vt} a_{vt} \frac{|\vec{V}_{SW}|}{V} \hat{y} \tag{3.20}$$

where η is the aerodynamic efficiency factor at the tail, S_{vt} is the vertical tail area, and a_{vt} is the lift curve slope of the vertical tail. The non-dimensional change in side force coefficient, is

$$\Delta C_Y = \eta \frac{S_{vt}}{S} a_{vt} \frac{|\vec{V}_{SW}|}{V} \tag{3.21}$$

Inserting the sidewash expression of Eq. (3.12) back into the non-dimensional side force Eq. (3.21) gives the side force coefficient

$$\begin{aligned} \Delta C_Y \quad = \quad & \eta \frac{S_{vt}}{S} \frac{a_{vt}}{V} \frac{\Gamma_L}{4\pi h_z} \cdot \\ & \left[\ln \frac{(y' - \frac{\pi}{8})^2 + z'^2 + \mu^2}{(y' - \frac{\pi}{8})^2 + (z' + \frac{h_z}{b})^2 + \mu^2} - \ln \frac{(y' + \frac{\pi}{8})^2 + z'^2 + \mu^2}{(y' + \frac{\pi}{8})^2 + (z' + \frac{h_z}{b})^2 + \mu^2} \right] \end{aligned} \tag{3.22}$$

Finally, substituting back in for Γ by using Eq. (3.16), the change in side force coefficient becomes

$$\begin{aligned} \Delta C_Y \quad = \quad & \frac{1}{\pi A_R} \frac{\eta S_{vt} a_{vt} C_{L_L} b}{2 S h_z} \frac{2}{\pi} \cdot \\ & \left[\ln \frac{(y' - \frac{\pi}{8})^2 + z'^2 + \mu^2}{(y' - \frac{\pi}{8})^2 + (z' + \frac{h_z}{b})^2 + \mu^2} - \ln \frac{(y' + \frac{\pi}{8})^2 + z'^2 + \mu^2}{(y' + \frac{\pi}{8})^2 + (z' + \frac{h_z}{b})^2 + \mu^2} \right] \end{aligned} \tag{3.23}$$

3.3 Modified Wing Aircraft Control System

It is envisaged that each aircraft is equipped with a flight control system that includes three standard autopilots: Heading hold, Mach hold, and Altitude hold autopilots.The aircraft autopilots that makeup the FCS are developed in Chapter II. The formation flight control autopilot resides on the Wing aircraft. It is an outer-loop controller which receives measurements of the Lead aircraft's position relative to the Wing aircraft and it drives the reference signals of the Wing's three axes Mach hold, Heading hold, and Altitude hold autopilots.

The formation flight control autopilot resides on the Wing aircraft. It is an outer-loop controller which receives measurements of the Lead aircraft's position relative to the Wing aircraft and it drives the reference signals of the Wing's three axes, Mach hold, Heading hold, and Altitude hold autopilots.

For close formation flight, the Wing FCS needs to be modified to account for the additional aerodynamic interactions created by the upwash and sidewash from the Lead aircraft. The upwash causes an aerodynamic force in the $\hat{x}$ and $\hat{z}$ directions in the form of a change in drag and change in lift as derived above. Thus, the Wing aircraft needs to be retrimmed in pitch. The sidewash induces a force in the $\hat{y}$ direction caused by a change in lift on the vertical tail, which requires the Wing aircraft's lateral directional control channel to be retrimmed. This change in forces need to be trimmed out by the Wing's FCS. Above and beyond this retrimming action, it is important to include the dynamical change in forces caused by a perturbation Δx, Δy, and Δz in the Lead's position in the formation relative to the Wing.

The upwash and sidewash also cause changes in moments applied to the wing aircraft. However, moment effects are not explored in this paper because of the rather rudimentary modeling employed, where the Wing aircraft is considered a point mass.

Thus, new stability derivatives for change in Wing drag resulting from a change in $\bar{x}$, $\bar{y}$, and $\bar{z}$ positions in the formation need to be determined for the Mach hold channel. Similarly, the new stability derivatives for the change in lift due to a change in the $\bar{x}$, $\bar{y}$, and $\bar{z}$ positions need to be determined for the Altitude hold channel. Finally, new stability derivatives for the change in side force due to a change in $\bar{x}$, $\bar{y}$, and $\bar{z}$ positions in the formation need to be determined for use in the Heading hold channel. The resulting Wing FCS is

$$\begin{aligned}
\dot{V}_W &= -\frac{1}{\tau_V}V_W + \frac{1}{\tau_V}V_{W_c} + \\
&\quad \frac{\bar{q}S}{m}\left[\Delta C_{D_{W_x}}x + \Delta C_{D_{W_y}}y + \Delta C_{D_{W_z}}z\right] \\
\dot{\psi}_W &= -\frac{1}{\tau_\psi}\psi_W + \frac{1}{\tau_\psi}\psi_{W_c} + \\
&\quad \frac{\bar{q}S}{mV}\left[\Delta C_{Y_{W_x}}x + \Delta C_{Y_{W_y}}y + \Delta C_{Y_{W_z}}z\right] \\
\ddot{h}_W &= -\left(\frac{1}{\tau_{h_a}} + \frac{1}{\tau_{h_b}}\right)\dot{h}_W - \frac{1}{\tau_{h_a}\tau_{h_b}}h_W + \frac{1}{\tau_{h_a}}h_{W_c} + \\
&\quad \frac{\bar{q}S}{m}\left[\Delta C_{L_{W_x}}x + \Delta C_{L_{W_y}}y + \Delta C_{L_{W_z}}z\right]
\end{aligned}$$

where: V_{W_c} is the reference signal to the Wing Mach-hold autopilot, and similarly, h_{W_c} is the reference signal to the Altitude-hold autopilot and ψ_{W_c} is the reference signal to the Heading-hold autopilot. V_W is the Wing's velocity, ψ_W is the Wing's heading, h_W is the Wing's altitude, and x,y, and z are the perturbations in the Lead's position in the formation relative to the Wing from the nominal location $(\bar{x}, \bar{y}, \bar{z})$. In the $\dot{V}_W$ differential equation the new stability derivatives for the longitudinal and the vertical perturbations, $\Delta C_{D_{W_x}}$, $\Delta C_{D_{W_y}}$, and $\Delta C_{D_{W_z}}$, and $\Delta C_{L_{W_x}}$, $\Delta C_{L_{W_y}}$, and $\Delta C_{L_{W_z}}$ are multiplied by $\frac{\bar{q}S}{m}$. Multiplying them by $\bar{q}S$ converts them back to a force, and then dividing by the mass converts them to an acceleration, as required. The new stability derivatives for the heading differential equation are multiplied by $\frac{\bar{q}S}{mV}$. The additional division by the velocity is required because the heading rate is an angular velocity. Also, the centrifugal acceleration is $A = \omega \times V$ where V is the aircraft's velocity and ω is the angular velocity. Since all of these vectors are orthogonal to each other, $\omega = A/V$. Hence, the new stability derivatives in the heading equation, when multiplied by $\frac{\bar{q}S}{mV}$ are converted to an angular velocity, as required in the heading equation.

3.3.1 Calculation of the New Formation Stability Derivatives. The change in drag, lift, and side force on the Wing aircraft in a close formation have been previously calculated. To determine the change in these forces due to a change in the x, y, and z Lead's relative position in the formation, a linearization is performed about the nominal Lead position (which is measured with respect to the Wing's position) in the optimal close formation: The latter is $\bar{y} = \frac{\pi}{4}b$ and $\bar{z} = 0$. This requires derivatives of the change in drag, lift, and side force to be evaluated at these values for $\bar{y}$ and $\bar{z}$.

First, a dimensionless expression is introduced for the change in induced drag, $\sigma_{UW}(y', z')$:

$$\sigma_{UW}(y', z') = \frac{2}{\pi^2}\left[\ln\frac{y'^2 + z'^2 + \mu^2}{(y' - \frac{\pi}{4})^2 + z'^2 + \mu^2} - \ln\frac{(y' + \frac{\pi}{4})^2 + z'^2 + \mu^2}{y'^2 + z'^2 + \mu^2}\right] \tag{3.24}$$

A similar non-dimensional function is defined for the sidewash component, $\sigma_{SW}(y', z')$:

$$\sigma_{SW}(y', z') = \frac{2}{\pi}\left[\ln\frac{(y' - \frac{\pi}{8})^2 + z'^2 + \mu^2}{(y' - \frac{\pi}{8})^2 + (z' + \frac{h_z}{b})^2 + \mu^2} - \ln\frac{(y' + \frac{\pi}{8})^2 + z'^2 + \mu^2}{(y' + \frac{\pi}{8})^2 + (z' + \frac{h_z}{b})^2 + \mu^2}\right] \tag{3.25}$$

Based on these definitions, the change in lift, drag, and side force are expressed as

$$\begin{aligned}
\Delta C_{D_W} &= \frac{1}{\pi A_R} C_{L_L} C_{L_W} \sigma_{UW}(y', z') && (3.26)\\
\Delta C_{L_W} &= \frac{1}{\pi A_R} a C_{L_W} \sigma_{UW}(y', z') && (3.27)\\
\Delta C_{Y_W} &= \frac{1}{\pi A_R} \frac{\eta S_{vt} a_{vt} b}{2 S h_z} C_{L_L} \sigma_{SW}(y', z') && (3.28)
\end{aligned}$$

The only parts of the above equations that vary with a change in the x, y, and z position are the $\sigma_{UW}(y', z')$ function for the change in drag and lift, and the $\sigma_{SW}(y', z')$ function for the change in side force. The derivatives of $\sigma_{UW}(y', z')$ and $\sigma_{SW}(y', z')$ are analytically obtained as follows: The partial derivatives for $\sigma_{UW}(y', z')$ are calculated as

$$\begin{aligned}
\frac{\partial \sigma_{UW}}{\partial x'}\Big|_{y'=\frac{\pi}{4}, z'=0} &= 0 && (3.29)\\
\frac{\partial \sigma_{UW}}{\partial y'}\Big|_{y'=\frac{\pi}{4}, z'=0} &= \frac{(3/8)\pi}{[(\frac{\pi}{4})^2 + \mu^2][(\frac{\pi}{2})^2 + \mu^2]} && (3.30)\\
\frac{\partial \sigma_{UW}}{\partial z'}\Big|_{y'=\frac{\pi}{4}, z'=0} &= 0 && (3.31)
\end{aligned}$$

and the partial derivatives for $\sigma_{SW}(y', z')$ are calculated as

$$
\begin{aligned}
\frac{\partial \sigma_{SW}}{\partial x'}\Big|_{y'=\frac{\pi}{4},z'=0} &= 0 && (3.32)\\
\frac{\partial \sigma_{SW}}{\partial y'}\Big|_{y'=\frac{\pi}{4},z'=0} &= \frac{\frac{1}{2}(\frac{h_z}{b})^2}{[(\frac{\pi}{8})^2+\mu^2]\,[(\frac{\pi}{8})^2+(\frac{h_z}{b})^2+\mu^2]} \\
&\quad -\frac{\frac{3}{2}(\frac{h_z}{b})^2}{[(\frac{3\pi}{8})^2+\mu^2]\,[(\frac{3\pi}{8})^2+(\frac{h_z}{b})^2+\mu^2]} && (3.33)\\
\frac{\partial \sigma_{SW}}{\partial z'}\Big|_{y'=\frac{\pi}{4},z'=0} &= \frac{-(\frac{\pi}{2})(\frac{h_z}{b})}{[(\frac{\pi}{8})^2+\mu^2+(\frac{h_z}{b})^2]\,[(\frac{3\pi}{8})^2+\mu^2+(\frac{h_z}{b})^2]} && (3.34)
\end{aligned}
$$

Inserting the above derivatives into the change in drag, lift, and side force coefficients expressions yields

$$\Delta C_{D_{W_x}} = \Delta C_{L_{W_x}} = \Delta C_{Y_{W_x}} = \Delta C_{D_{W_z}} = \Delta C_{L_{W_z}} = 0$$

$$\Delta C_{D_{W_y}} = \frac{1}{\pi A_R} C_{L_W}^2 \frac{(3/8)\pi}{[(\frac{\pi}{4})^2+\mu^2][(\frac{\pi}{2})^2+\mu^2]} \tag{3.35}$$

$$\Delta C_{L_{W_y}} = \frac{1}{\pi A_R} a C_{L_W} \frac{(3/8)\pi}{[(\frac{\pi}{4})^2+\mu^2][(\frac{\pi}{2})^2+\mu^2]} \tag{3.36}$$

$$
\begin{aligned}
\Delta C_{Y_{W_y}} &= \frac{1}{\pi A_R}\frac{\eta S_{vt} a_{vt} h_z}{4Sb} C_{L_L} \cdot && (3.37)\\
&\left[\frac{1}{[(\frac{\pi}{8})^2+\mu^2]\,[(\frac{\pi}{8})^2+(\frac{h_z}{b})^2+\mu^2]} - \frac{3}{[(\frac{3\pi}{8})^2+\mu^2]\,[(\frac{3\pi}{8})^2+(\frac{h_z}{b})^2+\mu^2]}\right]
\end{aligned}
$$

$$\Delta C_{Y W_z} = -\frac{1}{\pi A_R}\frac{\eta S_{vt} a_{vt}}{2S} C_{L_L} \frac{(\frac{\pi}{2})(\frac{h_z}{b})}{[(\frac{\pi}{8})^2+\mu^2+(\frac{h_z}{b})^2]\,[(\frac{3\pi}{8})^2+\mu^2+(\frac{h_z}{b})^2]} \tag{3.38}$$

3.3.2 Modified Wing Aircraft Control System. Based on the above derived stability derivatives associated with the forces created by the upwash and sidewash, the new Wing FCS is

$$
\begin{aligned}
\dot{V}_W &= -\frac{1}{\tau_V} V_W + \frac{1}{\tau_V} V_{W_c} + \frac{\bar{q}S}{m}\Delta C_{D_{W_y}} y && (3.39)\\
\ddot{h}_W &= -\left(\frac{1}{\tau_{h_a}} + \frac{1}{\tau_{h_b}}\right)\dot{h}_W - \frac{1}{\tau_{h_a}\tau_{h_b}} h_W + \frac{1}{\tau_{h_a}\tau_{h_b}} h_{W_c} + \frac{\bar{q}S}{m}\Delta C_{L_{W_y}} y && (3.40)\\
\dot{\psi}_W &= -\frac{1}{\tau_{\psi_W}}\psi_W + \frac{1}{\tau_{\psi_W}}\psi_{W_c} + \frac{\bar{q}S}{mV}\left[\Delta C_{Y_{W_y}} y + \Delta C_{Y_{W_z}} z\right] && (3.41)
\end{aligned}
$$

where $\Delta C_{D_{W_y}}$, $\Delta C_{L_{W_y}}$, $\Delta C_{Y_{W_y}}$, and $\Delta C_{Y_{W_z}}$ are the new close formation stability derivatives.

3.4 Summary

The average upwash and sidewash effects from the Lead vortex on the Wing aircraft's wing were developed. These effects were then used to derive the change in drag, change in lift, and change in sideforce, ΔD, ΔL, and ΔY, respectively. New close formation stability derivatives were developed and the Wing FCS was modified to account for the additional aerodynamic forces exerted by the Lead's vortex on the Wing.

IV. Control Design and Evaluation

The complete linear and nonlinear system models are developed in this chapter. The method for determining the best gains for the close FFC is described. Finally, a stability and robustness analysis is performed for the complete system using these gains.

4.1 Complete System Model

Equations (3.39) - (3.41) are adjoined to the nonlinear kinematics Equations (2.22) - (2.24) where Equation (3.41) for $\dot{\psi}$ is inserted into the x and y separation differential equations, yielding the hybrid nonlinear six-dimensional close formation flight control system:

$$\begin{aligned}\dot{x} &= -\frac{y}{\tau_{\psi_W}}\psi_W - V_W + V_L cos(\psi_L - \psi_W) + \frac{y}{\tau_{\psi_W}}\psi_{W_c} + \\ &\quad y\frac{\bar{q}S}{mV_W}\left[\Delta C_{Y_{W_y}}(y - \bar{y}) + \Delta C_{Y_{W_z}}(z - \bar{z})\right]\end{aligned} \tag{4.1}$$

$$\begin{aligned}\dot{y} &= \frac{x}{\tau_{\psi_W}}\psi_W + V_L sin(\psi_L - \psi_W) - \frac{x}{\tau_{\psi_W}}\psi_{W_c} - \\ &\quad x\frac{\bar{q}S}{mV_W}\left[\Delta C_{Y_{W_y}}(y - \bar{y}) + \Delta C_{Y_{W_z}}(z - \bar{z})\right]\end{aligned} \tag{4.2}$$

$$\dot{V}_W = -\frac{1}{\tau_V}V_W + \frac{1}{\tau_V}V_{W_c} + \frac{\bar{q}S}{m}\Delta C_{D_{W_y}}(y - \bar{y}) \tag{4.3}$$

$$\dot{\psi}_W = -\frac{1}{\tau_{\psi_W}}\psi_W + \frac{1}{\tau_{\psi_W}}\psi_{W_c} + \frac{\bar{q}S}{mV_W}\left[\Delta C_{Y_{W_y}}(y - \bar{y}) + \Delta C_{Y_{W_z}}(z - \bar{z})\right] \tag{4.4}$$

$$\dot{z} = \zeta \tag{4.5}$$

$$\begin{aligned}\dot{\zeta} &= -\left(\frac{1}{\tau_{h_a}} + \frac{1}{\tau_{h_b}}\right)\zeta - \frac{1}{\tau_{h_a}\tau_{h_b}}z + \frac{1}{\tau_{h_a}\tau_{h_b}}h_{W_c} - -\frac{1}{\tau_{h_a}\tau_{h_b}}h_{L_c} + \\ &\quad \frac{\bar{q}S}{m}\Delta C_{L_{W_y}}(y - \bar{y})\end{aligned} \tag{4.6}$$

where the vertical separation $z = h_W - h_L$ and the Wing and Lead aircraft are assumed to have the same vertical dynamics.

The six states are $x, y, \psi_W, V_W, z,$ and ζ. The three control inputs to the respective Wing's Heading hold, Mach hold, and Altitude hold autopilot channels are ψ_{W_C}, V_{W_C}, and h_{W_C}. The Lead's control inputs are viewed as a disturbance; thus, the disturbance signals are ψ_L, V_L, and h_{L_c}. This is the full nonlinear model used in the simulation. For the purpose of controller design, linearization of the above hybrid system yields the linear perturbation equations

$$\begin{aligned}
\dot{x} &= -\frac{\bar{y}}{\tau_{\psi_W}}\psi_W - V_W + V_L + \frac{\bar{y}}{\tau_{\psi_W}}\psi_{W_c} + \bar{y}\frac{\bar{q}S}{m\bar{V}}\left[\Delta C_{Y_{W_y}}y + \Delta C_{Y_{W_z}}z\right] \tag{4.7}\\
\dot{y} &= \left(\frac{\bar{x}}{\tau_{\psi_W}} - \bar{V}\right)\psi_W + \bar{V}\psi_L - \frac{\bar{x}}{\tau_{\psi_W}}\psi_{W_c} - \bar{x}\frac{\bar{q}S}{m\bar{V}}\left[\Delta C_{Y_{W_y}}y + \Delta C_{Y_{W_z}}z\right] \tag{4.8}\\
\dot{V}_W &= -\frac{1}{\tau_V}V_W + \frac{1}{\tau_V}V_{W_c} + \frac{\bar{q}S}{m}\Delta C_{D_{W_y}}y \tag{4.9}\\
\dot{\psi}_W &= -\frac{1}{\tau_{\psi_W}}\psi_W + \frac{1}{\tau_{\psi_W}}\psi_{W_c} + \frac{\bar{q}S}{m\bar{V}}\left[\Delta C_{Y_{W_y}}y + \Delta C_{Y_{W_z}}z\right] \tag{4.10}\\
\dot{z} &= \zeta \tag{4.11}\\
\dot{\zeta} &= -\left(\frac{1}{\tau_{h_a}} + \frac{1}{\tau_{h_b}}\right)\zeta - \frac{1}{\tau_{h_a}\tau_{h_b}}z + \frac{1}{\tau_{h_a}\tau_{h_b}}h_{W_c} + \frac{\bar{q}S}{m}\Delta C_{L_{W_y}}y - \frac{1}{\tau_{h_a}\tau_{h_b}}h_{L_c} \tag{4.12}
\end{aligned}$$

The resulting state space representation based on the above defined states, controls, and disturbances is

$$\frac{d}{dt}\begin{bmatrix} x \\ V_W \\ y \\ \psi_W \\ z \\ \zeta \end{bmatrix} = A\begin{bmatrix} x \\ V_W \\ y \\ \psi_W \\ z \\ \zeta \end{bmatrix} + B\begin{bmatrix} V_{W_c} \\ \psi_{W_c} \\ h_{W_c} \end{bmatrix} + \Gamma\begin{bmatrix} V_L \\ \psi_L \\ h_{L_c} \end{bmatrix} \tag{4.13}$$

where the dynamics matrix

$$A = \begin{bmatrix}
0 & -1 & \vdots & \frac{\bar{q}S}{m\bar{V}}\Delta C_{Y_{W_y}}\bar{y} & -\frac{\bar{y}}{\tau_{\psi_W}}G & \frac{\bar{q}S}{m\bar{V}}\Delta C_{Y_{W_z}}\bar{y} & 0 \\
0 & -\frac{1}{\tau_{V_W}} & \vdots & \frac{\bar{q}S}{m}\Delta C_{D_{W_y}} & 0 & 0 & 0 \\
\cdots & \cdots & \cdots & \cdots & \cdots & \cdots & \cdots \\
0 & 0 & \vdots & \frac{\bar{q}S}{m\bar{V}}\Delta C_{Y_{W_y}}\bar{x} & \left(\frac{\bar{x}}{\tau_{\psi_W}} - \bar{V}_L\right)G & -\frac{\bar{q}S}{m\bar{V}}\Delta C_{Y_{W_z}}\bar{x} & 0 \\
0 & 0 & \vdots & \frac{\bar{q}S}{m\bar{V}}\Delta C_{Y_{W_y}}1/G & -\frac{1}{\tau_{\psi_V}} & \frac{\bar{q}S}{m\bar{V}}\Delta C_{Y_{W_z}}1/G & 0 \\
0 & 0 & \vdots & 0 & 0 & 0 & 1 \\
0 & 0 & \vdots & \frac{\bar{q}S}{m}\Delta C_{L_{W_y}} & 0 & -\frac{1}{\tau_{h_a}\tau_{h_b}} & -\left(\frac{1}{\tau_{h_a}} + \frac{1}{\tau_{h_b}}\right)
\end{bmatrix} \tag{4.14}$$

the input matrix

$$B = \left[\begin{array}{c c c c} 0 & \vdots & \frac{\bar{y}}{\tau_{\psi_W}}G & 0 \\ \frac{1}{\tau_{V_W}} & \vdots & 0 & 0 \\ \cdots & \vdots & \cdots & \cdots \\ 0 & \vdots & -\frac{\bar{x}}{\tau_{\psi_W}}G & 0 \\ 0 & \vdots & \frac{1}{\tau_{\psi_W}} & 0 \\ 0 & \vdots & 0 & 0 \\ 0 & \vdots & 0 & \frac{1}{\tau_{h_a}\tau_{h_b}} \end{array}\right] \tag{4.15}$$

and the disturbance matrix is

$$\Gamma = \left[\begin{array}{c c c} 1 & 0 & 0 \\ 0 & 0 & 0 \\ 0 & \bar{V}_L G & 0 \\ 0 & 0 & 0 \\ 0 & 0 & 0 \\ 0 & 0 & -\frac{1}{\tau_{h_a}\tau_{h_b}} \end{array}\right] \tag{4.16}$$

and where the number $G = \pi/180$ and is used to keep consistency among units. The block diagram for the above linearized system, Equations (4.14) - (4.16) is shown in Figure 4.1.

The dynamics A matrix shows that there is additional coupling introduced to the system above and beyond the kinematically induced coupling. This is especially evident in the $A_{6,3}$ term which couples the y separation into the altitude hold autopilot and the $A_{3,5}$ term which couples the z separation into the heading hold autopilot. The heading is kinematically coupled into the y separation equation and the y separation is aerodynamically coupled into the Mach-hold autopilot, terms $A_{3,5}$ and $A_{1,3}$ respectively. This leads to an indirect coupling between the z separation and the Mach-hold autopilot. There is no coupling between the horizontal and vertical channels for a large formation. This interaction between channels is one of the most interesting effects of close formation flight and is discussed further in Chapter V.

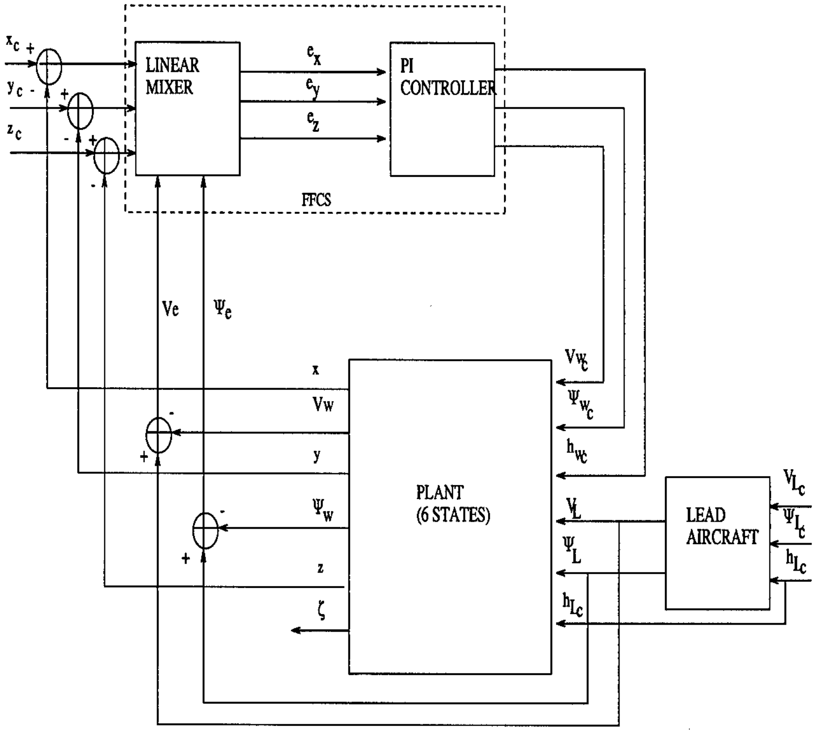

Figure 4.1 Linearized System and Formation Flight Controller

Typical characteristics for an F-16 class aircraft are listed in Table 4.1 for an altitude of 45,000 ft, velocity of 0.85 Mach, and a dynamic pressure of 155.8 lbs/ft^2. The close formation stability derivatives for this flight condition and the associated characteristics are listed in Table 4.2.

The dynamic A matrix evaluated for the typical characteristics listed in Table 4.1 and the nominal $\bar{x}$, $\bar{y}$, and $\bar{z}$ separations listed above, with no close formation induced aerodynamic coupling effects, is

$$A = \begin{bmatrix} 0 & -1.0000 & 0 & -0.3084 & 0 & 0 \\ 0 & -6.0000 & 0 & 0 & 0 & 0 \\ 0 & 0 & 0 & -13.6136 & 0 & 0 \\ 0 & 0 & 0 & -0.7500 & 0 & 0 \\ 0 & 0 & 0 & 0 & 0 & 1.0000 \\ 0 & 0 & 0 & 0 & -0.8447 & -3.5118 \end{bmatrix} \quad (4.17)$$

The dynamic A matrix evaluated for the data listed in Table 4.1 and the nominal $\bar{x}$, $\bar{y}$, and $\bar{z}$ separations with the close formation coupling effects included is

$$A = \begin{bmatrix} 0 & -1.0000 & 0.0057 & -0.3084 & -0.0020 & 0 \\ 0 & -6.0000 & -0.0471 & 0 & 0 & 0 \\ 0 & 0 & -0.0144 & -13.6136 & 0.0050 & 0 \\ 0 & 0 & 0.0138 & -0.7500 & 0.0138 & 0 \\ 0 & 0 & 0 & 0 & 0 & 1.0000 \\ 0 & 0 & 0.4663 & 0 & -0.8447 & -3.5118 \end{bmatrix} \tag{4.18}$$

It can be seen from a comparison of Eqs. (4.17) and (4.18) that the coupling terms introduced by the close formation are small. One notable exception is $A_{6,3} = 0.4663$. This justifies the use of the large formation controller since this is essentially a three channel system, although special care is required in the z-channel controller design.

Table 4.1 F-16 Class Aircraft Characteristic Values This data corresponds to the following flight condition: Altitude of 45,000 ft, dynamic pressure 155.8 lb/ft^2

Wing Area	S	300 ft^2
Wing Span	b	30 ft
Aspect Ratio	A_R	3
Lift Curve Slope	a	5.3 per rad
Tail Area	S_{vt}	54.75 ft^2
Tail Height	h_z	120 in
Tail Lift Curve Slope	a_{vt}	5.3 per rad
Aerodynamic Efficiency Factor	η	0.95
Velocity Time Constant	τ_{V_W}	5 sec
Heading Time Constant	τ_{ψ_W}	0.75 sec
Altitude Time Constant	h_a	0.3075 sec
Altitude Time Constant	h_b	3.85 sec
Gross Mass	m	776.4 slugs
Gross Weight	w	25000 lb
Velocity	$\bar{V}$	Mach = 0.85 or 825 ft/sec

Table 4.2 Close Formation Stability Derivatives for $\bar{y} = \frac{\pi}{4}b$ and $\bar{z} = 0$

$\Delta C_{D_{W_y}}$	-0.000782
$\Delta C_{L_{W_y}}$	-0.0077
$\Delta C_{Y_{W_y}}$	0.0033
$\Delta C_{Y_{W_z}}$	-0.0011

4.2 Control Design

Similar to the large FFC system, note that the y and z channel states y, ψ_W, z, and ζ, are decoupled from the x channel states, x, and V_W; which is easily seen in Equation 4.14. Hence, one first designs a controller for the y and z channels, where the control signals are ψ_{W_c} and h_{W_c}, following which one turns to the design of the x-channel controller, viz., one synthesizes the control law for the V_{W_c} control signal. Furthermore, even though the (y,z) model does not further decompose into individual y and z channels as in [8] where the coupling is exclusively induced by the kinematics of the large FFC, the same controller will be applied because the close formation induced coupling is weak.

The controller contains a linear mixer on the x and y channels and a standard PI compensator on the x-, y- and z-channels. The FFC Equations 2.31 - 2.33 developed in Chapter II are repeated below.

$$\begin{aligned}
V_{WC}(t) &= K_{X_p}[k_V V_E + k_x \Delta x_E] + K_{X_I}\int_0^t [k_V V_E + k_x \Delta x_E]dt \\
\psi_{WC}(t) &= K_{Y_p}[k_\psi \psi_E + k_y \Delta y_E] + K_{Y_I}\int_0^t [k_\psi \psi_E + k_y \Delta y_E]dt \\
h_{WC}(t) &= K_{Z_p} k_z \Delta z_E + K_{Z_I}\int_0^t k_z \Delta z_E dt
\end{aligned}$$

The FFC gains have been choosen based on the three criteria listed below:

- The maximum positive and negative perturbations from nominal for a single channel should be approximately equal for any heading maneuver within the test envelope defined; e.g., the y separation for a $-30°$ heading change ranges from a minimum of 20.5 ft to a maximum of 26.3 ft or -3 ft and 2.8 ft from nominal respectively. The deviation to the right is approximately equal to the deviation to the left.
- The responses should be consistent for either a positive or a negative change in either the heading, the velocity, or the altitude; e.g., a -30 degree heading change will cause a maximum error of 4 ft in x and 3 ft in the y and a +30 degree heading change will

cause a maximum error of 3.3 ft in the x and 3 ft in the y. Both maneuvers result in errors of approximately the same magnitude.

- The Wing aircraft should not cross over the $\hat{x}$ or $\hat{y}$ axes. This criterion has the dual effect of preventing collisions between the Lead and the Wing; also in a formation containing both a left and right Wing aircraft.

Previous AFIT students [6],[12] used SISO techniques to determine the gains. The method consisted of successively closing loops to create a new A matrix. After each loop closure, the new A plant matrix is used for the next loop closure. Once the appropriate loops were closed, the root locus was used to iteratively determine the best gains to achieve the desired performance. Even though this method is not completely rigorous for a MIMO system, it does give a good indication of gain magnitudes and system response.

4.2.1 Gain Selection Method. A simple systematic approach was used to iteratively determine the best gains. First, only the completely linearized system as shown in Equations 4.7 - 4.12 and in Figure 4.1 is considered. With the cross coupling terms zeroed out, Dargan's gains were chosen as the starting point [3]. The system is subjected to a positive and negative velocity change and the horizontal channel gains are adjusted. The system is then subject to a positive and negative heading change and the horizontal gains are adjusted. Lastly, the system is subjected to a positive and negative altitude change and the vertical channel gains are adjusted. The order of gain adjustment can affect the number of iterations required to determine the best gains. The best order of gain adjustment, i.e., the method which results in the fewest iterations, was to adjust the mixer gains first, to achieve the best maneuver tracking response, and then adjust the PI compensator gains to achieve the best formation response. Once the best gains are determined for the complete linear system with no coupling, the next step is to add back the linear cross coupling terms. Finally, apply these gains to the full non-linear model shown in Figure 4.17 and adjust the gains for the best response.

4.2.2 Gain Selection. The Six cases used for gain selection are: +/-50 ft/sec velocity change, +/- 30° heading change, and +/-1000 ft change in altitude. Figures 4.2 and 4.3 show the responses of the system using the large FFC with Dargan's gains for a

50 ft/sec change in velocity. Figures 4.4 and 4.5 show the system responses for a $-30°$ heading change using Dargan's gains. Figures 4.6 - 4.7 show the response for a 1000 ft increase in altitude.

The format for the time response plots and the Lissajous plots is described here. The time plots contain six subplots. In the top three subplots, the solid line represents the Lead aircraft and the dashed line represents the Wing aircraft. In some cases only a solid line is visible, this is due to the overlap of the responses from the Lead and the Wing. In the bottom three subplots, the solid line represents the nominal separation values and the dashed line represents the actual values. Starting points in the Lissajous plots are represented by an 'O' and the ending points are represented by an 'X'. This format is used for each plot listed in the following sections.

As expected, Dargan's large FFCS gains resulted in poor performance for a close formation. A velocity decrease of 50 ft/sec, Figures 4.2 and 4.3 resulted in a long delay before the Wing's velocity responded to the Lead's velocity. This delay causes the Wing to overtake the Lead, but since the Lead's wing and the Wing's wing overlap and both aircraft are at the same altitude, a collision occurs. This is easily seen when the separation in the $\hat{x}$ direction decreases to zero, crosses the $\hat{y}$ axis, and becomes negative. A $-30°$ heading change resulted in a maximum deviation of 4 ft ($\approx \frac{1}{7}$b) in the $\hat{x}$ direction and a maximum deviation of 41 ft ($\approx 1\frac{1}{3}$ b) in the $\hat{y}$ direction, see Figures 4.4 and 4.5. The deviation in the $\hat{y}$ direction crossed the x axis. This would most likely have resulted in a collision for the case of two Wingmen. The responses to an increase in altitude of 1000 ft using Dargan's large FFCS gains is shown in Figures 4.6 - 4.7. The altitude also suffered from a long delay before the Wing responded to the Lead's ascent. The separation in the $\hat{z}$ direction grew to over 400 ft ($\approx$ 13b). No collision would occur, but the enormous error is still not acceptable for close formation flight. Therefore, all three maneuver responses are unacceptable for close formation flight and require the gains to be adjusted.

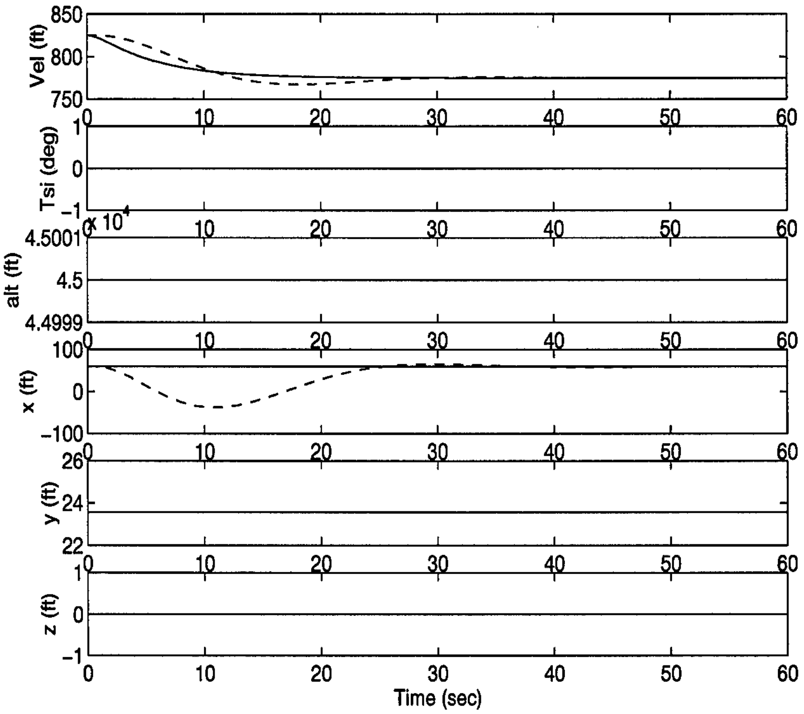

Figure 4.2 50 ft/sec Velocity Decrease Time Plot Using Dargan Gains

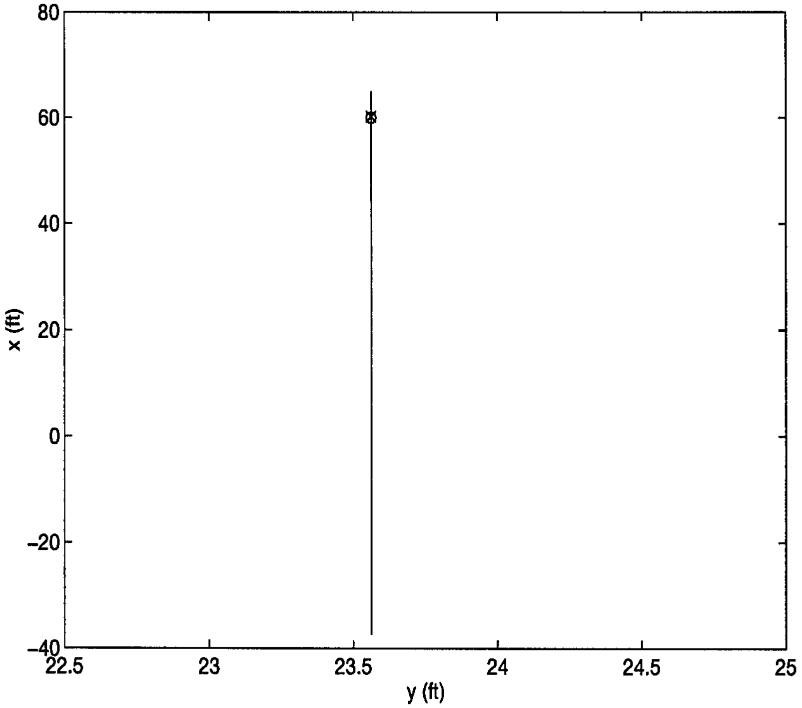

Figure 4.3 50 ft/sec Velocity Decrease Lissajous Plot Using Dargan Gains

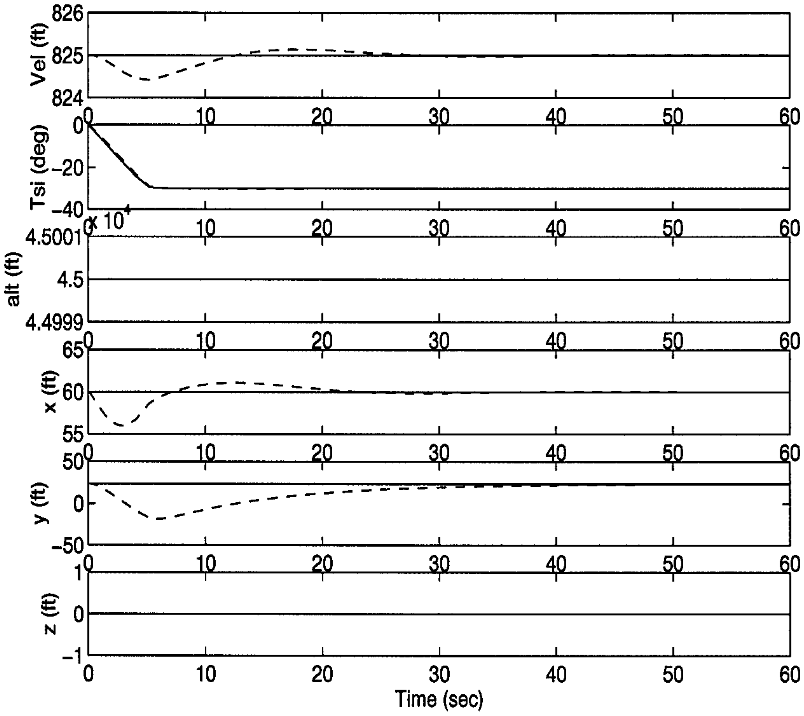

Figure 4.4 Negative 30 Degree Heading Change Plot Using Dargan Gains

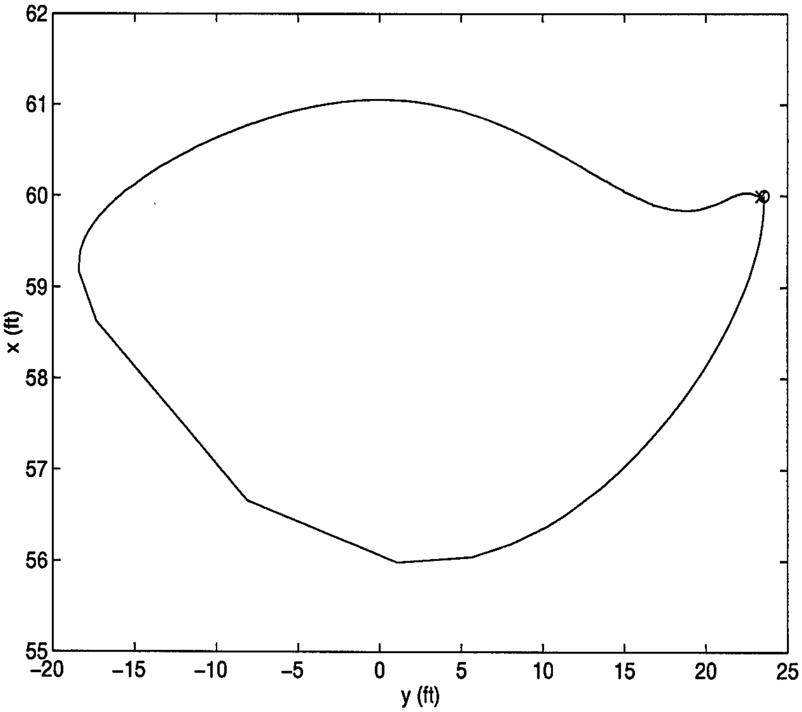

Figure 4.5 Negative 30 Degree Heading Change Lissajous Plot Using Dargan Gains

With the system responses from Dargan's gains as the baseline, adjustment of the x-channel was chosen first for the close FFC. Since, it is independent of the other channels when only a velocity change occurs, it should be the easiest of the two horizontal channels to determine the gains. Using the Dargan gain response as the baseline, the system was subjected to a 50 ft/sec change in velocity. The velocity error gain (k_V) was increased to get the Wing velocity to track closely with the Lead. Once, the best velocity response was achieved the x separation error gain (k_x) was increased to get the best x separation response. Both of these gains reached a certain limit in which further increase resulted in degraded performance. Once this point was achieved the x channel proportional gain (K_{X_P}) was adjusted to give the best x separation response. This gain also reached a limit in which further increase resulted in degraded performance. The x separation looked like an elongated bell sitting on the line marking the nominal x value. This shape indicates that the gain on the integrator was too small because the error continued to build up for a long time and then took a long time to decay. Therefore, the x channel integration gain (K_{X_I}) was increased. The combined effect of all gain adjustments resulted in an initial ramp like increase in x separation error, but with a much smaller magnitude, then a quick dropoff back to the nominal x separation distance. This was first done for an increase in velocity. The gains were then readjusted to get the best average response for both an increase and decrease in velocity to fulfill the second gain criterion.

These new gains provided the starting point for the next phase. This phase consisted of inputting a heading change. This was a little trickier since heading changes affect both the y- and x-channels simultaneously. However, applying the same approach as above worked well. First, the heading error gain (k_ψ) was adjusted to track the Lead's heading as closely as possible. The velocity and x separation responses degraded slightly from the heading gain adjustment and required a slight re-adjustment of the velocity and the x error gains (k_V and k_x). The y error gain (k_y) was then adjusted. Then the proportional y channel gain (K_{Y_P}) and finally the integral y channel gain (K_{Y_I}) was adjusted. This method worked well and was rather logical with respect to the system responses for each step.

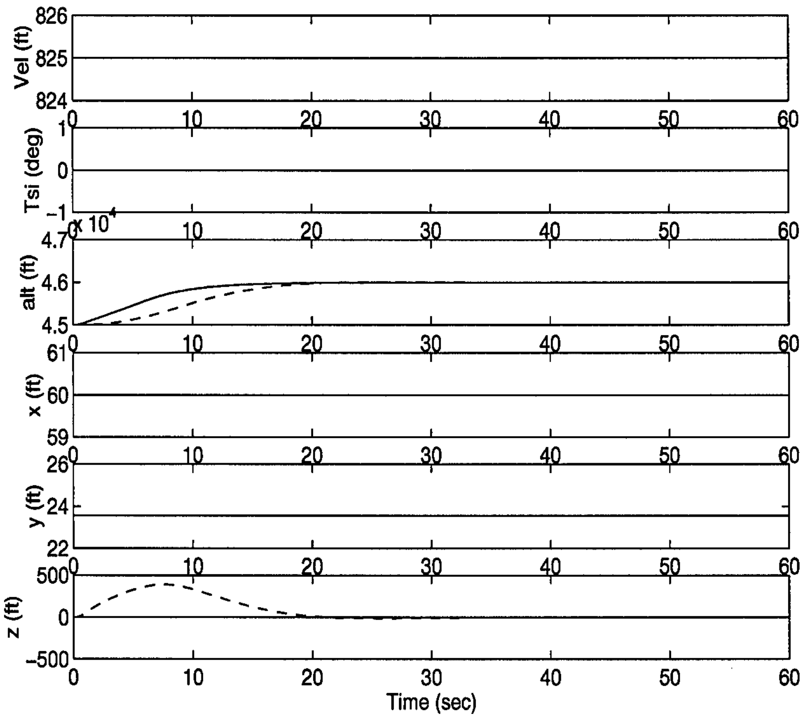

Figure 4.6 1000 ft Altitude Increase Plot Using Dargan Gains

The adjustments of the z channel gains were almost trivial with respect to the x- and y-channels. It required the adjustment of three gains, even though adjustment of the linear mixer gain (k_z) is the same as adding an equal gain to both the proportional (K_{Z_P}) and integral (K_{Z_I}) z error gains. First, the z error gain (k_z) was increased to achieve a good response. The proportional (K_{Z_P}) gain was then increased to improve the response. The result of these two adjustments was the best response and did not require any further adjustment of the integral gain (K_{Z_I}). SISO root locus methods would also have worked well for determining the best gains for this channel.

The simulations were then run again using the nonlinear kinematics Equations (4.1) - (4.7) and no cross coupling to determine if the gains determined in the previous run needed further adjustments. Adjustments were not needed. Finally, cross coupling terms were included; again, gain adjustments were not necessary. The final gain values are listed in Table 4.3.

Table 4.3 FFCS Gain Values

FFCS Gains	Numerical Value
Linear Mixer	
k_V	12.5
k_ψ	6
k_x	-8.0 sec^{-1}
k_y	-0.6 deg/ft
k_z	25
PI Compensator	
K_{X_P}	6
K_{X_I}	0.4
K_{Y_P}	11
K_{Y_I}	0.9
K_{Z_P}	4
K_{Z_I}	0.5

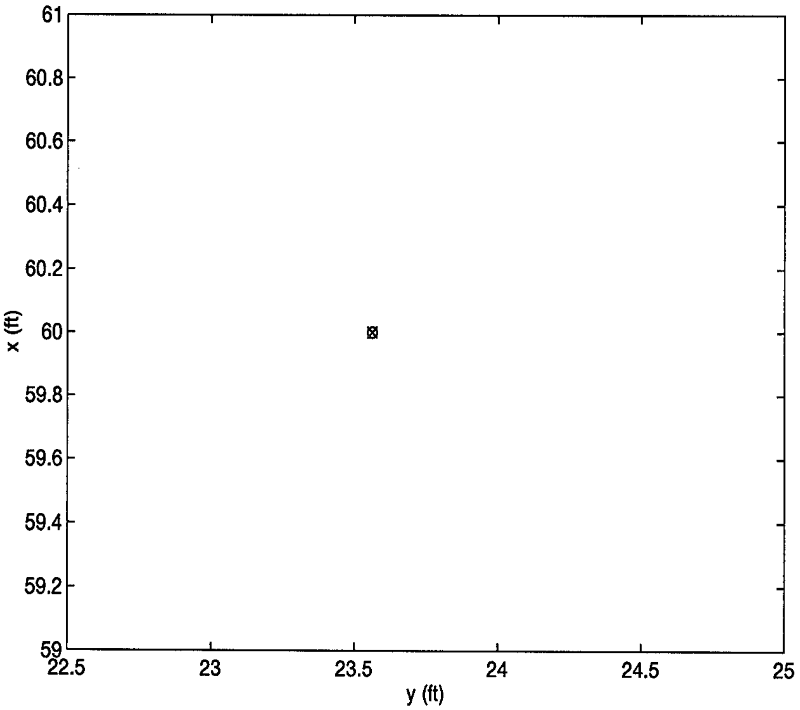

Figure 4.7 1000 ft Altitude Increase Lissajous Plot Using Dargan Gains

4.3 Stability

In order to determine the stability of the closed loop system, the linearized plant and controller must be combined together in an augmented closed loop plant. The eigenvalues of this new system should indicate whether or not the complete linear system is stable. The actual formation flight controller is composed of nonlinear saturation limits associated with the FCS. For this reason, stability cannot be guaranteed, but for the operating envelope defined, it is a good indication of system stability.

Since the FFCS consists of a linear mixer feeding into a three channel PI controller, three more states are needed for the augmented matrix. The three augmented states are

$$\dot{\alpha} = k_V\left(V_L - V_W\right) + k_x\left(x_c - x\right) = e_X \tag{4.19}$$

$$\dot{\beta} = k_\psi\left(\psi_L - \psi_W\right) + k_y\left(y_c - y\right) = e_Y \tag{4.20}$$

$$\dot{\gamma} = k_z\left(z_c - z\right) = e_Z \tag{4.21}$$

where, α, β, and γ are not related to the angle of attack, the sideslip angle, or the flight path angle. The new states are the outputs of the respective integrator for each channel's PI controller as shown in Figure 2.11. The input commands, Equations (2.31) - (2.33) are now solved using these new states. The resulting equations are

$$V_{W_c} = K_{X_I}\alpha + K_{X_P}k_V\left(V_L - V_W\right) + K_{P_x}k_x\left(x_c - x\right) \tag{4.22}$$

$$\psi_{W_c} = K_{Y_I}\beta + K_{Y_P}k_\psi\left(\psi_L - \psi_W\right) + K_{Y_P}k_y\left(y_c - y\right) \tag{4.23}$$

$$h_{W_c} = K_{Z_I}\gamma + K_{Z_P}k_z\left(z_c - z\right) \tag{4.24}$$

Equations (4.19) - (4.21) are augmented to Equations (4.7) - (4.12) and the new input Equations (4.22) - (4.24) are substituted into Equations (4.7) - (4.12). This creates a new nine state system. The new inputs are x_c, y_c, and z_c and the Lead is again treated as a disturbance. The resulting state space representation based on the augmented states, controls, and disturbances is

$$\frac{d}{dt}\begin{bmatrix} x \\ V_W \\ y \\ \psi_W \\ z \\ \zeta \\ \alpha \\ \beta \\ \gamma \end{bmatrix} = A_{cl}\begin{bmatrix} x \\ V_W \\ y \\ \psi_W \\ z \\ \zeta \\ \alpha \\ \beta \\ \gamma \end{bmatrix} + B\begin{bmatrix} x_c \\ y_c \\ z_c \end{bmatrix} + \Gamma\begin{bmatrix} V_L \\ \psi_L \\ h_{Lc} \end{bmatrix} \tag{4.25}$$

where the A_{cl} is arbitrarily broken into A_{cl1} and A_{cl2}, and B_{cl}, and Γ_{cl} matrices are, respectively,

$$A_{cl} = [A_{cl1}A_{cl2}] \tag{4.26}$$

$$A_{cl1} = \begin{bmatrix} 0 & -1 & \bar{y}\left(\frac{\bar{q}S}{m\bar{V}}\Delta C_{Y_{W_y}} - G\frac{K_{Y_P}K_y}{\tau_{\psi_W}}\right) & -\frac{\bar{y}}{\tau_\psi}(1+K_{Y_P}K_\psi)G \\ -\frac{K_{X_P}K_x}{\tau_V} & -\frac{1}{\tau_V}(1+K_{X_P}K_V) & \frac{\bar{q}S}{m}\Delta C_{D_{W_y}} & 0 \\ 0 & 0 & \bar{x}\left(\frac{K_{Y_P}K_y}{\tau_{\psi_W}}G - \frac{\bar{q}S}{m\bar{V}}\Delta C_{Y_{W_y}}\right) & \left(\frac{\bar{x}}{\tau_{\psi_W}} - \bar{V} + \frac{\bar{x}K_{Y_P}K_\psi}{\tau_{\psi_W}}\right)G \\ 0 & 0 & \left(-\frac{K_{Y_P}K_y}{\tau_{\psi_W}} + \frac{\bar{q}S}{m\bar{V}}\Delta C_{Y_{W_y}}(1/G)\right) & -\frac{1}{\tau_{\psi_W}}(1+K_{Y_P}K_y) \\ 0 & 0 & 0 & 0 \\ 0 & 0 & \frac{\bar{q}S}{m}\Delta C_{L_{W_y}} & 0 \\ -k_x & -k_v & 0 & 0 \\ 0 & 0 & -k_y & -k_\psi \\ 0 & 0 & 0 & 0 \end{bmatrix} \tag{4.27}$$

$$A_{cl2} = \begin{bmatrix} \frac{\bar{q}S}{m\bar{V}}\bar{y}\Delta C_{Y_{W_z}} & 0 & 0 & \frac{K_{Y_I}}{\tau_{\psi_W}}\bar{y}G & 0 \\ 0 & 0 & \frac{K_{X_I}}{\tau_V} & 0 & 0 \\ -\bar{x}\frac{\bar{q}S}{m\bar{V}}\Delta C_{Y_{W_z}} & 0 & 0 & -\frac{\bar{x}K_{Y_I}}{\tau_{\psi_W}}G & 0 \\ \frac{\bar{q}S}{m\bar{V}}\Delta C_{Y_{W_z}}(1/G) & 0 & 0 & \frac{K_{Y_I}}{\tau_{\psi_W}} & 0 \\ 0 & 1 & 0 & 0 & 0 \\ -\left(\frac{1}{\tau_{h_a}\tau_{h_b}} + \frac{K_{Z_P}K_z}{\tau_{h_a}\tau_{h_b}}\right) & -\left(\frac{1}{\tau_{h_a}} + \frac{1}{\tau_{h_b}}\right) & 0 & 0 & \frac{K_{Z_I}k_z}{\tau_{h_a}\tau_{h_b}} \\ 0 & 0 & 0 & 0 & 0 \\ 0 & 0 & 0 & 0 & 0 \\ -k_z & 0 & 0 & 0 & 0 \end{bmatrix} \tag{4.28}$$

$$B_{cl} = \begin{bmatrix} 0 & \bar{y}\frac{K_{Y_P}k_y}{\tau_{\psi_W}} & 0 \\ \frac{K_{X_P}k_x}{\tau_V} & 0 & 0 \\ 0 & -\bar{x}\frac{K_{Y_P}k_y}{\tau_{\psi_W}} & 0 \\ 0 & \frac{K_{Y_P}k_y}{\tau_{\psi_W}} & 0 \\ 0 & 0 & 0 \\ 0 & 0 & \frac{K_{Z_P}}{\tau_{h_a}\tau_{h_b}} \\ K_x & 0 & 0 \\ 0 & k_y & 0 \\ 0 & 0 & k_z \end{bmatrix} \tag{4.29}$$

$$\Gamma_{cl} = \begin{bmatrix} 1 & -\bar{y}\frac{K_{Y_P}k_y}{\tau_{\psi_W}}G & 0 \\ \frac{K_{X_P}K_x}{\tau_V} & 0 & 0 \\ 0 & \left(\bar{V} - \bar{x}\frac{K_{Y_P}k_\psi}{\tau_{\psi_W}}\right)G & 0 \\ 0 & \frac{K_{Y_P}k_\psi}{\tau_{\psi_W}} & 0 \\ 0 & 0 & 0 \\ 0 & 0 & -\frac{1}{\tau_{h_a}\tau_{h_b}} \\ k_v & 0 & 0 \\ 0 & k_\psi & 0 \\ 0 & 0 & 0 \end{bmatrix} \tag{4.30}$$

where the number $G = \pi/180$ and is used to keep consistency among units.

The evaluated A_{cl} for the characteristics in Table 4.1 is

$$A_{cl} = \begin{bmatrix} 0 & -1.0000 & 8.1481 & -82.6581 & -0.0020 & 0 & 0 & 1.1103 & 0 \\ 9.6000 & -15.2000 & 0.0471 & 0 & 0 & 0 & 0.0800 & 0 & 0 \\ 0 & 0 & -20.7490 & 196.0877 & 0.0050 & 0 & 0 & -2.8274 & 0 \\ 0 & 0 & 19.8138 & -201.0000 & -0.0048 & 0 & 0 & 0 & 0 \\ 0 & 0 & 0 & 0 & 0 & 1.0000 & 0 & 0 & 0 \\ 0 & 0 & 0.4663 & 0 & -85.3131 & -3.5118 & 0 & 0 & 0.4223 \\ 8.0000 & -12.5000 & 0 & 0 & 0 & 0 & 0 & 0 & 0 \\ 0 & 0 & 0.6000 & -6.0000 & 0 & 0 & 0 & 0 & 0 \\ 0 & 0 & 0 & 0 & -25.0000 & 0 & 0 & 0 & 0 \end{bmatrix} \tag{4.31}$$

The eigenvalues for the above closed loop dynamics matrix A_{cl} are all in the left half plane and are shown in Table 4.4. Therefore, the system is stable for the selected gains. It is also evident from the system responses shown later in Chapter V that the system is stable.

Table 4.4 Closed Loop Eigenvalues

Eigenvalues
-0.6627
-14.47
-0.0667
-220.37
-1.69 + 9.06i
-1.69 - 9.06i
-1.29
-0.1256
-0.0818

4.4 Robustness

A robust controller is one that responds well to very dynamic plants. It was stated in Chapter I that the window of opportunity for a reduction in drag and increase in lift is small. Since, the change in drag, ΔD, and the change in lift, ΔL, are very complicated 3-dimensional functions, individual slices are shown for both the $\hat{y}$ and $\hat{z}$ directions. The ΔD and ΔL, are proportional; the only difference is the magnitude of the ΔL is about ten times greater than the ΔD. Therefore, all discussions for the ΔD function also apply to the ΔL function.

Figure 4.8 shows a z-slice of the ΔD function at $\bar{z} = 0$. Figure 4.9 shows the rate of change in ΔD evaluated for $\bar{z} = 0$ and $\bar{y}$ varied between 3.5 ft to 43.5 ft or -/+$\frac{2}{3}b$ from nominal, $y = \frac{\pi}{4}b$. It can be seen from these two figures that the nominal operating point is highly dynamic. A slight movement, either to the right or to the left, can cause a large rapid magnitude swing and even a sign change in ΔD. ΔD is almost symmetric with respect to $\bar{y} = \frac{\pi}{4}b$ for small changes in y separation. The function loses it's symmetry as the deviations from nominal exceed $\approx \frac{1}{10}b$. This is easily seen in Figure 4.9 where the left hand side forms a parabola and the right slowly decays to zero. Decreases in y position greater than $\frac{1}{5}b$ cause the Wing aircraft to move into the region in which the effect from the Lead's vortex is downwash instead of upwash. This region is directly between the two filaments composing the horseshoe vortex. However, the vortex never becomes a downwash for an increase in y separation greater than the nominal, but slowly decays to zero upwash.

Figure 4.10 shows the same ΔD function, but sliced in the $\hat{y}$ direction at $\bar{y} = \frac{\pi}{4}b$. Figure 4.11 shows the rate of change in ΔD evaluated for $\bar{y} = \frac{\pi}{4}b$ and $\bar{z}$ varied between -20 ft to 20 ft or -/+$\frac{2}{3}b$ from nominal. It is obvious from these two figures that ΔD is also very dynamic for changes in z, but unlike the z-slice it is perfectly symmetric. The radius for a ΔD benefit is larger for the y-slice, about 55% of the wingspan.

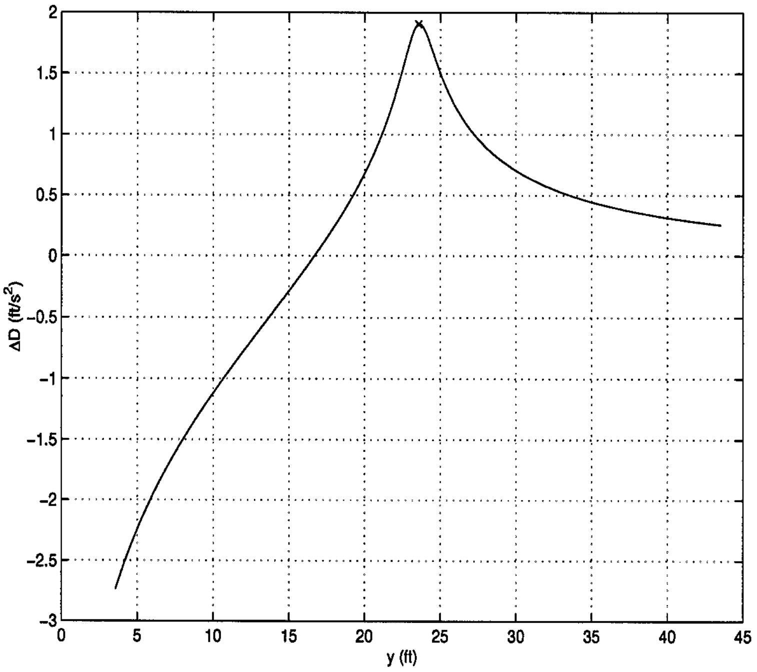

Figure 4.8 Δ D z-slice at $\bar{z} = 0$

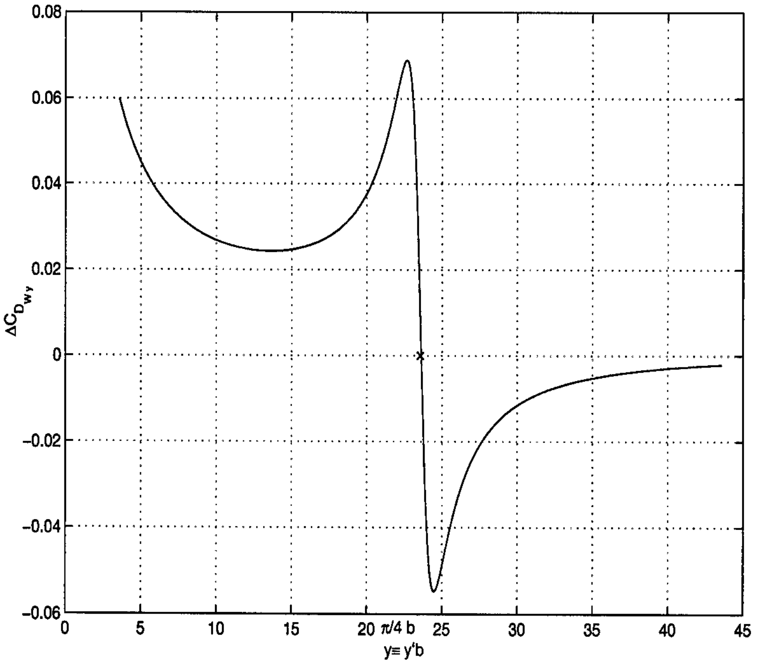

Figure 4.9 Change in ΔD for a change in y evaluated at $\bar{z} = 0$

It can be seen from the z and y slices that the maximum reduction in drag is obtained at the nominal y and z values. Deviations in the y and z positions from this nominal location are compounded. So a combined change in y and z position in the formation results in a larger reduction in ΔD than for an individual change of greater magnitude in either the y or the z positions.

Figure 4.12 shows the actual ΔD function and the first and second order models for the region of $+/-\frac{1}{10}b$ in which ΔD is roughly symmetric. It can be seen, that the first order model truly does trivialize the effect of the upwash. A decrease in the y separation distance causes a small decrease in the ΔD; an increase in the y separation causes a small increase in the ΔD. However, the true response is more like a parabola. A decrease in y separation causes a decrease in ΔD, but it is much faster than the linear version. An increase in the y separation also causes a decrease in the actual ΔD, but the first order model causes an increase in ΔD for an increase in y. The second order model is parabolic like the actual and appears to be better than the first order model for small positive and negative changes in y, but for larger changes the first order model is actually closer to the true response as the second order model becomes increasingly negative. The first order model is truly only accurate for changes in y of 0.25 ft in magnitude. It can also be seen from Figure 4.12, that the first order model is not constant, but has a small slope. The maximum reduction in drag is not exactly at the point $\bar{y} = \frac{\pi}{4}b$ or 23.562 ft, but at 23.612 ft. This shift is caused by the inclusion of the correction term μ. There is no effect on the first and second order ΔD models for a change in z, because $\bar{z} = 0$ at the nominal position.

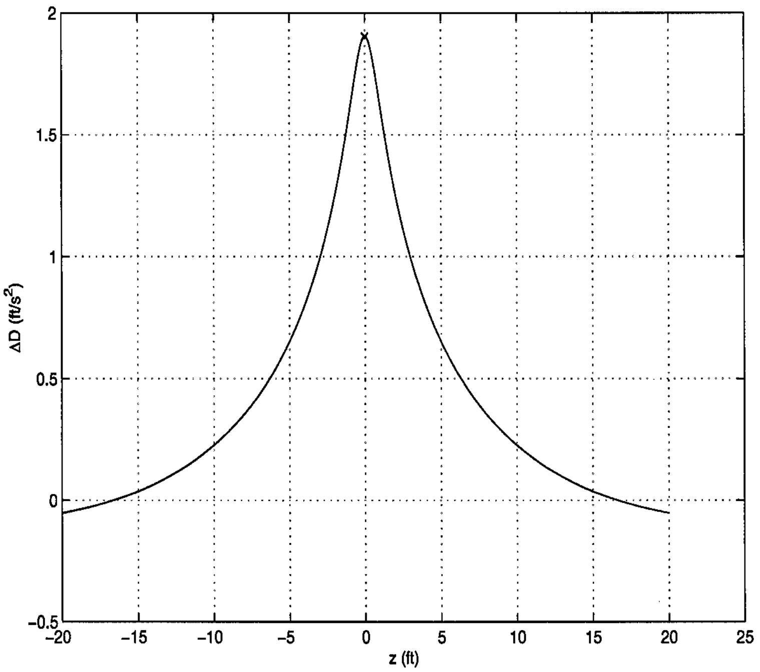

Figure 4.10 Δ D y-slice at $\bar{y} = \frac{\pi}{4}b$

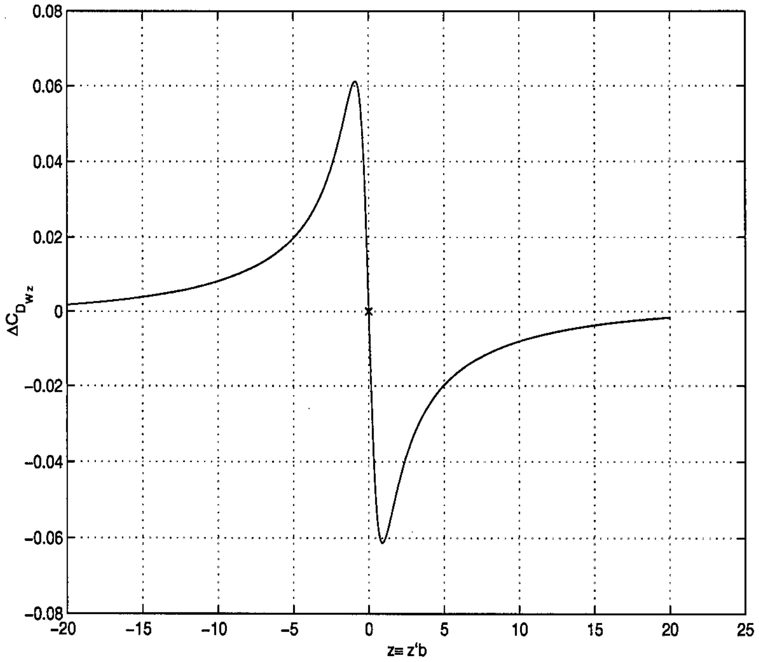

Figure 4.11 Change in ΔD for a change in z evaluated at $\bar{y} = \frac{\pi}{4}b$

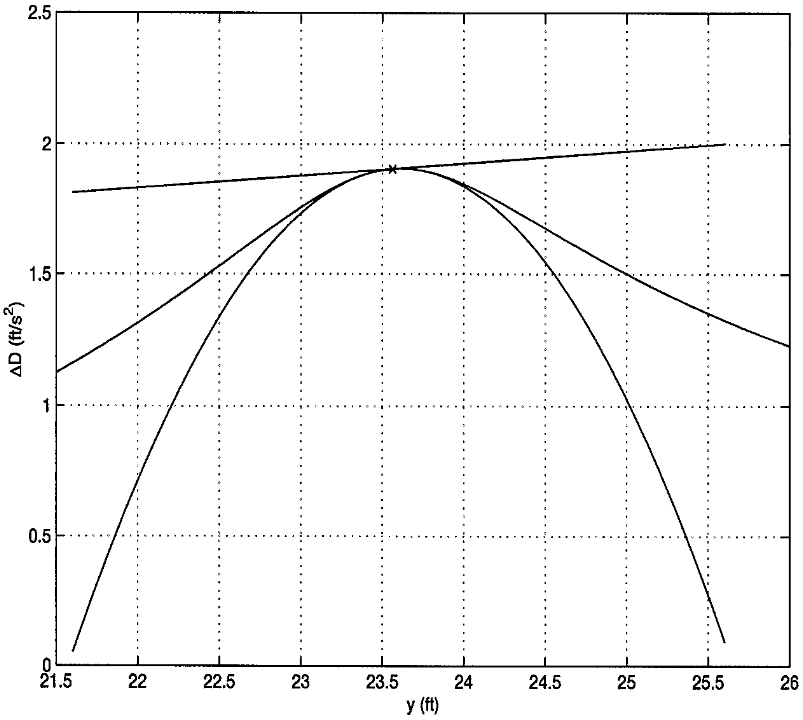

Figure 4.12 Δ D at $\bar{z}$ = 0: 1st Order Approximation-Top Actual-Middle, 2nd Order Approximation-Bottom

The change in side force, ΔY function is also a complicated three dimensional surface. Figure 4.13 shows a z-slice of the ΔY function at $\bar{z} = 0$ and Figure 4.14 shows the change in side force for a change in y position evaluated at $\bar{z} = 0$. From these figures, it is evident that the ΔY curve is also dynamic, but the highly dynamic region is removed from the nominal operating point. Recall, the nominal separation distances were choosen to achieve a maximum reduction in drag not side force. For this reason, the ΔY is less dynamic than the ΔD near the nominal operating point. However, the function is not symmetric for equal positive and negative changes in y location. A reduction in y separation distance of more than $\frac{1}{5}b$ results in a strong increase in negative side force. The side force slowly decays to zero for increasing y separation.

Figure 4.15 shows the same ΔY function, but sliced in the $\hat{y}$ direction at $\bar{y} = \frac{\pi}{4}b$. The partial derivatives for ΔY with respect to a change in z are shown in Figure 4.16. It is again obvious in these figures that the nominal position is removed from the highly dynamic region. A change in z separation will have only minor impact on ΔY. The magnitude changes caused by a change in z are much less severe than those caused by a change in y.

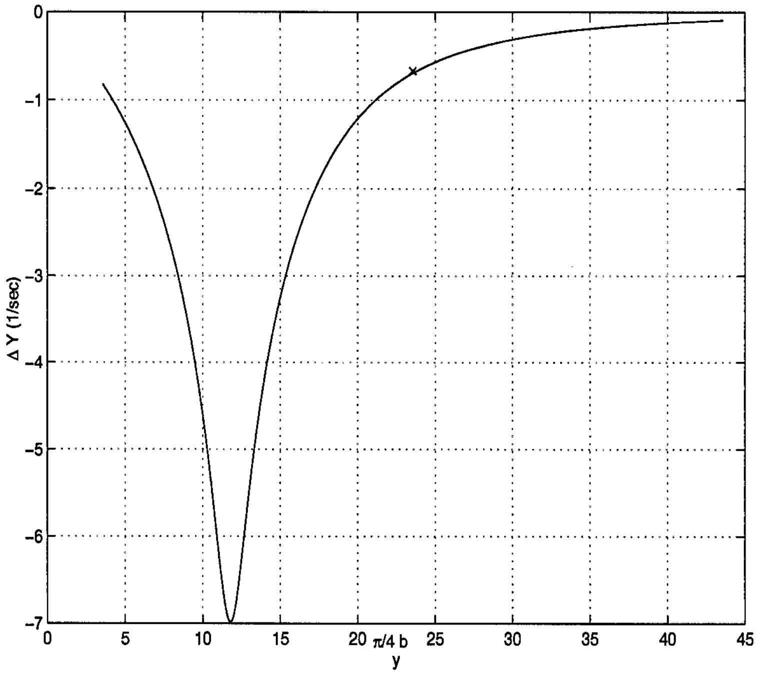

Figure 4.13 Δ Y z-slice at $\bar{z} = 0$

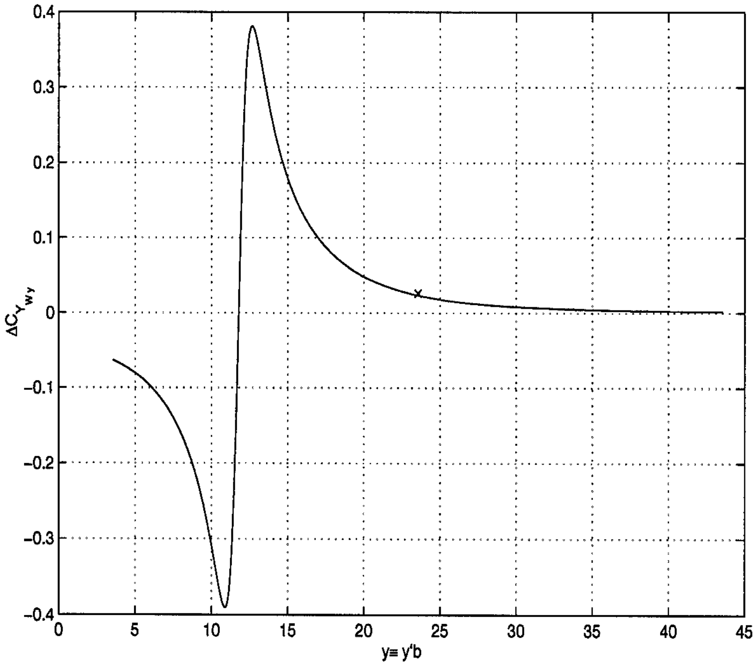

Figure 4.14 Change in Δ Y for a change in y

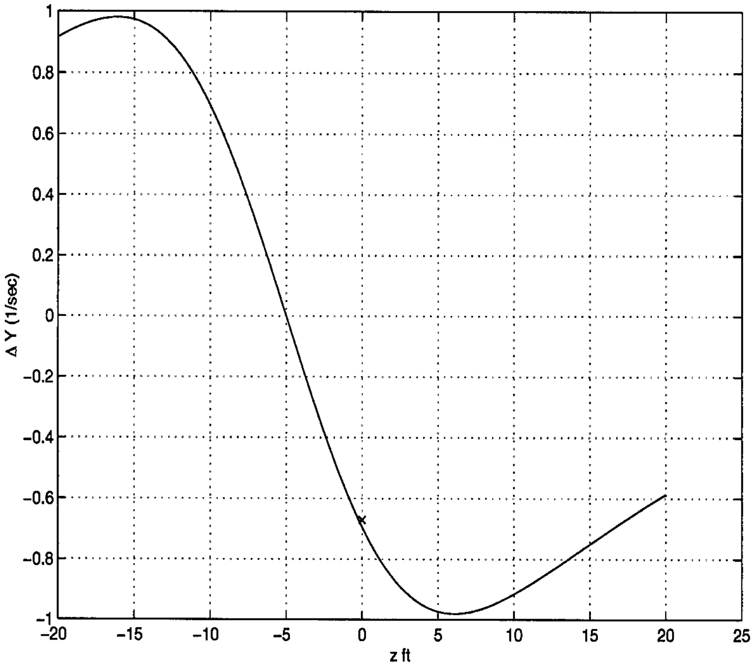

Figure 4.15 Δ Y y-slice at $\bar{y} = \frac{\pi}{4}b$

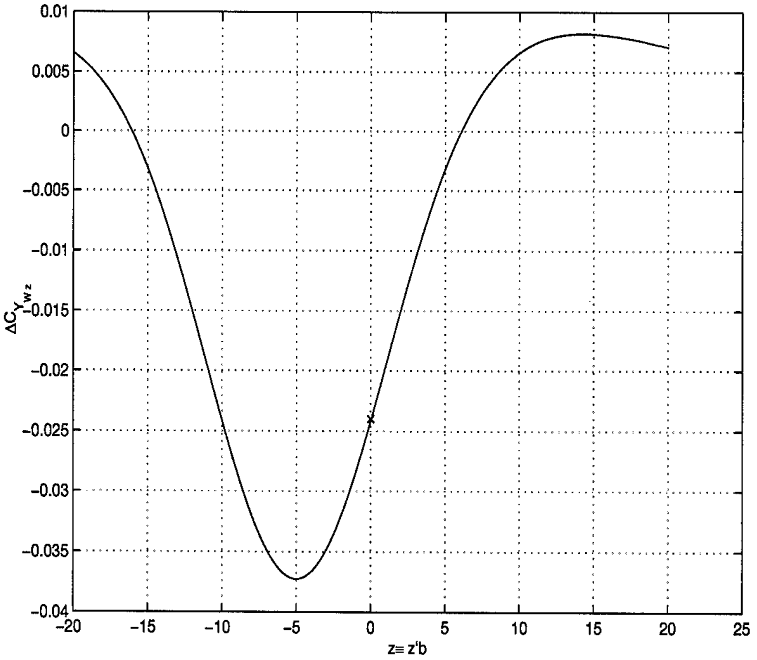

Figure 4.16 Change in Δ Y for a change in z

Overall, it was seen from Figures 4.8 - 4.16 with the exception of Figure 4.12, that the vortex strength changes drastically from location to location and changes very quickly, but the magnitude of the cross coupling due to the vortex is much smaller than the magnitude of the kinematically induced coupling. This is easily seen from the linearized system dynamics A matrix in Equation 4.18. The $A_{1,4}$, $A_{3,4}$, and $A_{4,4}$ terms are the kinematic induced coupled terms. The $A_{1,3}$, $A_{2,3}$, $A_{3,3}$, $A_{4,3}$, $A_{5,3}$, $A_{6,3}$,$A_{1,5}$, $A_{3,5}$, and $A_{4,5}$ terms are the aerodynamic cross coupling caused by the Lead vortex. Except for $A_{6,3}$, all the vortex terms compared to the kinematic cross coupling terms are quite small. Therefore, the kinematic coupling has a stronger influence on the robustness of the controller than does the vortex induced aerodynamic cross coupling. The formation flight controller was previously shown to be robust enough to handle the kinematic coupling [3]. Hence, the FFCS designed by Dargan is quite robust with respect to the minor disturbances caused by the vortex, as well.

4.5 Complete Nonlinear Simulation Model

The full linear system was developed in the beginning of this chapter. This was needed for the design of the close formation flight controller. Once the close FFC is developed using the linear system, it needs to be tested on the actual nonlinear system.

The nonlinear system is developed by replacing the first order close formation stability derivatives in Equations (3.39) - (3.41) with the actual coefficients for ΔC_{D_W}, ΔC_{L_W}, and ΔC_{Y_W} shown in Equations (3.15), (3.18), and (3.21) and adjoining them to the nonlinear kinematics Equations (2.22) - (2.24). The full nonlinear system is:

$$\dot{x} = -\frac{y}{\tau_{\psi_W}}\psi_W - V_W + V_L cos(\psi_L - \psi_W) + \frac{y}{\tau_{\psi_W}}\psi_{W_c} + y\frac{\bar{q}S}{mV_W}\Delta C_{Y_W} \tag{4.32}$$

$$\dot{y} = \frac{x}{\tau_{\psi_W}}\psi_W + V_L sin(\psi_L - \psi_W) - \frac{x}{\tau_{\psi_W}}\psi_{W_c} - x\frac{\bar{q}S}{mV_W}\Delta C_{Y_W} \tag{4.33}$$

$$\dot{V}_W = -\frac{1}{\tau_V}V_W + \frac{1}{\tau_V}V_{W_c} + \frac{\bar{q}S}{m}\Delta C_{D_W} \tag{4.34}$$

$$\dot{\psi}_W = -\frac{1}{\tau_{\psi_W}}\psi_W + \frac{1}{\tau_{\psi_W}}\psi_{W_c} + \frac{\bar{q}S}{mV_W}\Delta C_{Y_W} \tag{4.35}$$

$$\dot{z} = \zeta \tag{4.36}$$

$$\dot{\zeta} = -\left(\frac{1}{\tau_{h_a}}+\frac{1}{\tau_{h_b}}\right)\zeta - \frac{1}{\tau_{h_a}\tau_{h_b}}z + \frac{1}{\tau_{h_a}\tau_{h_b}}H_{W_c} - -\frac{1}{\tau_{h_a}\tau_{h_b}}H_{L_c} + \frac{\bar{q}S}{m}\Delta C_{L_W} \quad (4.37)$$

where the vertical separation $z = h_W - h_L$ and the Wing and Lead aircraft are assumed to have the same vertical dynamics and Equation (4.35) for $\dot{\psi}$ is inserted into the x and y separation differential equations as in the linear version. This full nonlinear model and the nonlinear model with the linear close formation stability derivatives, Equations (4.1) - (4.7) are used in the performance evaluations in Chapter V. The full nonlinear model, Equations (4.32 - 4.37), is shown in Figure 4.17.

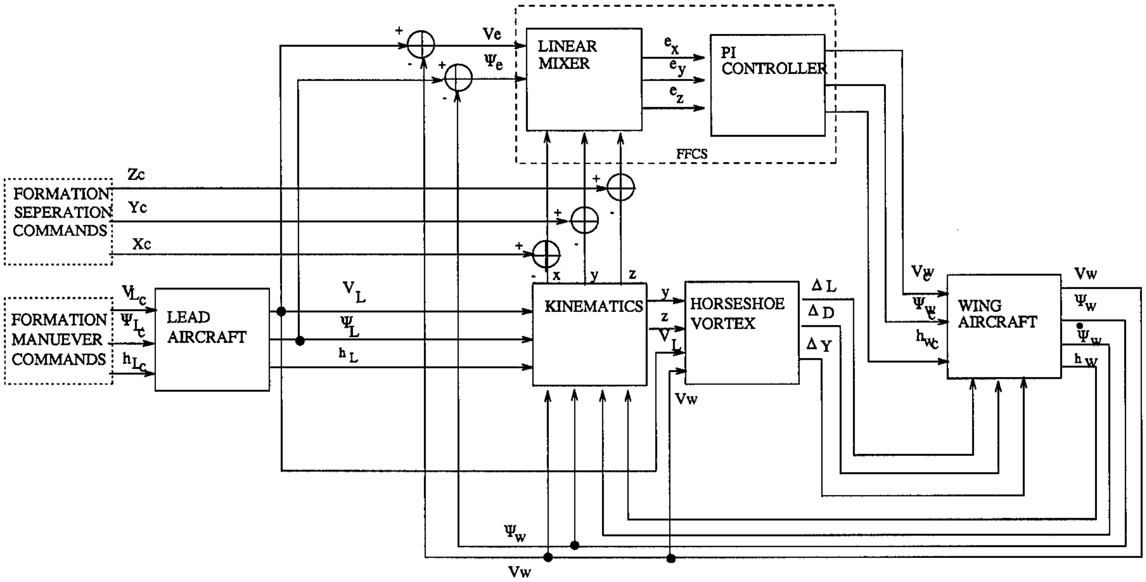

Figure 4.17 Formation Flight Control System Nonlinear Simulation Diagram

4.6 Summary

In this chapter, the complete six state model was developed and the method for gain selection was described. The linear closed loop system was developed and a stability analysis was conducted for the closed loop system. The aerodynamic coupling was evaluated and shown to be weak in comparison to the coupling created by the kinematics, thereby justifying the use the large formation flight controller. Finally, the large formation flight controller was shown to be robust enough to handle the aerodynamic coupling created by the vortex.

V. Performance Evaluation

This chapter describes the complete nonlinear simulation model, including a description of the command prefilter. A description of the format for the response plots is provided. Performance evaluations for six cases are performed: The cases evaluated are +/- heading changes, +/- velocity changes, and +/- altitude changes. Each case is subdivided into three runs. The system response for each case is discussed and comparisons are made between cases.

The simulation model is shown in Figure 4.17. The Lead and Wing Aircraft blocks are represented by the linear F-16 class aircraft FCS developed in Chapter II. The FFCS block is represented by the model developed in Chapter IV. The kinematics block is modeled using the fully non-linear Equations (2.22) - (2.24) outlined in Chapter II. The Horseshoe Vortex block is actually composed of two models described in Chapter III. One is the linear model developed in Equations (3.35) - (3.38). The other is the fully non-linear version developed in Equations (3.15), (3.18), and (3.21). The coupling terms are appropriately dimensionalized and then added as disturbances to the Wing flight control system. Both the linear cross coupling version and the non-linear vortex version are used in the following simulations. A command prefilter is contained in the Formation Maneuver Command block. It processes the input step commands so they follow more closely the commands input into an actual aircraft autopilot. This basically ramps the commands into the aircraft FCS instead of inputting an instantaneous step change. This allows the errors to grow gradually instead of instantly changing from zero error to 100 percent error and prevents the immediate saturation of the aircraft flight control system. Saturation of the FCS for long periods can result in instability. The complete Matlab Simulink simulation model is shown in Appendix A.

The Lead and Wing aircraft are flying in a close diamond formation with $\bar{x} = 60ft$ and $\bar{y} = 23.562ft$ or 2b and $\frac{\pi}{4}b$, respectively and $\bar{z} = 0$. This formation was shown previously in Figure 1.2 in which the Lead is on the right side and in front of the Wing. Typical F-16 class aircraft characteristics are listed in Table 4.1 and the evaluated formation stability derivatives are listed in Table 4.2.

5.1 Case Definition

Each case consists of three runs: no cross coupling, linear cross coupling, and nonlinear cross coupling. There are cases for both positive and negative change of equal magnitude. Comparison of the positive and negative cases show the difference between maneuvers in which the Lead is moving away from the Wing and when the Lead is moving toward the Wing. The positive and negative heading plots can also be used to determine the response in the event there are two Wingmen; one on each side of the Lead.

Long distance flying usually entails flying from waypoint to waypoint until the final destination is reached. Usually waypoints are defined by radio beacons or airports. Beginning at the initial airport of takeoff, the pilot dials in the autopilots' velocity, heading, and altitude to reach the next way point. Upon reaching the next waypoint, the pilot enters the new velocity, heading, and altitude values into the autopilot to proceed to the next waypoint and so on until the final destination is reached. Usually, the paths followed are relatively strait. This means that large heading changes between waypoints will not be encountered. The simulation cases were chosen based on this scenario and should be representative of typical autopilot changes implemented by a pilot as he sets the autopilot to proceed to the next waypoint.

The format for the time response plots and the Lissajous plots is the same as described in Chapter IV and is repeated below. The time plots contain six subplots. In the top three subplots, the solid line represents the Lead aircraft and the dashed line represents the Wing aircraft. In some cases only a solid line is visible, this is due to the overlap of the responses from the Lead and the Wing. In the bottom three subplots, the solid line represents the nominal separation values and the dashed line represents the actual values. Starting points in the Lissajous plots are represented by an 'O' and the ending points are represented by an 'X'. This format is used for each plot listed in the following sections.

5.2 Negative 30 Degree Heading Change

The formation is commanded a heading change of negative 30° in which the Lead aircraft turns into the Wing aircraft. Figures 5.1 and 5.2 show the time and Lissajous response plots for the linearized system without cross coupling. Even with the prefilter in place there is a slight saturation of the Lead heading response. This is not significant and more importantly the Lead is considered a disturbance so it truly doesn't matter whether it is saturated or not for this analysis. The Wing does not experience any saturation in heading response.

The Wing heading follows the Lead heading so closely that the two overlap. However, the Wing's velocity varies to follow the heading change of the Lead. The Wing must decrease it's velocity, since the Lead is turning into it. This causes the separation in the $\hat{x}$ direction to initially decrease as expected. The y separation initially increases and then undershoots the nominal and slowly increases and levels off at the nominal y separation. The formation separation reduces to a minimum 56 ft in the $\hat{x}$ direction or 4 ft from nominal. The closest the Lead comes to the Wing in the $\hat{y}$ direction is 20.6 ft or 3 ft from nominal. In fact the maximum positive and negative deviations in the $\hat{y}$ direction are 3 ft, meeting the first gain criterion. The x-channel settles within 12 seconds and the y-channel settles within 60 seconds. The formation spacing is maintained within approximately 3 ft (1/10 b) in both the $\hat{x}$ and $\hat{y}$ directions and zero steady state tracking errors are achieved after the heading change is complete. The z separation stays at zero for the duration of the maneuver.

Figures 5.3 and 5.4 are the response plots for -30° heading change with linear cross coupling. The most obvious and most interesting difference between this run and the previous run without cross coupling is the affect of the cross coupling on the z-channel. Specifically, the cross coupling of the y separation into the altitude hold autopilot through the $A_{6,3}$ term. The linear cross coupling causes an oscillation in the vertical channel. It is a very small oscillation with a maximum deviation of 3×10^{-3} ft and a minimum deviation of 5×10^{-3} ft and is nulled out by the PI controller. The initial increase in y separation causes an increase in the Wing's lift causing it to ascend above the Lead. It is apparent from this response that the change in z separation follows the linear first order ΔL function exactly. The ΔL first order model decreases for decreasing y separation and increases for increasing y separation.

Figures 5.5 and 5.6 are the response plots for -30° heading change with non-linear cross coupling. The effect of the non-linear cross coupling is very different than that of the linear coupling. The vertical channel perturbations are less graceful and greater in magnitude than that of the run with linear coupling. The x and y separation plots are also different than the previous two runs.

The minimum x separation increases from -4 ft to -3.85 ft. The maximum x deviation increases from 0 ft to 0.1 ft. Basically the entire x response plot just shifted up by 0.1 ft. This is due to the change in drag from the change in y separation. The linearized ΔD function, Figure 4.12 did not accurately represent the true change in drag for changes in y separations greater than 0.25 ft in magnitude from the nominal y separation.

The y separation also changed. The positive and negative deviations for the previous two runs were 3 ft and -3 ft, respectively. In this run, the positive and negative deviations are 2.3 ft and -2.2 ft, respectively. This is a change of 0.7 ft and 0.8 ft, respectively from the previous runs. The error improved in both the positive and negative directions by about the same amount. Recall from Figure 4.13, the nominal point rests in the middle of the knee of the curve where the slope is changing slowly. In fact, the change in side force magnitude is almost equal for changes in y of +/-3 ft. The increase in y separation causes the sideforce to decrease causing the Wing to turn away from the Lead. Since, the Lead is turning into the Wing this speeds up the Wing's heading response leading to a reduced error in the y separation. The smaller error means the controller does not have to apply as much correction as in the previous two runs resulting in a smaller undershoot as the controller pulls the y separation toward nominal.

The z separation decreases initially as y increases. As the controller decreases the y separation towards the nominal y, the z separation begins to increase. When the y separation crosses the nominal, the z separation briefly crosses the $\hat{z}$ axis becoming slightly positive and then quickly decreases again as y continues to decrease. The y separation then slowly increases and levels off when it reaches the nominal y value. The z separation slowly increases overshoots and then starts to decrease and level off at the nominal z separation.

There are four primary pieces to the z plot. The first piece is the first negative peak. Since the Wing is sitting at the point of maximum lift in the vortex, any deviation causes a decrease in ΔL. This is reversed from the linear coupling run in which the initial increase in y separation caused an increase in z separation or an increase in ΔL. The crossing of the z axis is interesting. The response in this area demonstrates how quickly the magnitude of the ΔL changes for relatively small changes in separation between aircraft. Since the changes in z separation are so small, the ΔD, ΔL, and ΔF_Y forces are dependent on the change in y separation only.

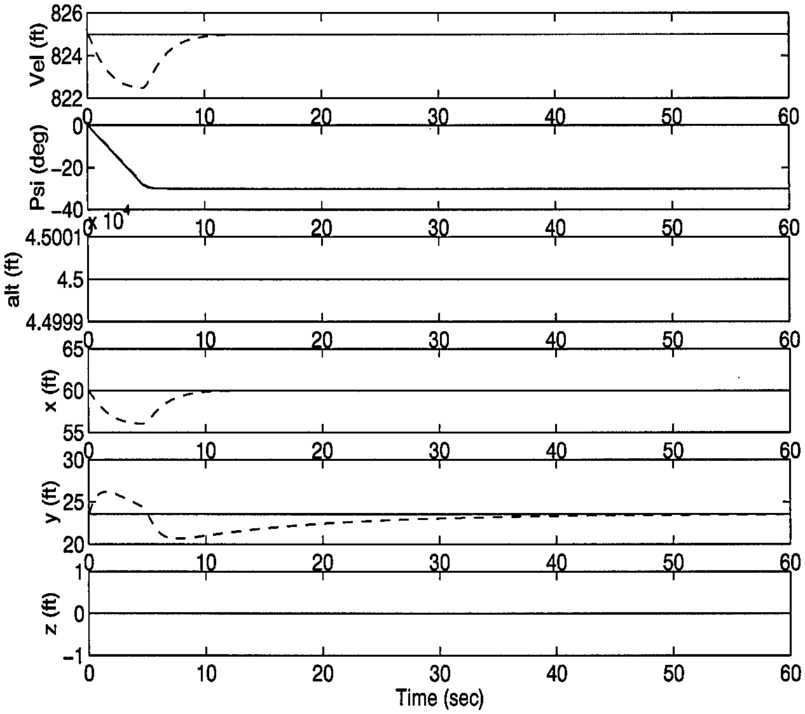

Figure 5.1 -30 Degree Heading Change Without Coupling Time Plot

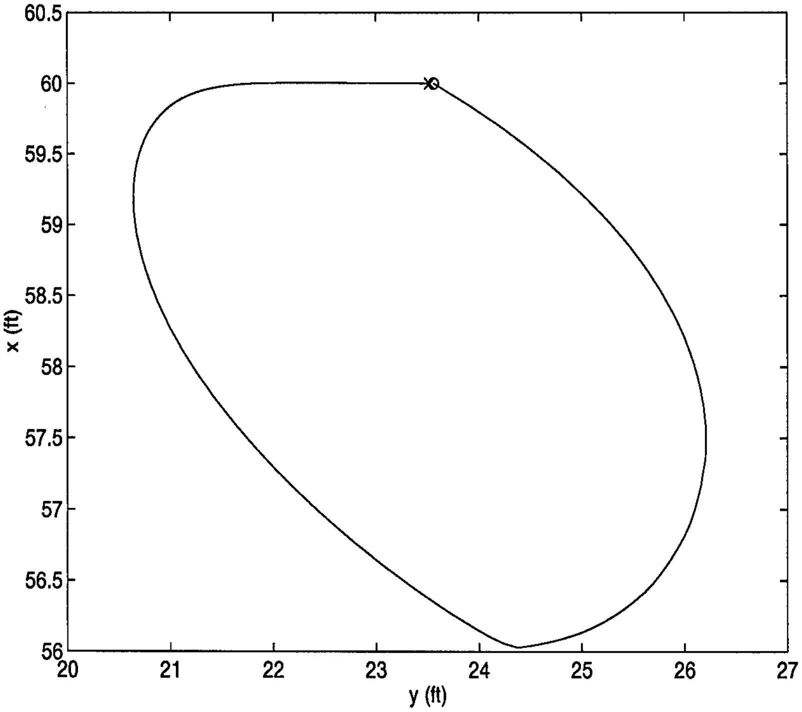

Figure 5.2 -30 Degree Heading Change Without Coupling Lissajous Plot

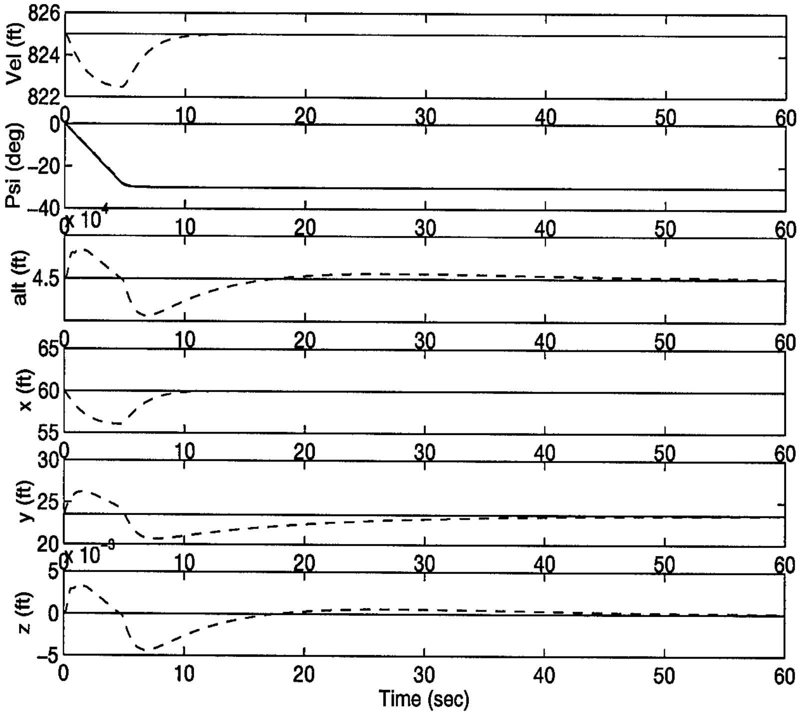

Figure 5.3 -30 Degree Heading Change With Linear Coupling Time Plot

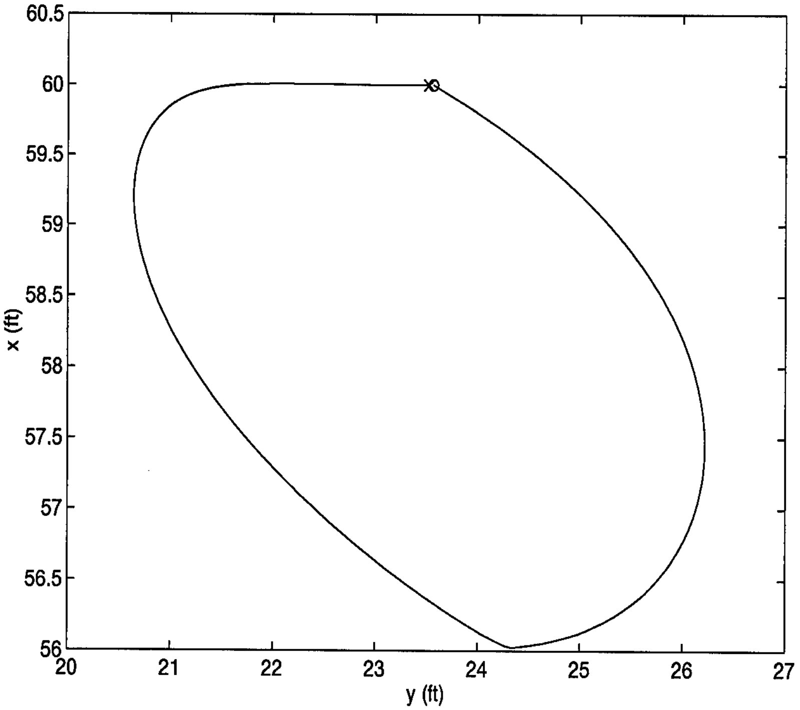

Figure 5.4 -30 Degree Heading Change With Linear Coupling Lissajous Plot

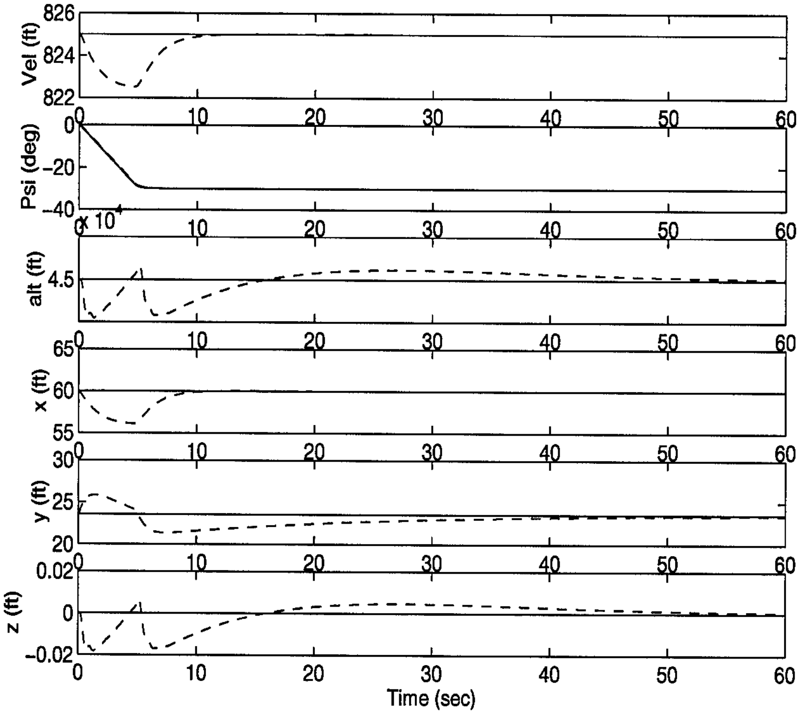

Figure 5.5 -30 Degree Heading Change With Non-Linear Coupling Time Plot

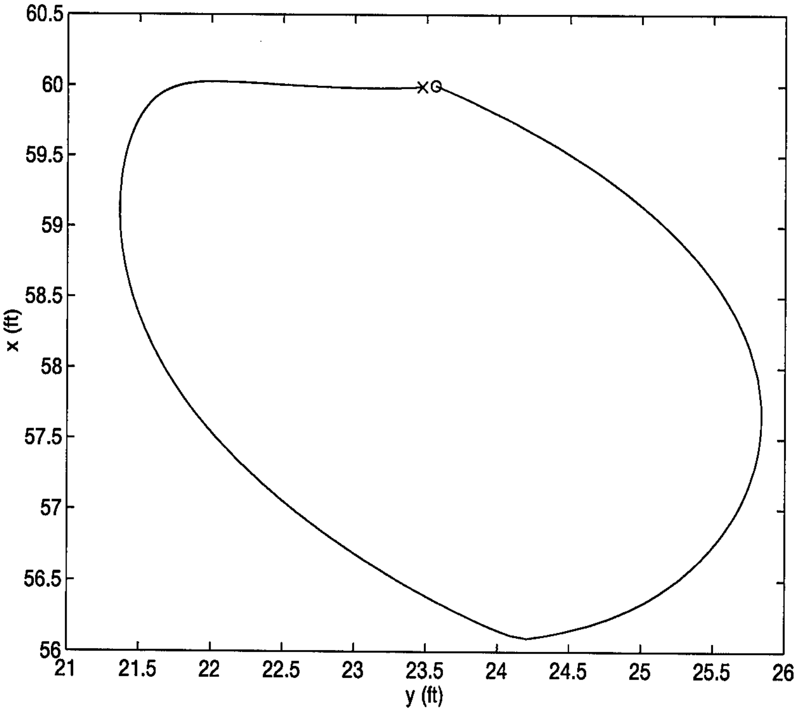

Figure 5.6 -30 Degree Heading Change With Non-Linear Coupling Lissajous Plot

5.3 Positive 30 Degree Heading Change

The positive 30° heading change without coupling is shown in Figures 5.7 - 5.8. This again causes a slight saturation in the Lead heading response. The two headings overlap, however the velocity increases instead of decreasing as in the previous case. In this case, the Lead is turning away from the Wing causing the Wing to play catch up. Since the Wing is on the outside it needs to cover a longer distance than the Lead in order to maintain the formation. This causes the Wing to briefly increase it's velocity. The response in the x and y plots is exactly the opposite of the $-30°$ heading change maneuver. Instead of decreasing as in the $-30°$ case, the x separation initially increases. The y separation initially decreases, then overshoots and slowly decays to nominal. The maximum separation in the $\hat{x}$ direction is 63.3 ft or $+3.3$ ft from nominal. It can be seen from the plots, that the closest the two aircraft come to one another in the $\hat{y}$ direction is 20.6 ft and the farthest is 26.5 ft, i.e., approximately -3 ft and $+3$ ft from nominal, respectively. As expected, there is no change in the vertical channel.

The positive 30° heading change with linear coupling is shown in Figures 5.9 - 5.10. The primary difference between the plots with linear cross coupling versus those without cross coupling is again the effect on the vertical channel. The cross coupling causes an initial oscillation in the vertical channel that is almost exactly the opposite of the previous case, $-30°$ heading change with linear coupling. The PI controller nulls the perturbation out after about 60 sec. The perturbation in the z-channel is again caused by the linking term $A_{6,3}$ and responds exactly as expected from the ΔL first order model.

The non-linear coupling plots are shown in Figures 5.11 - 5.12. The x separation error is 0.1 ft larger than in the previous two runs; 3.4 ft versus 3.3 ft. As in the -30° case with non-linear coupling, the first order model does not accurately represent the changes in magnitude of drag for changes in y greater than +/-0.25 ft.

In the case of the negative and positive 30° heading changes with linear cross coupling, the results were identical except flipped in the $\hat{z}$ direction. This is not true for the non-linear cases. The z separation responses for both a positive and negative 30° heading change are remarkably similar. The initial decrease in y causes a decrease in z. As y begins to increase the z separation begins to increase. The z separation briefly crosses its nominal as y crosses its nominal and then starts to decrease again as y continues to increase. The y separation then decreases slowly back to nominal. The z separation also increases back to nominal, but overshoots slightly. The first $\hat{z}$ crossover is caused by both the controller attempting to null out the error and the increasing ΔL caused by the shrinking error in the y separation between the Wing and the Lead aircraft. The reason this response is almost identical to that of the negative heading change is because the ΔL function is nearly symmetric with respect to the nominal $\bar{y} = 23.562$ ft for y separations in the range of 20.5 ft - 26.5 ft or -/+ 3 ft as previously described and seen in Figure 4.8. The magnitude of the negative deviation is slightly larger (0.06 ft) than in the -30° run with nonlinear coupling due to the slight non-symmetry in ΔL. As in the negative heading change cases, the ΔD, ΔL, and ΔF_Y depend on changes in y separation only.

Recall from Chapter IV, the second requirement for gain selection was to achieve consistent results for both positive and negative maneuvers of equal magnitude. This is best seen by comparing the Lissajous plots, Figures 5.2 and 5.8 for the $-30°$ and $+30°$ runs. The positive heading change Lissajous plot is almost identical as the the negative heading change Lissajous plot except it is rotated by 180 degrees. This is also true for Figures 5.4 and 5.10 and and Figures 5.6 and 5.12

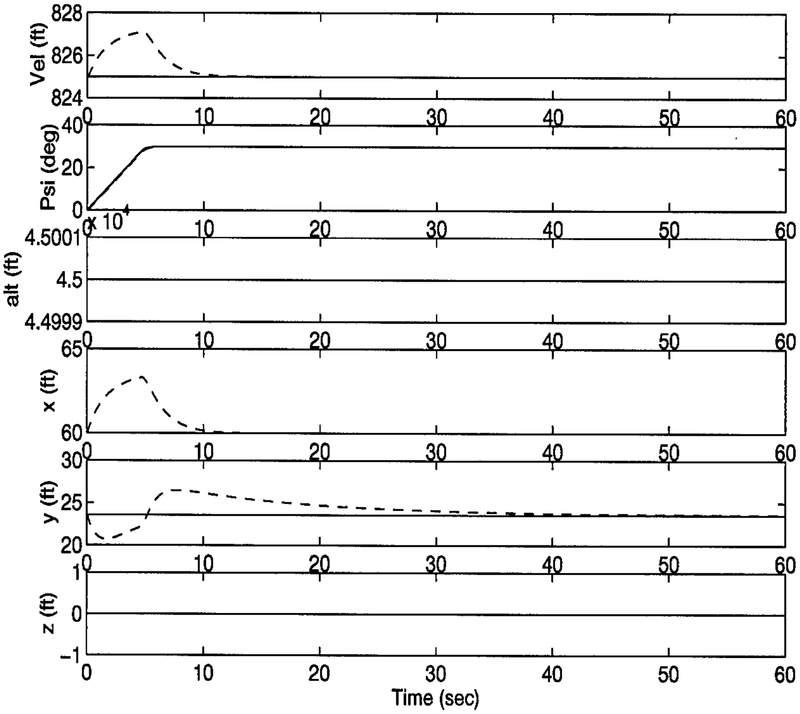

Figure 5.7 30 Degree Heading Change Without Coupling Time Plot

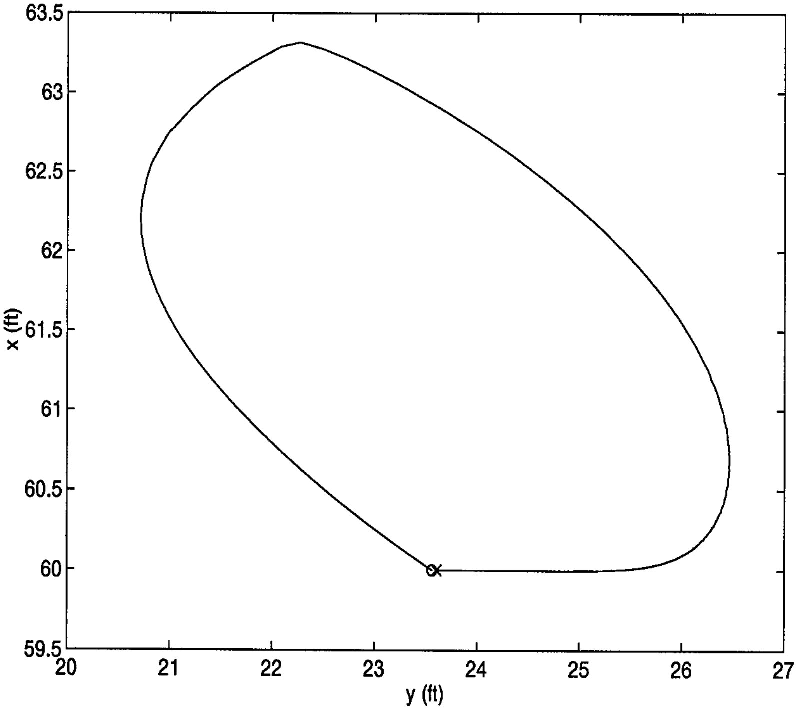

Figure 5.8 30 Degree Heading Change Without Coupling Lissajous Plot

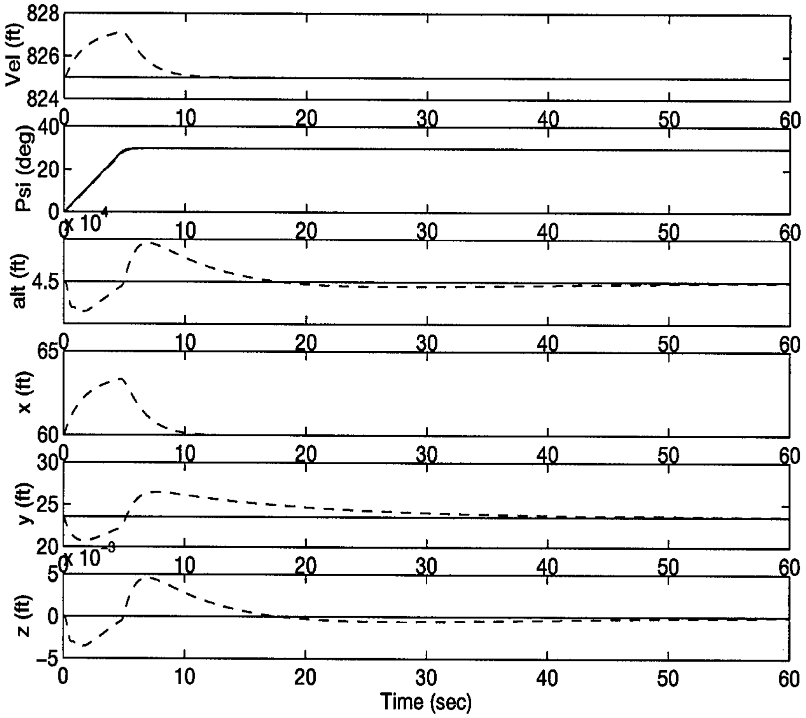

Figure 5.9 30 Degree Heading Change With Linear Coupling Time Plot

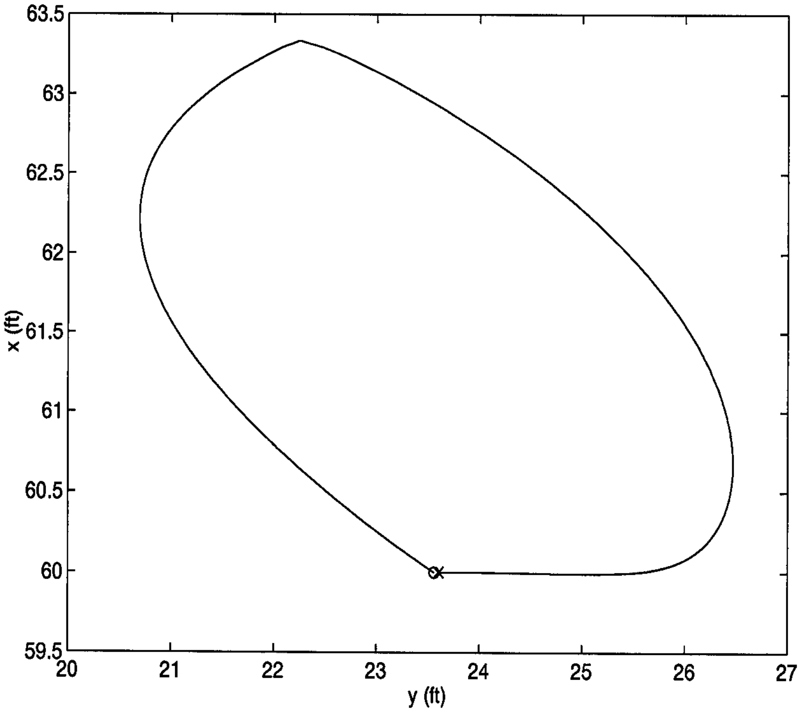

Figure 5.10 30 Degree Heading Change With Linear Coupling Lissajous Plot

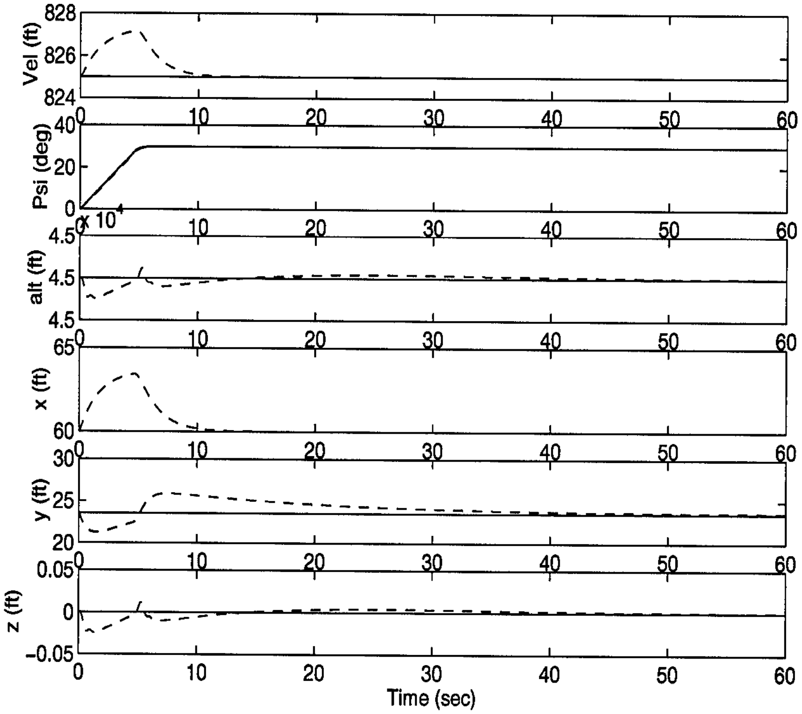

Figure 5.11 30 Degree Heading Change With Non-Linear Coupling Time Plot

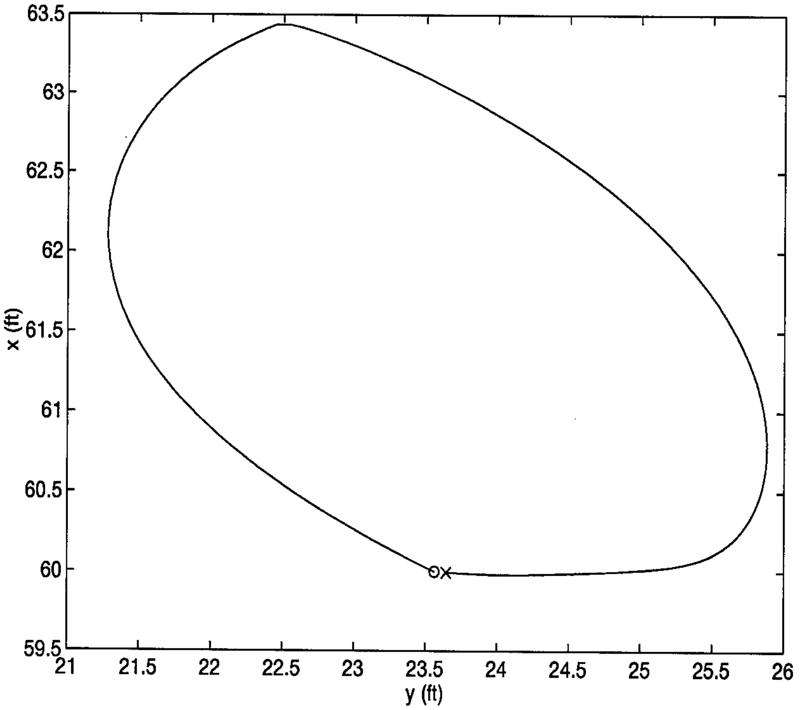

Figure 5.12 30 Degree Heading Change With Non-Linear Coupling Lissajous Plot

5.4 50 ft/sec Velocity Decrease

In this case, the formation is commanded a decrease in velocity of 50 ft/sec without cross coupling as seen in 5.13 - 5.14. The velocity of the Wing follows the Lead so closely that the two cannot be distinguished on the velocity time plot. However, the x separation distance immediately decreases. This shows that there is some delay between the time the Lead starts to decrease it's velocity and the time the Wing starts to decrease it's velocity. This is expected since the Wing does not have foreknowledge of the Lead's future maneuvers. The FFCS is very tight and allows a maximum error of approximately 0.8 ft and settles in about 60 seconds. The y and z channels are unaffected by the velocity change.

There is no difference between the run with cross coupling and the run with no cross coupling. As seen in Figures 5.15 - 5.16, the response in the x separation is the same as the previous run without cross coupling. The first order model was developed based on the assumption that the vortex extends a long distance behind the Lead. Secondly, the linearized kinematic equation for y separation is only affected by heading changes, not velocity changes. Therefore, a change in $\hat{x}$ direction does not affect the upwash or sidewash. Only a change in the $\hat{y}$ direction can cause a change in upwash and sidewash. Therefore, the reduction in drag ΔD is constant for pure velocity changes. Prior to the Lead velocity change in this run and the previous run the Wing aircraft was in steady-state, i.e., all the forces in the $\hat{x}$ direction sum to zero, leading to a constant velocity. Therefore, the error caused by the decrease in the Lead's velocity and input into the x-channel of the FFC is of equal magnitude and sign and causes identical responses in both runs.

The responses to a 50 ft/sec decrease in velocity with non-linear cross coupling can be seen in Figures 5.17 - 5.18. This is another very interesting run. The x response is the same as in the previous two runs. However, the heading, altitude, y separation, and z separation responses are not zero as in the previous two runs. Both the Wing's heading and y separation plots experience an initial oscillation. The vertical channel experiences a slight decrease in ΔL and causes a drop in altitude of 2×10^{-5} ft. The inital decrease in y separation causes a slight decrease in ΔL that leads to an initial decrease in z separation and then a slow return to nominal. Equations (3.15), (3.18), and (3.21) are necessary to understand the responses from this run. The linear model assumes that the formation's velocity is constant at 825 ft/sec. This is not significant for the heading change maneuvers, since the Lead and Wing velocities vary only slightly. However, this is not the case for a velocity change of 50 ft/sec. There are two reasons for this outcome. First, the Lead velocity determines the strength of the vortex. Secondly, the Wing's velocity determines the change in angle of attack, α, due to the upwash. Both of these directly affect the strength of the upwash and downwash exerted on the Wing aircraft. The ΔL function is proportional to the Lead's velocity and inversly proportional to the Wing's velocity, as seen in Equation (3.18). The formation hold controller responds very quickly keeping the velocity of the Wing almost equal to the velocity of the Lead. Since the two velocities are almost equal, the change in angle of attack, $\Delta\alpha$, is almost constant. It decreases the most at the beginning of the maneuver when the error between the Lead and Wing velocities is the greatest. This is seen in the initial decrease in z separation. ΔF_Y is affected in exactly the same way as ΔD and ΔL. This leads to the tear drop shape shown in Figure 5.18. Even though this response looks very dynamic, closer inspection reveals the magnitudes of the y deviations are very small and the x separation is essentially unchanged from the previous two runs.

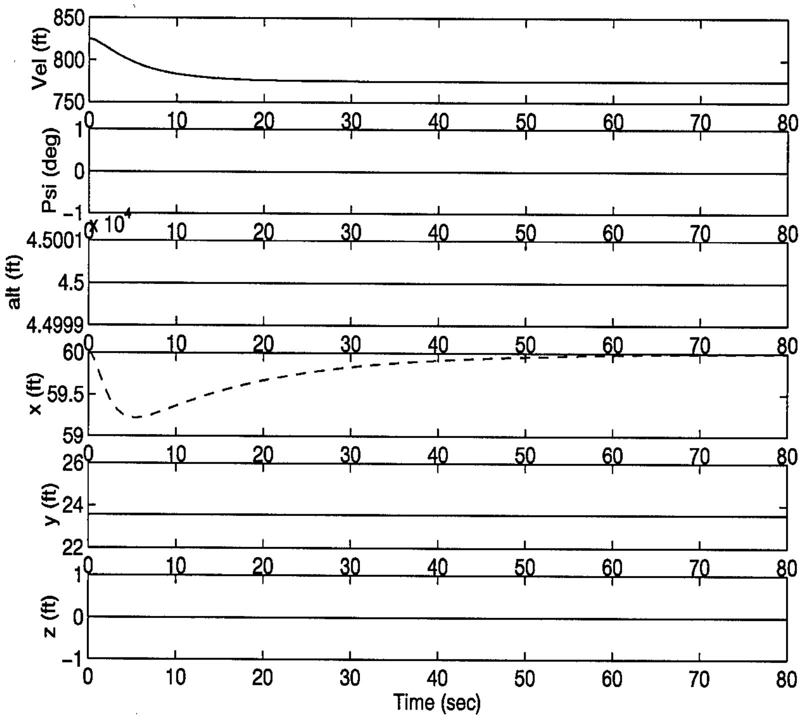

Figure 5.13 50 ft/sec Velocity Decrease Without Coupling Time Plot

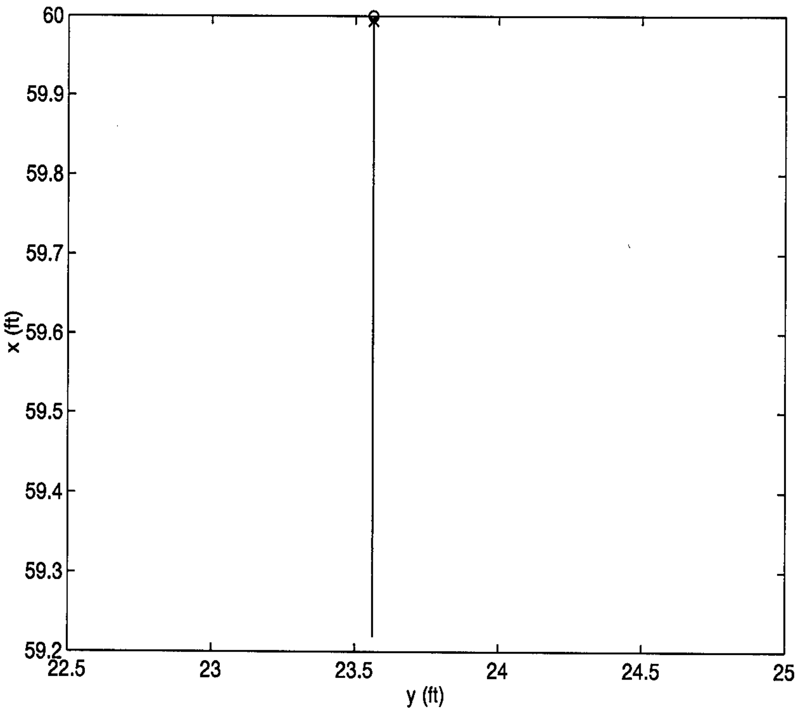

Figure 5.14 50 ft/sec Velocity Decrease Without Coupling Lissajous Plot

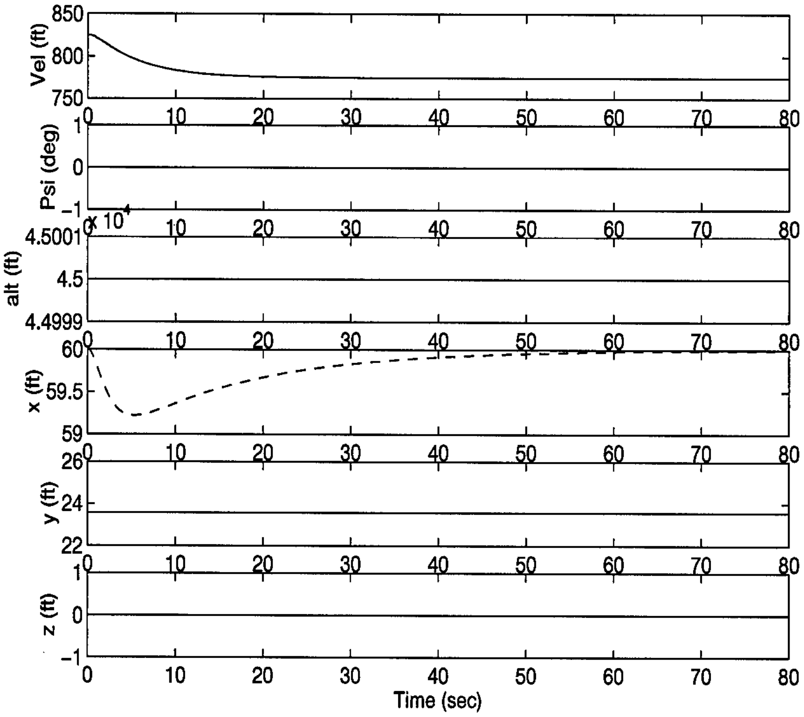

Figure 5.15 50 ft/sec Velocity Decrease With Linear Coupling Time Plot

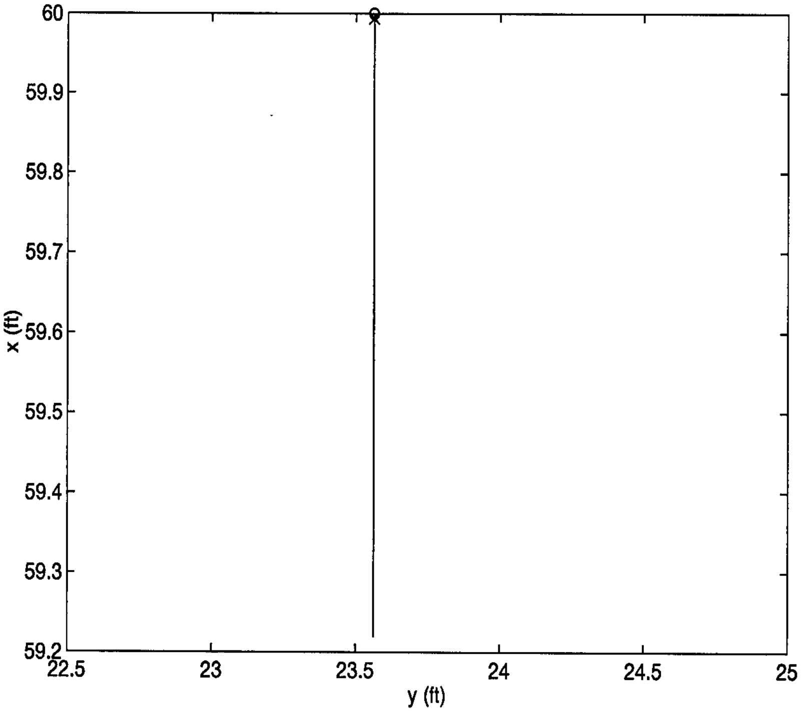

Figure 5.16 50 ft/sec Velocity Decrease With Linear Coupling Lissajous Plot

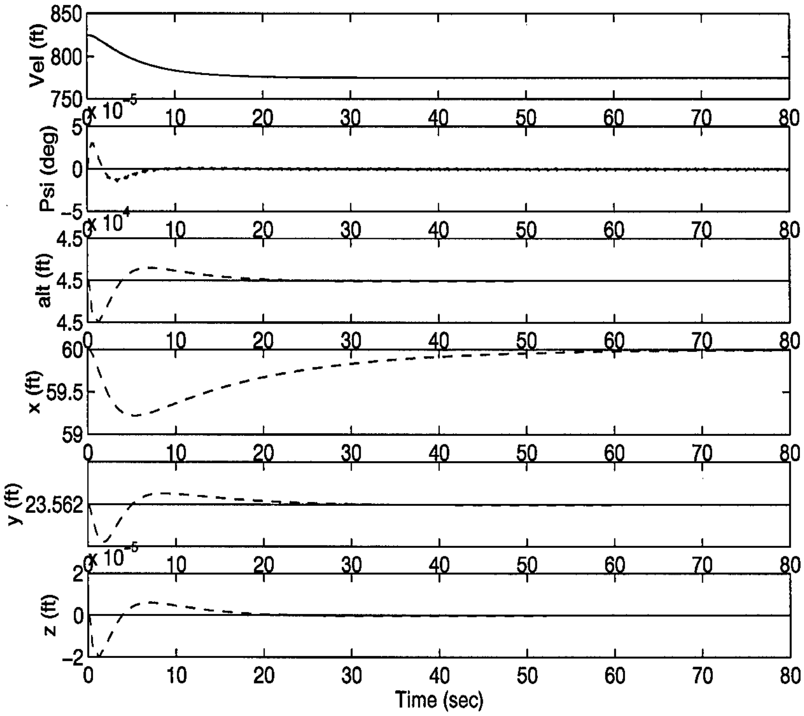

Figure 5.17 50 ft/sec Velocity Decrease With Non-Linear Coupling Time Plot

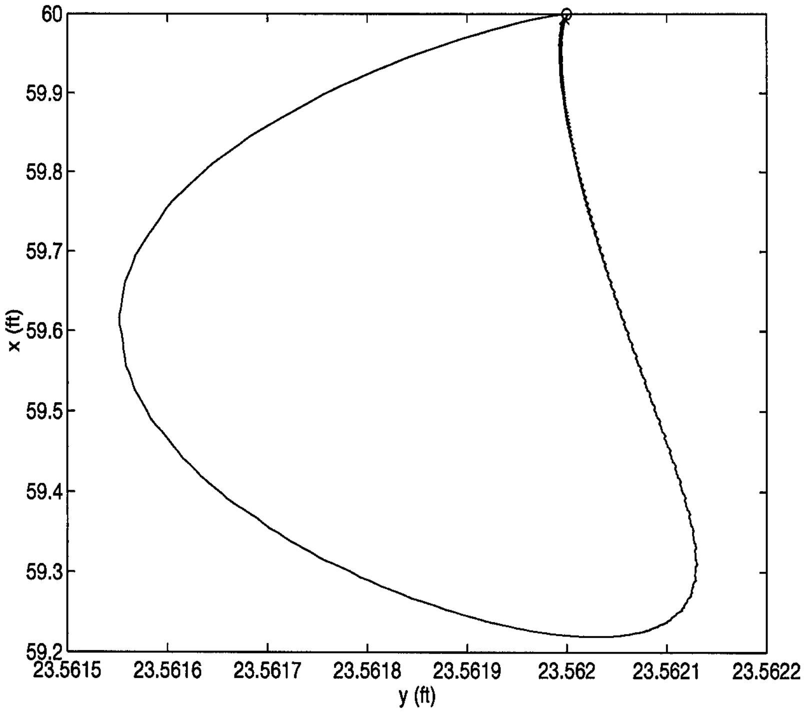

Figure 5.18 50 ft/sec Velocity Decrease With Non-Linear Coupling Lissajous Plot

5.5 50 ft/sec Velocity Increase

The formation is commanded an increase in velocity of 50 ft/sec without cross coupling. This case is the exact opposite of the previous case run, 50 ft/sec decrease in velocity with no coupling. The velocity of the Wing again follows the Lead so closely that the two cannot be distinguished on the time plot, Figure 5.19, but the x separation distance immediately increases as seen in the Lissajous plot, Figure 5.20. As in the previous case, there is some delay between the time the Lead starts to increase velocity and the time the Wing starts to increase velocity. The FFCS allows a maximum error of 1.4 ft, 0.6 ft greater than the previous case and settles in about 60 seconds, Figures 5.19 and 5.20. The difference in magnitudes between cases is caused by the rate limits for the Mach hold autopilot. The upper limit is half of the lower limit. Therefore, the aircraft can decelerate faster than they can accelerate. The point at which the Wing's Mach hold autopilot saturates is easily identified by the constant slope of the x separation plot for the first 6 seconds. Except for the affects of the non-symmetric saturation limits, the second gain criterion is again satisfied for this case and the case of 50 ft/sec velocity decrease.

Figures 5.21 - 5.22 show the aircraft response to linear cross coupling. This is identical to the previous run without coupling. Recall from the previous case for a velocity decrease of 50 ft/sec; the linear first order model for lift, drag, and sideforce is not affected by changes in x separation and velocity.

The responses for an increase in velocity of 50 ft/sec with non-linear cross coupling is shown in Figures 5.23 - 5.24. As in the case with non-linear cross coupling for the velocity decrease of 50 ft/sec case, all channels are affected by the velocity change. The y separation experiences an initial small oscillation. The x separation error is the same as the two 50 ft/sec velocity increase runs without coupling and with linear coupling. The vertical channel experiences an initial increase in lift caused by the initial increase in $\Delta\alpha$ caused by the Lead's velocity increasing faster than the Wing's velocity. Rotating this Lissajous plot and comparing with the Lissajous Plot from the -50 ft/sec run, Figure 5.18 reveals the responses are very similar except in this run, the y deviation is shifted left of the nominal. This results in the nonsymmetrical bulge in the inverted tear drop.

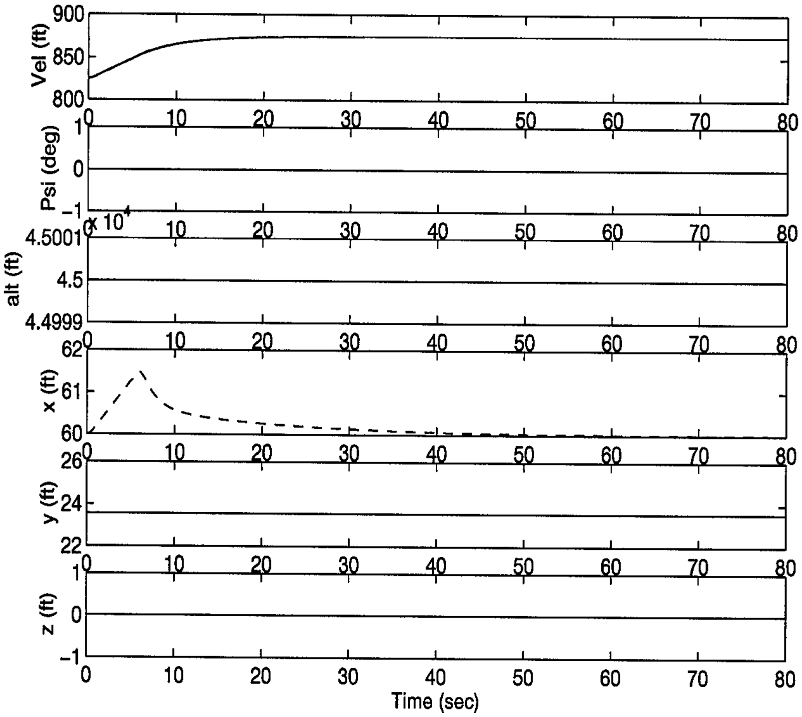

Figure 5.19 50 ft/sec Velocity Increase Without Coupling Time Plot

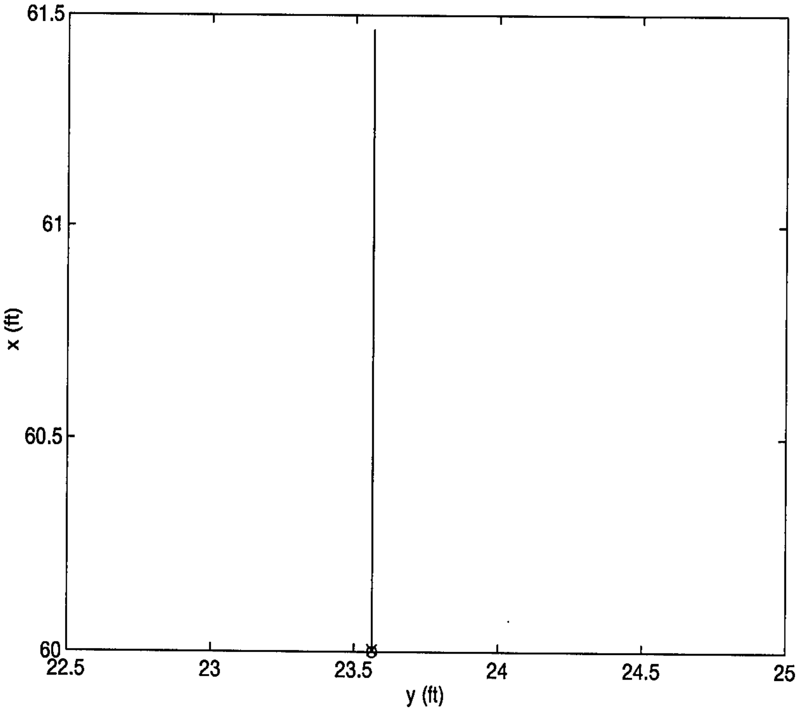

Figure 5.20 50 ft/sec Velocity Increase Without Coupling Lissajous Plot

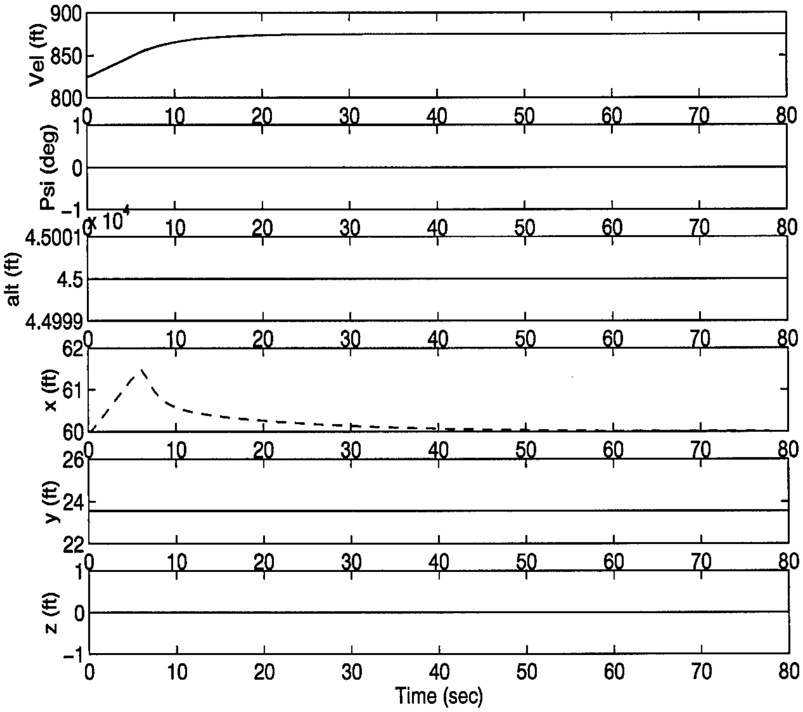

Figure 5.21 50 ft/sec Velocity Increase With Linear Coupling Time Plot

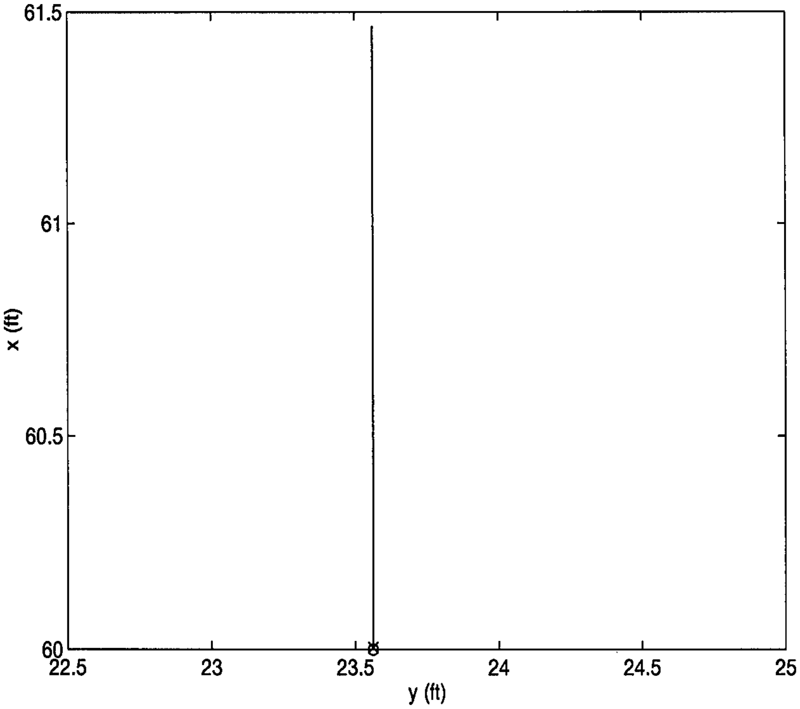

Figure 5.22 50 ft/sec Velocity Increase With Linear Coupling Lissajous Plot

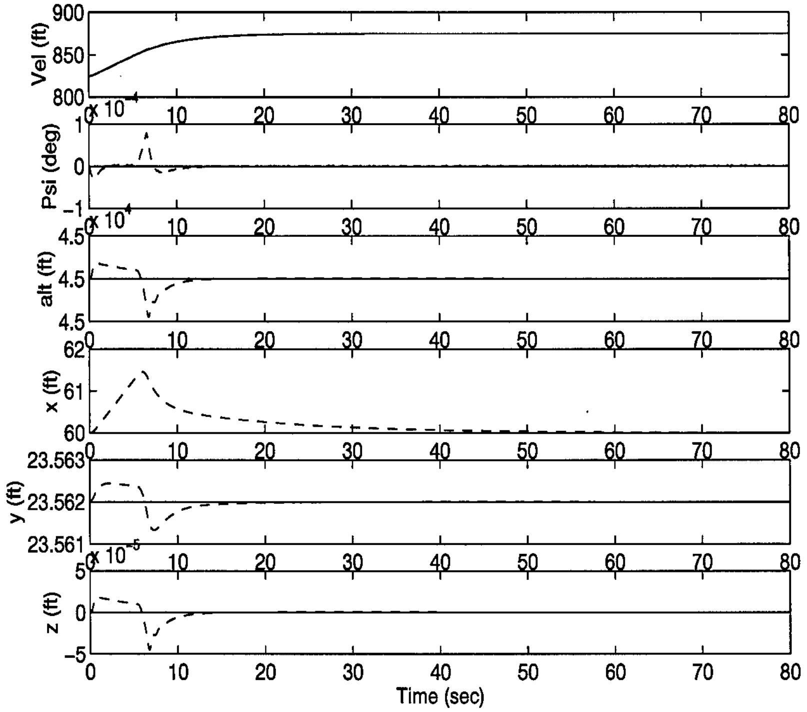

Figure 5.23 50 ft/sec Velocity Increase With Non-Linear Coupling Time Plot

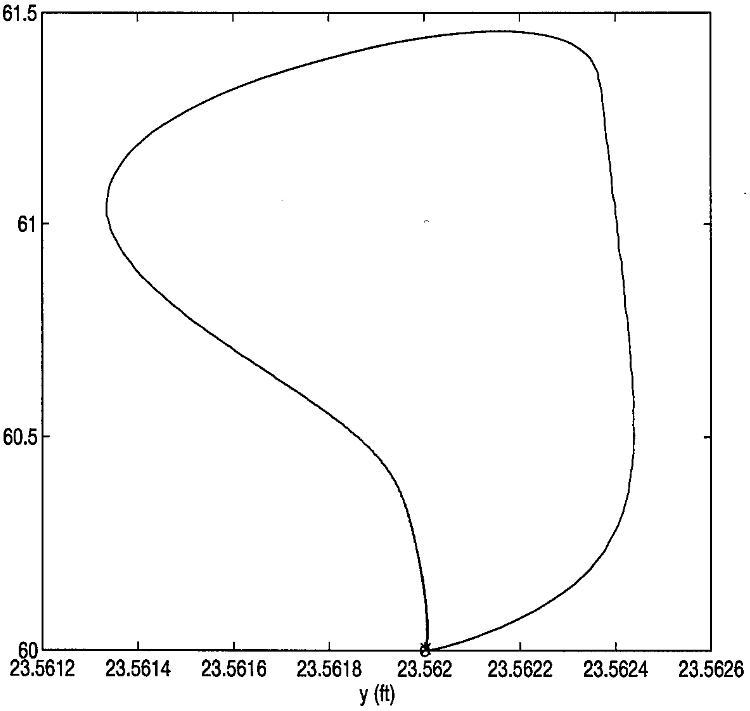

Figure 5.24 50 ft/sec Velocity Increase With Non-Linear Coupling Lissajous Plot

5.6 1000 ft Altitude Decrease

In this case, the formation is commanded a 1000 ft decrease in altitude. Figures 5.25 - 5.26 show the response without cross coupling. The altitude channel is completely separate from the horizontal channels when cross coupling is not included. The Wing tracks fairly closely, but does deviate slightly from the Lead. This can be seen in the z time plot, which shows the vertical separation grow very quickly, level off for a few seconds and then begin to decrease. This maneuver saturates both the Lead and Wing altitude autopilots. The PI controller experiences *windup* during this period of saturation. This can be seen from the level area between 1 and 5 seconds in the z separation plot. Integrator windup causes the feedback to be much larger than the command leading to a large error fed into the controller even though the actual response may be close to the commanded response. In this case, the windup only causes a delay, but in extreme circumstances windup can cause the aircraft to become unstable. Prefilters are used to prevent this from occurring in most cases. They slowly ramp the command into the system, allowing the error to grow gradually and give the controller time to respond. The prefilter, described at the beginning of this chapter, is working, but not as well as desired. The aircraft does not go unstable, but does take a few seconds to *winddown.* Figure 5.26 shows there is no affect on the horizontal separation distances from the change in altitude.

The responses for a 1000 ft decrease in altitude with linear cross coupling are shown in Figures 5.27 - 5.28. Recall from Sections 5.3 and 5.4, a change in heading with linear cross coupling caused a perturbation in the vertical channel. This case shows the reverse is true also. A change in altitude, with cross coupling included, leads to a minor oscillation in the heading. The $A_{4,5}$ term directly links the z separation into the heading autopilot. This is easily seen in the plot for the heading response. The heading is linked into the Mach hold autopilot and the x and y separations. This causes the small initial oscillations in the velocity and the x and y separation plots. The maximum y separation magnitude is 2×10^{-3} ft. Under real circumstances all of these effects would be drowned out by insignificant changes in air currents, but it is still interesting to see the simulation behave as expected. Overall, everything settles down in about 50 seconds with the exception of a little bit of chattering. The linear first order model ΔL and ΔD is not affected by a change in z. All the changes in ΔL and ΔD are caused by the change in heading which is caused by a change in sideforce, ΔF_Y, due primarily to the change in z separation, since the y separation is extremely small. Therefore, the affect of a change in z separation on the x-channel is only superficial and the affect on the y-channel is minor due to the simple first order model employed.

Figures 5.29 - 5.30 show the response for a decrease of 1000 ft in altitude with non-linear cross coupling. The inter-relationship between the z and y separations is much more obvious for this run than for the linearized run. The comparison between this run and the previous shows the x and y separation errors are much larger, highlighting the difference between the full non-linear model and the model with linear aerodynamic cross coupling. The y separation has a maximum error of 0.5 ft and a minimum error of -0.2 ft. The maximum x separation error is also much larger in magnitude, 0.1 ft. The y deviations are relatively small compared to the heading change cases, but larger than those from the velocity maneuver change cases. Recall from Figure 4.13, the change in sideforce, ΔF_Y, was not as dynamic as the change in drag for small changes in y separation. However, as seen in Figure 4.15 large changes in z separation can cause large changes in sideforce. A z separation of 6 ft leads to an increase in magnitude of ΔF_Y of 50%. Since ΔF_Y is negative it pushes the Wing away from the Lead, increasing the y separation. The y separation has a maximum magnitude of 1.1 ft. Since the nominal point sits on the knee of the curve as seen in Figure 4.13, ΔF_Y does not vary much for the 1.1 ft change in y separation. Therefore, in this case the effects of the change in z separation are greater than the effects from the change in y separation.

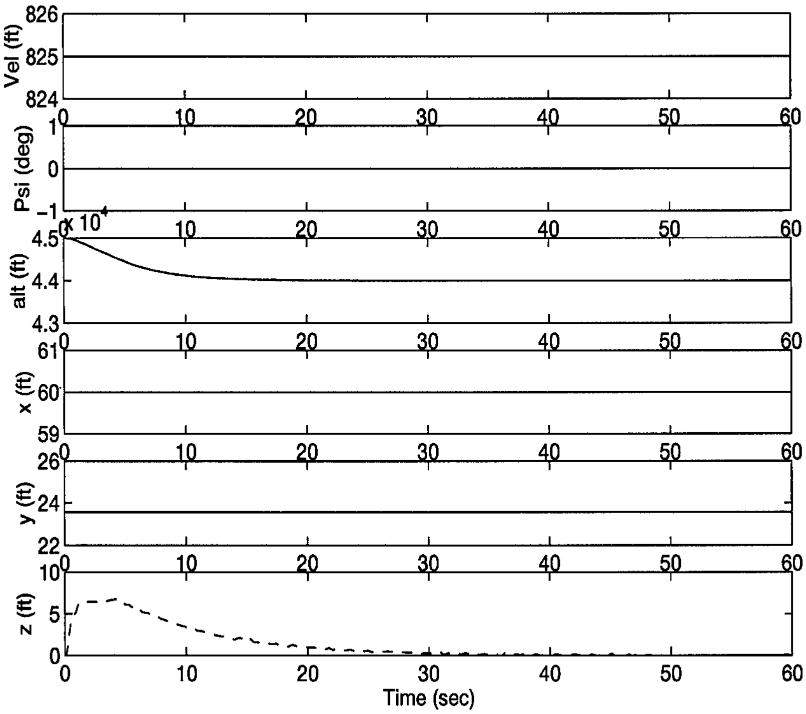

Figure 5.25 1000 ft Altitude Decrease Without Coupling Time Plot

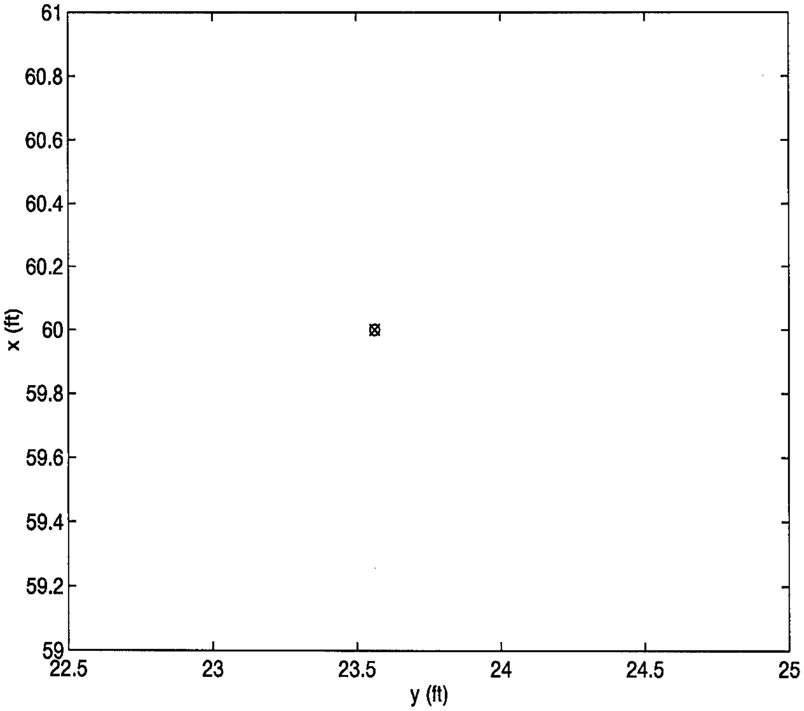

Figure 5.26 1000 ft Altitude Decrease Without Coupling Lissajous Plot

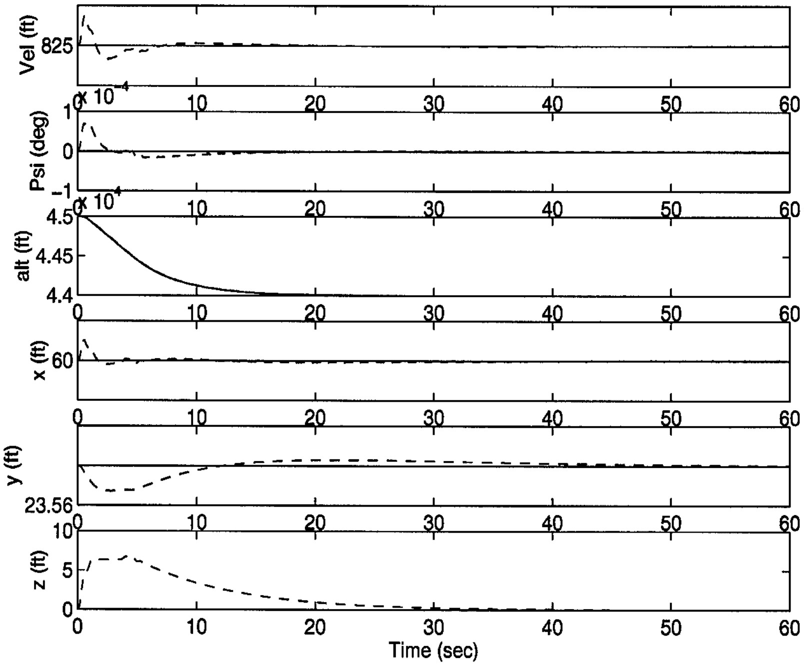

Figure 5.27 1000 ft Altitude Decrease With Linear Coupling Time Plot

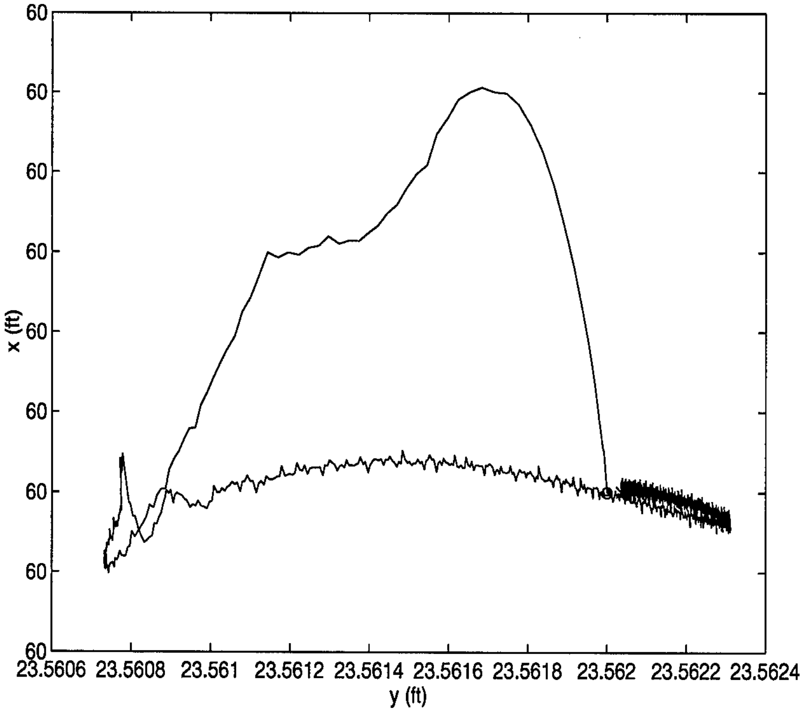

Figure 5.28 1000 ft Altitude Decrease With Linear Coupling Lissajous Plot

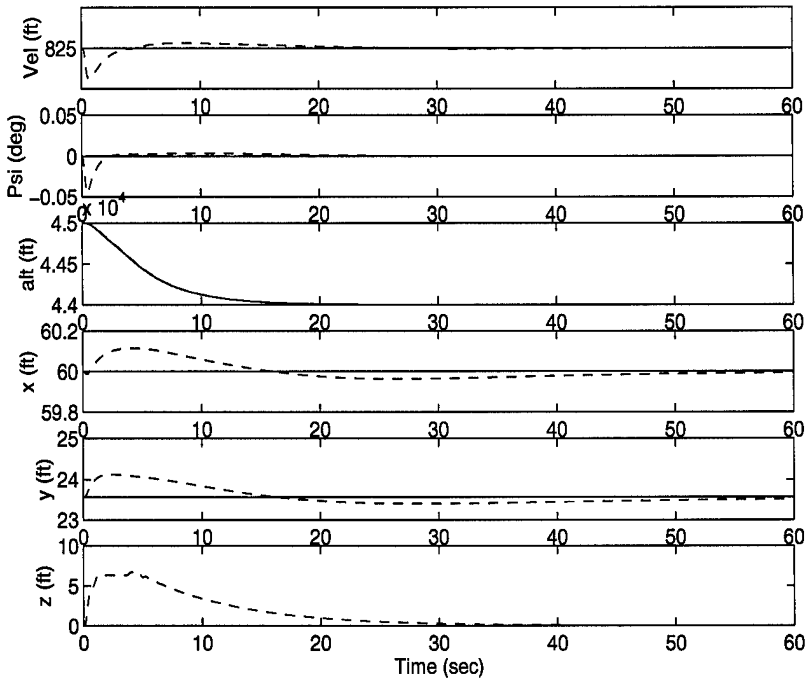

Figure 5.29 1000 ft Altitude Decrease With Non-Linear Coupling Time Plot

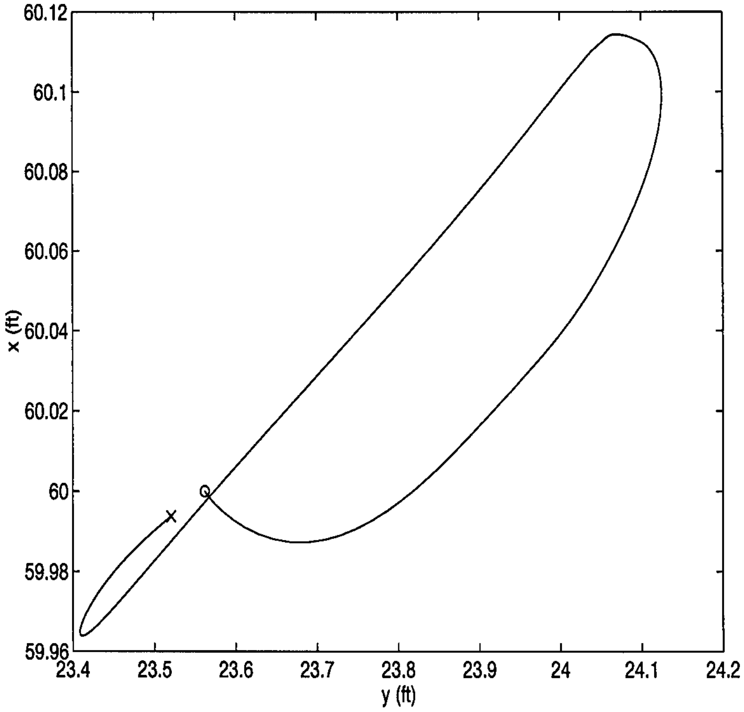

Figure 5.30 1000 ft Altitude Decrease With Non-Linear Coupling Lissajous Plot

5.7 1000 ft Altitude Increase

The formation is commanded a 1000 ft increase in altitude without coupling as shown in Figures 5.31 - 5.32. This case is almost identical to the previous except the direction for each term is opposite. The Wing tracks fairly closely, but does deviate from the Lead. This can be seen in the z time plot, which shows the vertical separation grows very quickly, levels off for a few seconds and then decreases. This maneuver saturates both the Lead and Wing altitude autopilots, but the Wing is saturated longer than the Lead. This is made better and worse by the upper limit on the FCS altitude hold autopilot. The magnitude of the upper limit is 1/3 less than the lower limit. The smaller limit causes the Lead autopilot to saturate faster, thereby not allowing the Lead to move farther away from the Wing. However, the lower saturation limit causes the vertical PI controller to windup for a longer period of time, causing a longer delay before the controller winds down and starts bringing the z separation back to the nominal value. This is easily seen in the z separation in which it is constant from 1 to 7 seconds, two seconds longer than in the 1000 ft altitude decrease case. There is no effect on the horizontal separation distances from the change in altitude. The reasons for this were described in the last section in the case of a 1000 ft altitude decrease.

Linear cross coupling causes some interesting results as in the previous case. The responses for this run are shown in Figures 5.33 and 5.34. A change in altitude with cross coupling included initially causes minor oscillations in the heading and velocity. The changes in heading and velocity lead to slight perturbations in the x and y separation distances. Overall, everything settles down in about 60 seconds. The x separation continues to oscillate, but the magnitude of the oscillation is on the order of nanofeet. The effects on the horizontal channels is again due to the coupling caused by the $A_{4,5}$ term.

Figures 5.35 - 5.36 show the response for an increase of 1000 ft in altitude with nonlinear cross coupling. As in the previous -1000 ft case with nonlinear cross coupling, the velocity and heading responses have an initial small oscillation. The y separation has a minimum error of -1.8 ft and a maximum error of 0.5 ft. Recall from the previous case, a z error of 6 ft resulted in an increase in sideforce of 50%. In this case, a z error of -6 ft results in a decrease of 130% causing the ΔF_Y to actually become slightly positive as seen in Figure 4.15. This strong positive ΔF_Y pulls the Wing toward the Lead causing the y separation to decrease. Since the ΔF_Y is stronger for a negative z change than for a positive z change this causes the maximum magnitude in y separation to be 0.7 ft greater between this run and the -1000 ft altitude with nonlinear coupling run. As expected, the maximum x separation error is larger in magnitude, 0.1 ft, than the linear run. Overall, all perturbations settle in about 60 seconds.

It is again apparent from Figures 5.25 - 5.36 that the results are consistent. The error in the z channel is about 6 ft for both an increase and decrease in altitude. The x and y changes also show some consistency between responses for an increase and decrease in altitude. Therefore, these results satisfy the second gain criteria of consistent results for positive and negative maneuver changes.

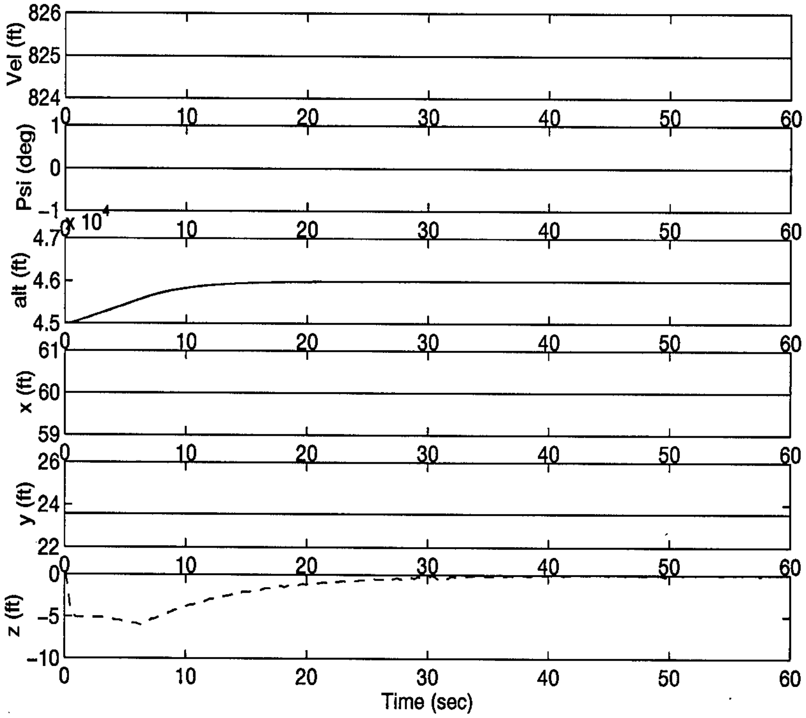

Figure 5.31 1000 ft Altitude Increase Without Coupling Time Plot

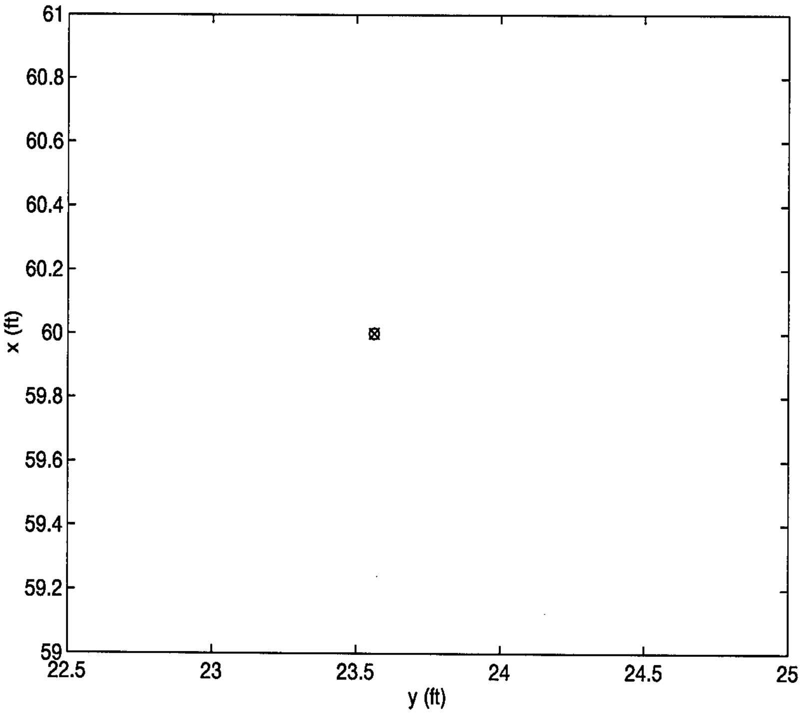

Figure 5.32 1000 ft Altitude Increase Without Coupling Lissajous Plot

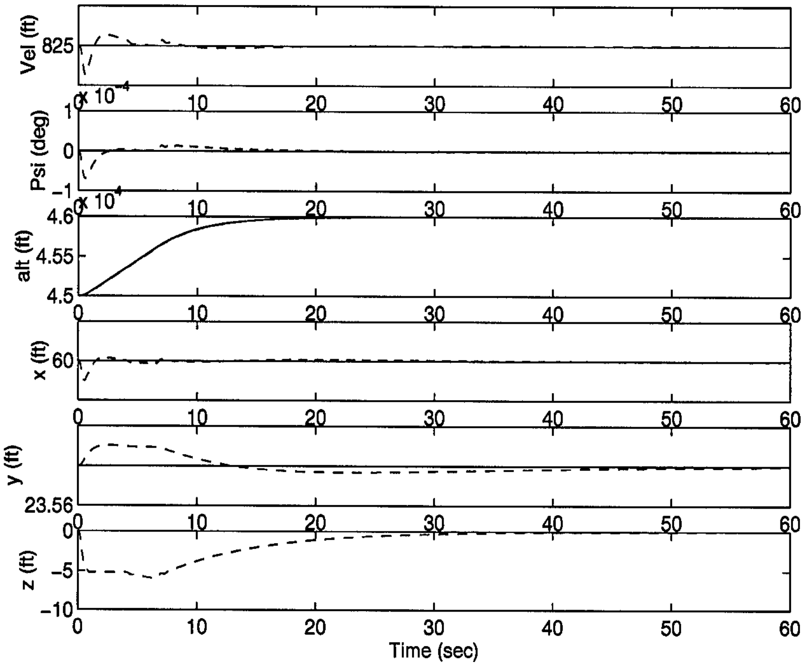

Figure 5.33 1000 ft Altitude Increase With Linear Coupling Time Plot

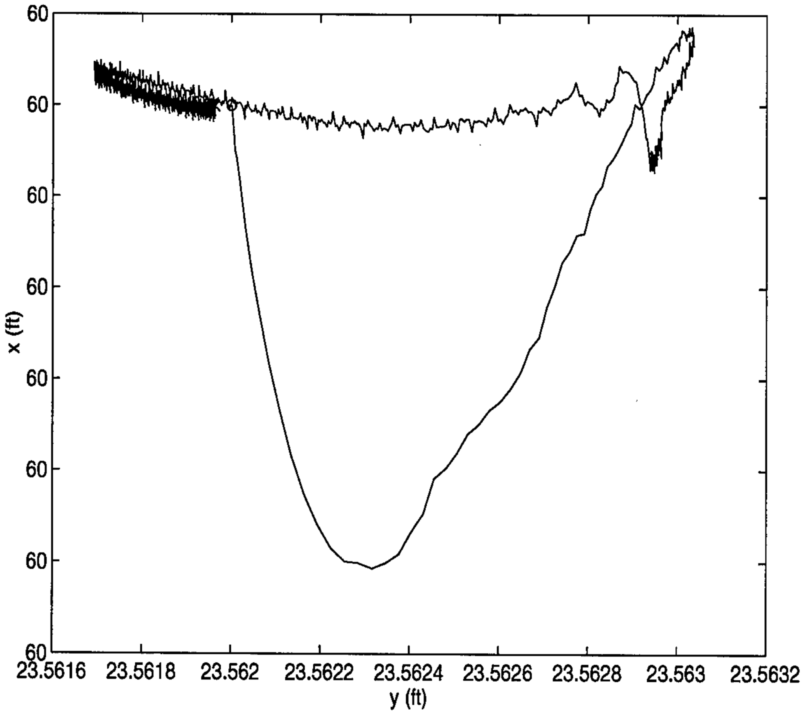

Figure 5.34 1000 ft Altitude Increase With Linear Coupling Lissajous Plot

5.8 Summary

Six cases were presented: +/-30° heading change, +/-50 ft/sec velocity change, and +/-1000 ft altitude change. Some observations not mentioned in the cases are presented: The FFC can maintain the formation within the 10% tolerance for y and z errors for a Lead heading change of +/-30°, +/-50 ft/sec velocity change, and +/-400 ft altitude change. The 400 ft altitude response was not shown in the cases. The +/-30° did not meet the 10%b tolerance for x error, but since the change in x is negligible this is not a requirement. However, a +/-20° heading change does meet the 10%b for x, y, and z errors. The responses were also shown to meet the gain criteria listed in Chapter IV.

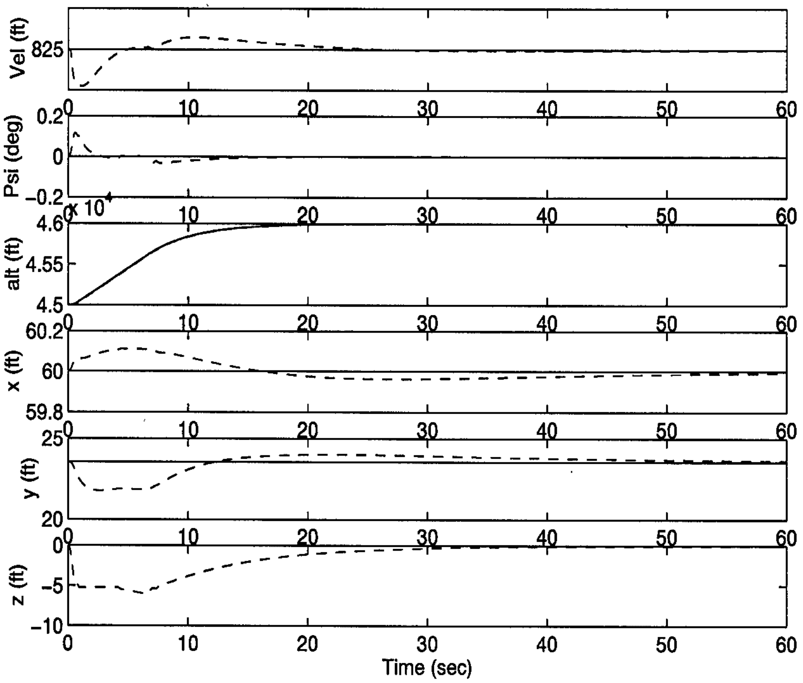

Figure 5.35 1000 ft Altitude Increase With Non-Linear Coupling Time Plot

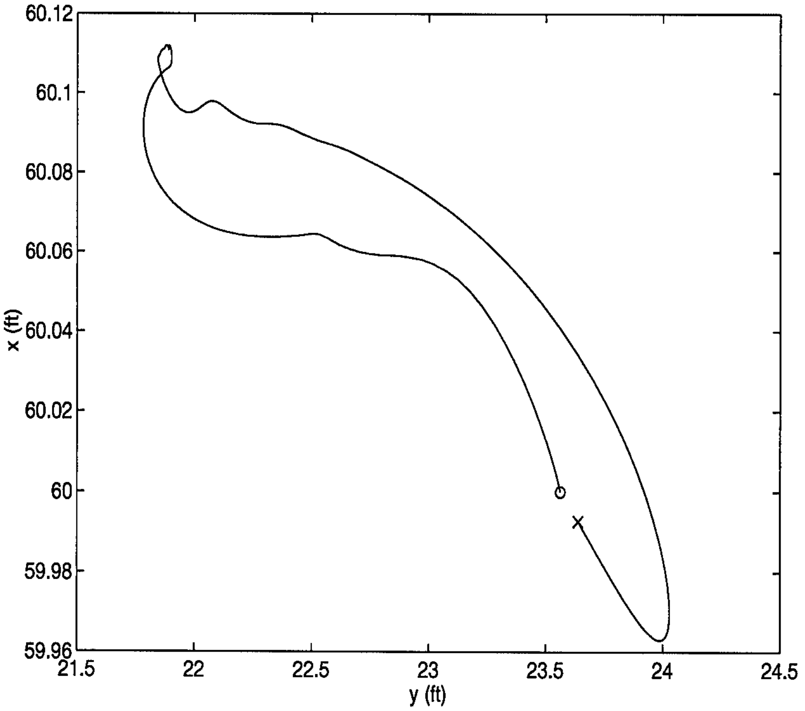

Figure 5.36 1000 ft Altitude Increase With Non-Linear Coupling Lissajous Plot

VI. Conclusion

6.1 Conclusions

The primary objective of this research was to determine if a large formation flight controller could be redesigned and applied to a close formation. The close formation flight controller designed in Chapter IV has met this objective.

The primary question to be answered by this research was to determine if a close formation flight controller designed without due consideration of the close formation aerodynamic coupling can handle the additional forces created by the close formation. The secondary question was to determine if the kinematic coupling is stronger than the aerodynamic cross coupling. The primary and secondary questions have also been answered through the stability and robustness analysis of Chapter IV and the results obtained in Chapter V.

The effects of close formation flight were derived and applied to the close formation flight controller. It was shown that the large formation flight controller, with the gains adjusted for a close formation, resulted in zero steady state tracking errors. The maximum tracking error in x separation was 4 ft ($\approx \frac{1}{7}b$), the maximum tracking error in the y separation was 3 ft ($\frac{1}{10}b$), and the maximum tracking error in the z separation was 6 ft ($\frac{1}{5}b$) for the envelope defined in the assumptions with the full non-linear kinematics and aerodynamic cross coupling included.

The criteria for gain selection was also met. The gain criteria are briefly summarized as: similar positive and negative perturbations for a heading change maneuver, similar results for a positive and negative maneuver change, and the Wing should not cross over the $\hat{x}$ or $\hat{y}$ axes. Consistent positive and negative deviations from nominal for a heading change maneuver satisfied the first gain criterion. The responses for a negative and positive heading and velocity maneuver change of equal magnitude were consistent; satisfying the second gain criterion. Finally, the Wing aircraft never crossed over either the $\hat{x}$ or $\hat{y}$ axes. Therefore, no collisions occurred and the third gain criterion was satisfied.

With the exception of the $A_{6,3}$ term, the kinematic coupling was generally at least two orders of magnitude greater than any aerodynamic induced cross coupling. The close formation flight controller developed without including aerodynamic cross coupling proved to be stable and robust. All eigenvalues for the closed loop system were shown to be in the left half plane. The overall responses from the system with the inclusion of the full nonlinear kinematics and aerodynamic effects were shown to be similar to the responses from the full nonlinear kinematics without the inclusion of the aerodynamic effects.

Finally, it was shown that the formation flight controller can maintain the formation geometry within the required 10% tolerance for y and z errors for a Lead heading change of +/-30°, a velocity change of +/-50 ft/sec, and an altitude change of +/-400 ft. Thus the close formation flight controller can enable aircraft to take advantage of the reduction in induced drag brought about by the aerodynamic coupling effects.

6.2 Recommendations for Further Study

- The models employed in this research were rather rudimentary. The prefilter was a simple first order lag and was identical for each channel. The FCS models were based on a point mass and did not include moment effects. The FCS C-130 models were modified to represent an F-16 class aircraft. More accurate Models should be developed to better represent a true F-16 class aircraft.
- Moment effects caused by the vortex should be developed. The effects of linearized and non-linear moments should be applied to the close FFC to determine if it is robust enough or whether it needs to be modified.
- If higher precision formation flight control is desired, it may be prudent to add sensor noise to the system and perform a stochastic based analysis using a Kalman filter to estimate the true location of the Lead with respect to the Wing in the formation. This will also promote fusing sensor data from a close formation of UAVs performing a surveillance mission in which each UAV has a different sensors.
- Implement the close formation flight controller in a digital controller.
- Incorporate anti-collision circuitry and analyze the effect.

6.3 Summary

The close formation aerodynamic coupling effects on the Wing aircraft caused by the Lead's wing vortex have been included in the formation flight control system dynamics. A close formation flight control system for the Wing aircraft was designed. It was shown that formation flight control system designs, accounting for kinematic coupling effects only, are robust and can handle the additional aerodynamic coupling effects caused by close formation flying. The developed close formation flight controller can enable aircraft to take advantage of benefits from the vortices created by the Lead aircraft in the formation. This can reduce the formations fuel consumption and extend formation range and endurance. This can also enable multiple aircraft or UAVs to fly together in a controlled close formation during

Appendix A. Appendix A

The F-16 characteristic data are contained in the Matlab data file, controlfile.m. The actual program is contained in the Matlab script, runsimc.m. The script loads the data file and then executes the simulations using the Simulink models. Two models are used the first is the linear state space model and the second is the complete linear/nonlinear block model. The linear simulation is used to perform initial analysis and design of the controller. This includes the gain selection described in Chapter IV. The full block simulation model is used to test the designed controller for stability and robustness and determine if the gains need to be adjusted.

A.1 Characteristic Data file

```
% controlfile.m
% PLEASE NOTE
% Second order MODELS with saturations most accurately follow true autopilots
% without saturations if the inputs are limited to 30 degree magnitude heading
% change; 40 ft/sec magnitude velocity change; 1000 ft magnitude altitude change
% More thorough methods will have to be employed if values greater than these
% are required.  They might include ramping of input or alteration of models
% based on better modeling methods as outlined in Russ Miller's dissertation

% NON-LINEAR or LINEAR

linear=1;
nonlin=-1;
%switch = linear

% THIS IS FIRST ORDER MODELS
% COMMANDS
% F-16 wingspan 30 ft
% Pi/4 X 30 = 23.6 ft
```

```
nominal_vel=825; % M=0.85 a=971
command_vel=825;
nominal_heading=0;
commanded_heading=0;
nominal_alt = 45000;
commanded_alt = 46000;
x_nominal= 60; % 2b nominal this one does not matter as much for upwash as does
x_command= 60;
y_nominal= 23.562; % (Pi/4 X 132)/2 nominal    this one, we also need a z component
y_command= 23.562;
z_nominal = 0;
z_command = 0;

% F-16 LEAD AIRCRAFT AUTOPILOT
% time constants
lead2_vel_time=5;
lead1_Tsi_time=1/3;
lead2_alta_time=0.3075;
lead2_altb_time=3.85;

% Lead Saturations
lead_accel_sat_low=-10;
lead_accel_sat_high=5;
lead_Tsi_sat_low=-6;
lead_Tsi_sat_high=6;
lead_alt_sat_low=-126;
lead_alt_sat_high=100;

% F-16 WING AIRCRAFT AUTOPILOT
```

```
% Time constants
wing2_vel_time=5;
wing1_Tsi_time=1/3;  %for a true second order model
wing2_alta_time=0.3075;
wing2_altb_time=3.85;

% Wing Saturations
wing_accel_sat_low=-10;
wing_accel_sat_high=5;
wing_Tsi_sat_low=-6;
wing_Tsi_sat_high=6;
wing_alt_sat_low=-126;
wing_alt_sat_high=100;

% Stability Derivatives and aircraft values F-16 class
weight_max=25000;
weight_avg=21500; % lbs half tank of fuel
weight_min=18000; % no fuel
AR=3; % aspect ratio
S=300; % sq ft area of wing
b=30; % ft wingspan
Svt=54.75; % sq ft
hz=10 ; % ft or 120 inches height of tail
aw=5.3 ; % per rad  wing lift curve slope
avt=5.3 ; % per rad  tail lift curve slope
eta=.95 ; % efficiency factor of tail
q=155.8; % lb/sq ft  dynamic pressure
mu=0.03; % upwash/sidewash correction factor
```

```
% DARGAN CONTROLLER

% LINEAR MIXER cur DAR
vel_error_gain=12.5; % 5
head_error_gain=6; % 10
x_pos_error_gain=-8; % 2
y_pos_error_gain=-0.6; % 1
z_pos_error_gain=25; % 0.5

% PI CONTROLLER
x_pro_gain=6; % 0.17 1.2
x_int_gain=0.4; % 0.02
y_pro_gain=11; % 0.5
y_int_gain=0.9; % 0.05
z_pro_gain=4.0; % 1.0
z_int_gain=0.5; % 0.5
```

A.2 Executable Program

```
clear

controlfile


def_time=60;

def_cont=1;

fig_num=0;

def_par=[];


% close old simulink controller if open

parms=get_param;

if parms == def_par;

;

else

close_system;

end


%simplify names of time constants

tv=lead2_vel_time;

tpsi=lead1_Tsi_time;

tha=lead2_alta_time;

thb=lead2_altb_time;


% simplify names of gains

Kv=vel_error_gain;

Kpsi=head_error_gain;

Kx=x_pos_error_gain;

Ky=y_pos_error_gain;

Kz=z_pos_error_gain;
```

```
% PI CONTROLLER
KXP=x_pro_gain;
KXI=x_int_gain;
KYP=y_pro_gain;
KYI=y_int_gain;
KZP=z_pro_gain;
KZI=z_int_gain;




prev=input('Do you want to close previous pictures 1 yes 0 no: ');
if prev == 1
close all;
hx=1;
hy=0;
else prev == 0
    prev=0;
    hx=1;
    hy=1;
end

cont=input('please choose 1 for current or 0 for previous : ');
if cont == 1
cd ../dargan/current;
XI=[0,0,0,0,0,0,0,0,0,0,0,0,0,0,0,0,0];
else cont == 0
cd ../dargan/old;
%XI=[0,0,0,0,0,0,0,0,0,0,0,0,0,0,0,0,0];
XI=[0,0,0,0,60,23.562,0,0,0,0,0,0,0,0,0,0,0,0,0];
```

```
choice=input('please choose 1 for linear or 0 for nonlinear kinematics: ');
if choice == 1;
kswitch = linear;
else choice == 0;
kswitch = nonlin;
end


choice=input('please choose 1 for linear or 0 for nonlinear disturbance: ');
if choice == 1;
dswitch = linear;
else choice == 0;
dswitch = nonlin;
end

V_dist_sw=input('Do you want a velocity disturbance, 1 yes 0 no: ');
H_dist_sw=input('Do you want a altitude disturbance, 1 yes 0 no: ');
Tsi_dist_sw=input('Do you want a heading disturbance, 1 yes 0 no: ');


end


'Calculate formation stability derivatives'
weight=weight_max;
Cl=weight/(q*S);
m=weight/32.2 ; %mass
bp=(pi*b)/4;

% TRUE CHANGE IN DRAG
```

```
% nominal
G=(2*Cl*nominal_vel*b)/(pi*AR);
W=G/(4*pi*bp)*(log((y_nominal^2 + z_nominal^2 + (b*mu)^2)/((y_nominal-bp)^2 +...
z_nominal^2 + (b*mu)^2))...
- log(((y_nominal+bp)^2 + z_nominal^2 + (b*mu)^2)/(y_nominal^2 +...
z_nominal^2 + (b*mu)^2)));
delta_C_D=Cl*W/nominal_vel;
D_nominal=q*S*delta_C_D/m


% TRUE CHANGE IN LIFT
% nominal
delta_C_D=aw*W/nominal_vel;
L_nominal=q*S*delta_C_D/m


% TRUE CHANGE IN SIDE FORCE
%nominal
V=G/(4*pi*hz)*(log(((y_nominal-bp/2)^2 + z_nominal^2 + (b*mu)^2)/((y_nominal-bp/2)^2 +...
(z_nominal+hz)^2 + (b*mu)^2))...
- log(((y_nominal+bp/2)^2 + z_nominal^2 + (b*mu)^2)/((y_nominal+bp/2)^2 +...
(z_nominal+hz)^2 + (b*mu)^2)));
delta_C_Y=eta*Svt*avt*V/(S*nominal_vel);
Tsi_nominal=q*S*delta_C_Y/m

% velocity
delta_C_D_W_y=(1/(pi*AR))*(Cl^2)*(1/b)*((3/8)*pi/[((pi/4)^2+mu^2)*((pi/2)^2+mu^2)]);

% altitude
delta_C_L_W_y=aw*Cl*(3/8)*pi/[pi*AR*b*((pi/4)^2+mu^2)*((pi/2)^2+mu^2)];
```

```
% heading
C_Y_W_y_first=hz^2/[2*b^2*((pi/8)^2+mu^2)*((pi/8)^2+(hz/b)^2+mu^2)];
C_Y_W_y_sec=3*hz^2/[2*b^2*((3*pi/8)^2+mu^2)*((3*pi/8)^2+(hz/b)^2+mu^2)];
C_Y_W_y_inner=C_Y_W_y_first-C_Y_W_y_sec;
delta_C_Y_W_y=eta*Svt*avt*Cl*C_Y_W_y_inner/(pi*AR*2*S*hz);

delta_C_Y_W_z=-(eta*Svt*avt*Cl*32*hz*pi^2)/(pi*AR*2*S*pi*b^2*8^2*...
[((pi/8)^2+mu^2+(hz/b)^2)*((3*pi/8)^2+mu^2+(hz/b)^2)]);

if cont == 1
lindis=input('please choose 1 for disturb or 0 for nodisturb : ');
if lindis == 1
% STATE SPACE MODELS
% A with disturbances
A=[0 -1 [(q*S/(m*nominal_vel))*(delta_C_Y_W_y*y_nominal)] [-(y_nominal/wing1_Tsi_time)*(p
0 [-(1/wing2_vel_time)] [(q*S/m)*(delta_C_D_W_y)] 0 0 0;
0 0 [-(q*S/(m*nominal_vel))*(delta_C_Y_W_y*x_nominal)] [((x_nominal/wing1_Tsi_time - nomi
0 0 [(q*S/(m*nominal_vel))*(delta_C_Y_W_y)*(180/pi)] [-(1/wing1_Tsi_time)] [(q*S/(m*nomin
0 0 0 0 0 1;
0 0 [(q*S/m)*(delta_C_L_W_y)] 0 [-1/(wing2_alta_time*wing2_altb_time)] -[(1/wing2_alta_ti

else lindis == 0
% A without disturbances
A=[0 -1 0 [-(y_nominal/wing1_Tsi_time)*(pi/180)] 0 0;
0 [-(1/wing2_vel_time)] 0 0 0 0;
0 0 0 [((x_nominal/wing1_Tsi_time - nominal_vel))*(pi/180)] 0 0;
0 0 0 [-(1/wing1_Tsi_time)] 0 0;
0 0 0 0 0 1;
0 0 0 0 [-1/(wing2_alta_time*wing2_altb_time)] -[(1/wing2_alta_time) + (1/wing2_altb_time
```

```
end

end

% Input Matrix

b1=[0 [(y_nominal/wing1_Tsi_time)*(pi/180)] 0;

[1/wing2_vel_time] 0 0;

0 [-(x_nominal/wing1_Tsi_time)*(pi/180)] 0;

0 [(1/wing1_Tsi_time)] 0;

0 0 0;

0 0 [1/(wing2_alta_time*wing2_altb_time)]];

% Disturbance Matrix

b2=[1 0 0;

0 0 0;

0 nominal_vel*(pi/180) 0;

0 0 0;

0 0 0;

0 0 -[1/(wing2_alta_time*wing2_altb_time)]];

B=[b1 b2];

C=[1 0 0 0 0 0;

0 1 0 0 0 0;

0 0 1 0 0 0;

0 0 0 1 0 0;

0 0 0 0 1 0];

D=[0 0 0 0 0 0;

0 0 0 0 0 0;
```

```
0 0 0 0 0 0;
0 0 0 0 0 0;
0 0 0 0 0 0];


I=[0 0 0 0 0 0]';



% Closed Loop plant
G=pi/180;
a1=[0 -1 y_nominal*((q*S*delta_C_Y_W_y/(m*nominal_vel)) - G*KYP*Ky/tpsi) -(G/tpsi)*y_nomi
(q*S/(m*nominal_vel))*(y_nominal*delta_C_Y_W_z) 0 0 y_nominal*KYI*G/tpsi 0];
a2=[-KXP*Kx/tv -(1/tv)*(1 + KXP*Kv) (q*S/m)*delta_C_D_W_y 0 0 0 KXI/tv 0 0];
a3=[0 0 x_nominal*(G*KYP*Ky/tpsi - (q*S/(m*nominal_vel))*delta_C_Y_W_y) ...
G*(x_nominal/tpsi -nominal_vel + x_nominal*KYP*Kpsi/tpsi) ...
-x_nominal*(q*S/(m*nominal_vel))*delta_C_Y_W_z 0 0 -x_nominal*KYI*G/tpsi 0];
a4=[0 0 (-KYP*Ky/tpsi + (q*S/(m*nominal_vel*G))*delta_C_Y_W_y) -(1/tpsi)*(1+KYP*Kpsi) ...
(q*S/(m*nominal_vel))*delta_C_Y_W_z/G 0 0 KYI/tpsi 0];
a5=[0 0 0 0 0 1 0 0 0];
a6=[0 0 (q*S/m)*delta_C_L_W_y 0 -(1/(tha*thb))*(KZP*Kz + 1) -(1/tha + 1/thb) 0 0 KZI/(tha
a7=[-Kx -Kv 0 0 0 0 0 0 0];
a8=[0 0 -Ky -Kpsi 0 0 0 0 0];
a9=[0 0 0 0 -Kz 0 0 0 0];

Acl=[a1;a2;a3;a4;a5;a6;a7;a8;a9];
eig(Acl)

open_system controller
cd ../../test/;
```

```
time=input('please enter time for simulation in increments of 10 seconds :');
if time == 0;
time = def_time;
else
    time = time*10;
end

% Set initial state values
%x1 = [0;nominal_vel;nominal_vel;x_nominal;y_nominal;0;0]
%;nominal_heading;nominal_vel;nominal_heading]
%x2 = [0;nominal_vel;0;0;0;nominal_alt;nominal_alt];
%x3= [];
%XI = [x1;x2];
max_error=1e-3;
min_step=time/1000;
max_step=time/1000;

%[t,x,y]=rk45('controller',time,XI,[max_error,min_step,max_step]);
%[t,x,y]=rk45('controller',time);
%[t,x,y]=rk45('cont_generic',time);
[t,x,y]=adams('controller',time);
%[t,x,y]=rk45('controller',time,XI,[max_error,min_step,max_step]);

% velocities of lead and wing
set(figure,'Position',[560*(hx-1),480-480*hy,560 460]);
subplot(6,1,1), plot(t,y(:,3),'-');
subplot(6,1,1), ylabel('Vel (ft)');
hold;
subplot(6,1,1), plot(t,y(:,5),'c--');
```

```
% headings of lead and wing
subplot(6,1,2), plot(t,y(:,4),'-');
subplot(6,1,2), ylabel('Psi (deg)');
hold;
subplot(6,1,2), plot(t,y(:,6),'c--');

% lead altitude
subplot(6,1,3), plot(t,y(:,12),'-');
hold
% wing altitude
subplot(6,1,3), plot(t,y(:,13),'c--');
subplot(6,1,3), ylabel('alt (ft)');

% x seperation
subplot(6,1,4), plot(t,y(:,1),'c--');
hold;
subplot(6,1,4), line(t,x_nominal.*ones(size(t)));
subplot(6,1,4), ylabel('x (ft)');
% y seperation
subplot(6,1,5), plot(t,y(:,2),'--c');
hold;
subplot(6,1,5), line(t,y_nominal.*ones(size(t)));
subplot(6,1,5), ylabel('y (ft)');
% z seperation
subplot(6,1,6), plot(t,y(:,11),'--c');
hold
subplot(6,1,6), plot(t,z_nominal.*ones(size(t)));
subplot(6,1,6), ylabel('z (ft)');
```

```
xlabel('Time (sec)');

hx=hx+1;
last_y=size(y,1);
set(figure,'Position',[560*(hx-1),480-480*hy,560 460]);
plot(y(:,2),y(:,1));
hold on
plot(y(1,2),y(1,1),'o');
hold on
plot(y(last_y,2),y(last_y,1),'x');
ylabel('x (ft)');
xlabel('y (ft)');

a=x;

% TRUE CHANGE IN DRAG
% nominal
G=(2*Cl*nominal_vel*b)/(pi*AR);
W=G/(4*pi*bp)*(log((y_nominal^2 + z_nominal^2 + (b*mu)^2)/((y_nominal-bp)^2 +...
z_nominal^2 + (b*mu)^2))...
- log(((y_nominal+bp)^2 + z_nominal^2 + (b*mu)^2)/(y_nominal^2 +...
z_nominal^2 + (b*mu)^2)));
delta_C_D=Cl*W/nominal_vel;
D_w_nom=q*S*delta_C_D/m;

% final
G=(2*Cl*command_vel*b)/(pi*AR);
W=G/(4*pi*bp)*(log((y_command^2 + z_command^2 + (b*mu)^2)/((y_command-bp)^2 +...
z_command^2 + (b*mu)^2))...
- log(((y_command+bp)^2 + z_command^2 + (b*mu)^2)/(y_command^2 +...
```

```
z_command^2 + (b*mu)^2)));
delta_C_D=Cl*W/command_vel;
D_w_com=q*S*delta_C_D/m;

% change in drag
delta_diff=(D_w_com-D_w_nom)
```

A.3 Linear Simulation Model

The linear model, shown in Figure A.1 is the State-space representation of the system described in section 4.1 and described by Equations (4.13) - (4.16). The commands input to the Lead are: commanded_velocity-nominal_velocity, commanded_heading-nominal_heading, and commanded_alt-nominal_alt.

The individual blocks that make up the linear model are described. The Wing&kinematic&vortex block is the state space system described by Equations (4.13) - (4.16). The command prefilter block, Figure A.2 contains the prefilter discussed in Chapter V. The FFC controller is made up of the linear mixer block described in Figure A.5 and the PI controller, Figure A.6 described in Chapters II and IV. The Lead aircraft, Figure A.3 is composed of the flight control system detailed in Chapter II. Finally, the Perts+nominals block, Figure A.4 is used to add the nominal settings back to the perturbations to obtain the actual separation distances.

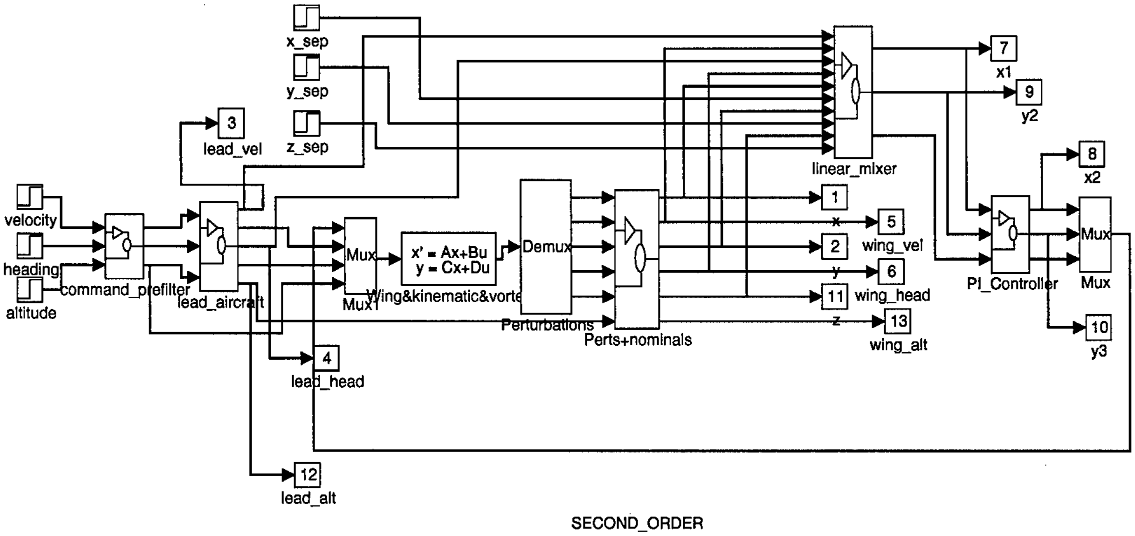

Figure A.1 Linear State Space Matlab Simulation Model

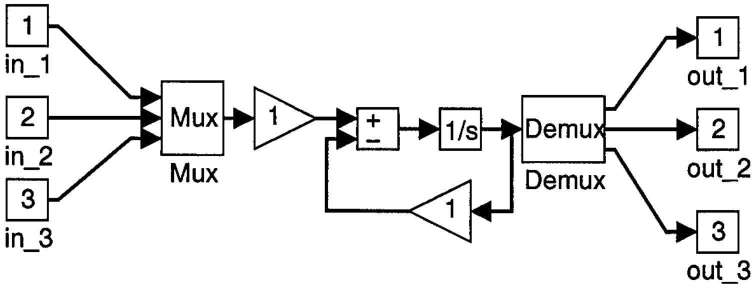

Figure A.2 Command Prefilter Simulation Model

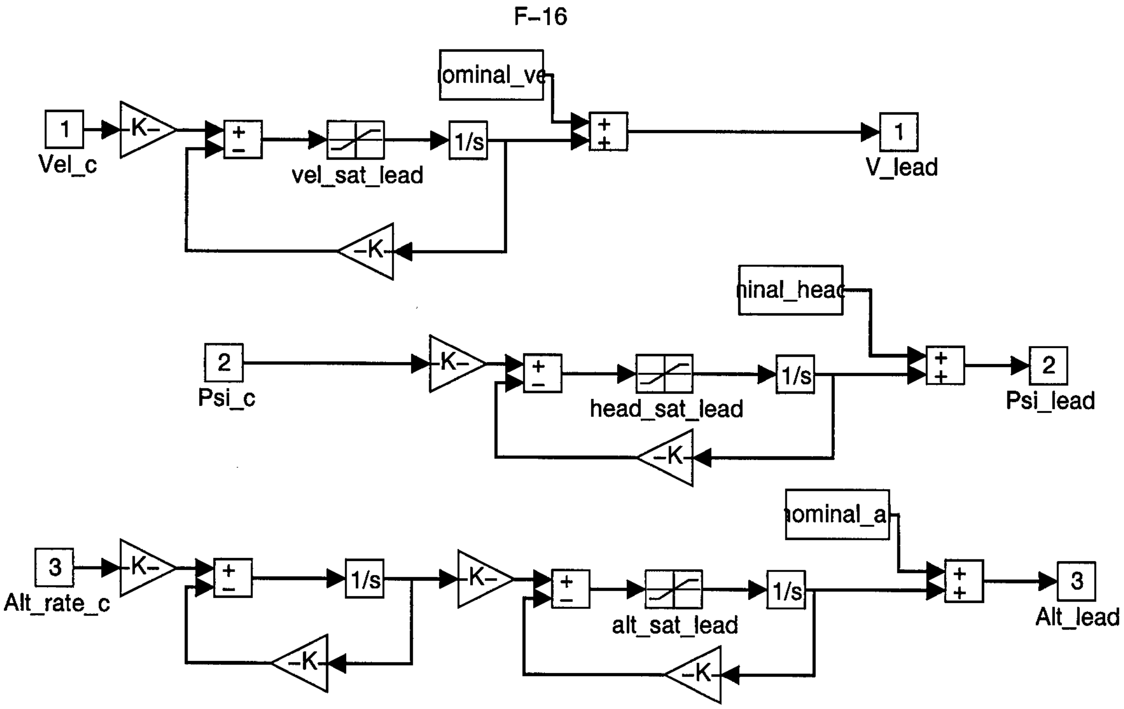

Figure A.3 Lead Aircraft Flight Control System Model

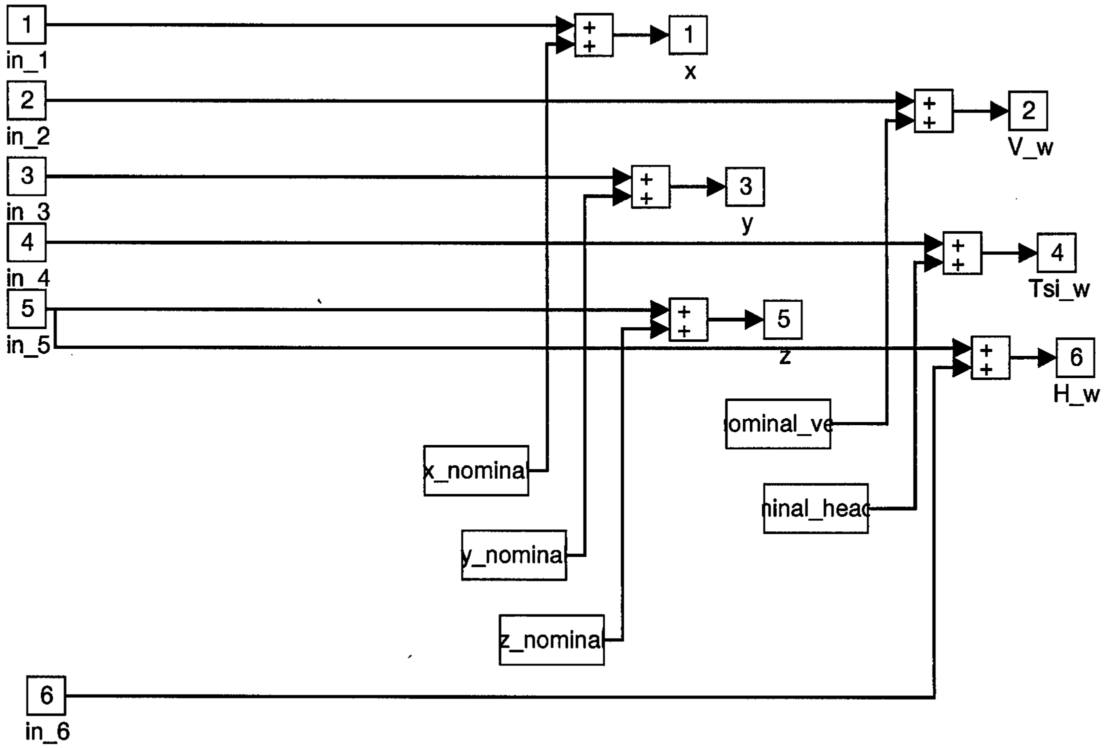

Figure A.4 Perturbation+Nominal Block

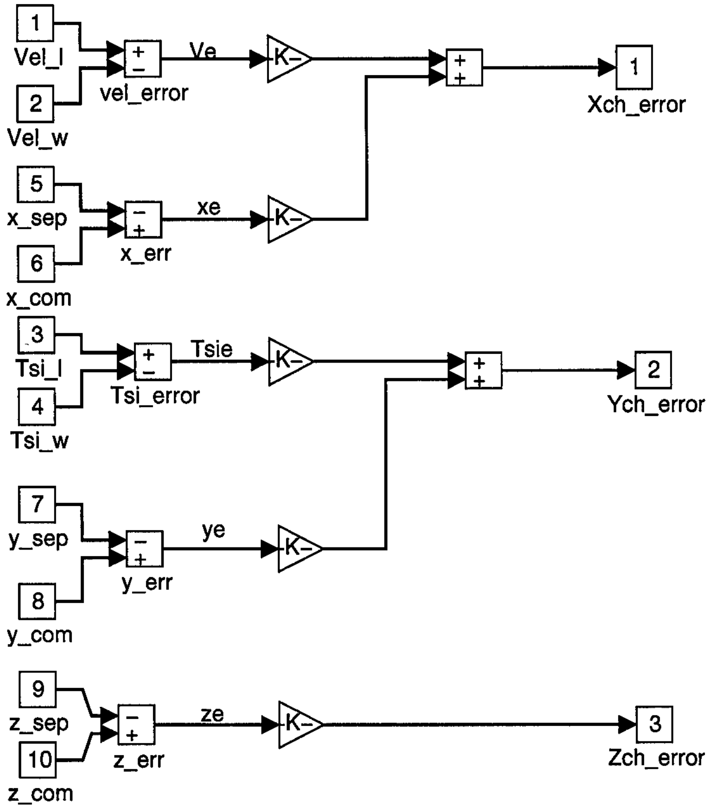

Figure A.5 Linear Mixer Simulation Model

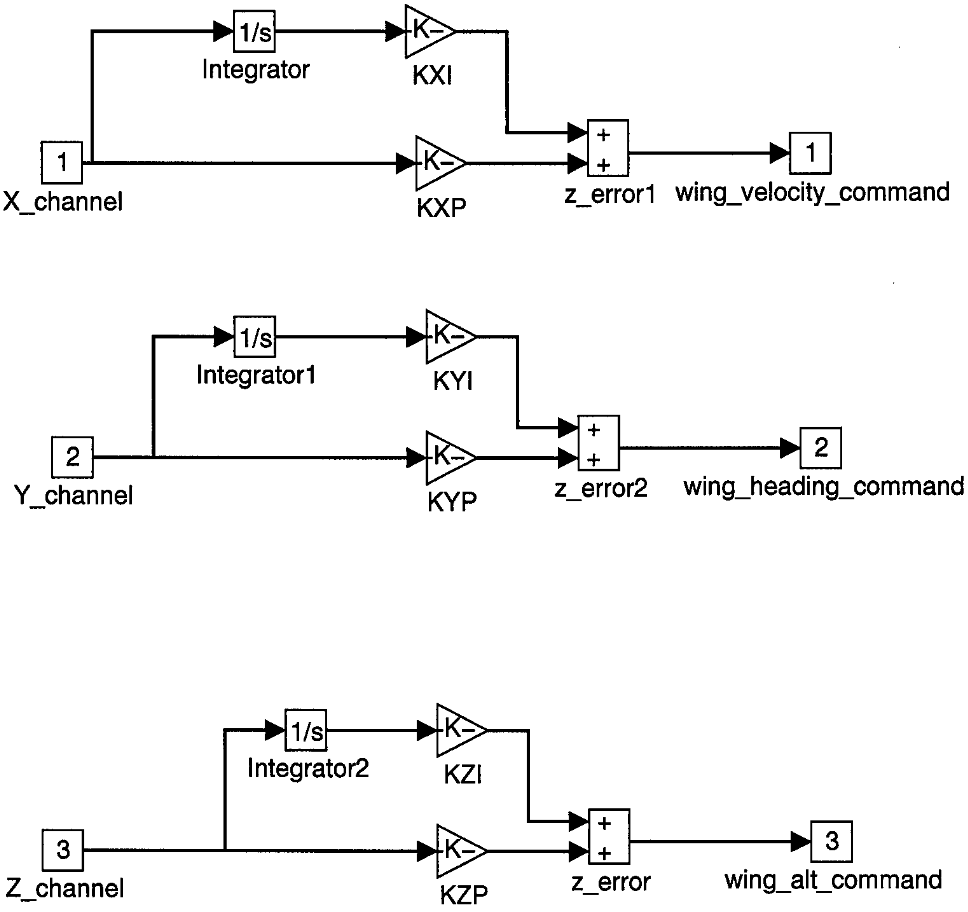

Figure A.6 PI Controller Simulation Model

A.4 Non-Linear Simulation Model

The full block simulation model is shown in Figures A.7 - A.10. The prefilter, linear mixer, PI controller, and lead aircraft blocks are the same as those used in the linear model above. The Kinematic and Horseshoe Vortex simulation blocks contain both the linear models and the non-linear models, Figures A.9 and A.10 respectively. The full nonlinear model was discussed in section 4.5. The wing aircraft, Figure A.8 is the same as the Lead except the disturbances are added to the respective autopilots they affect.

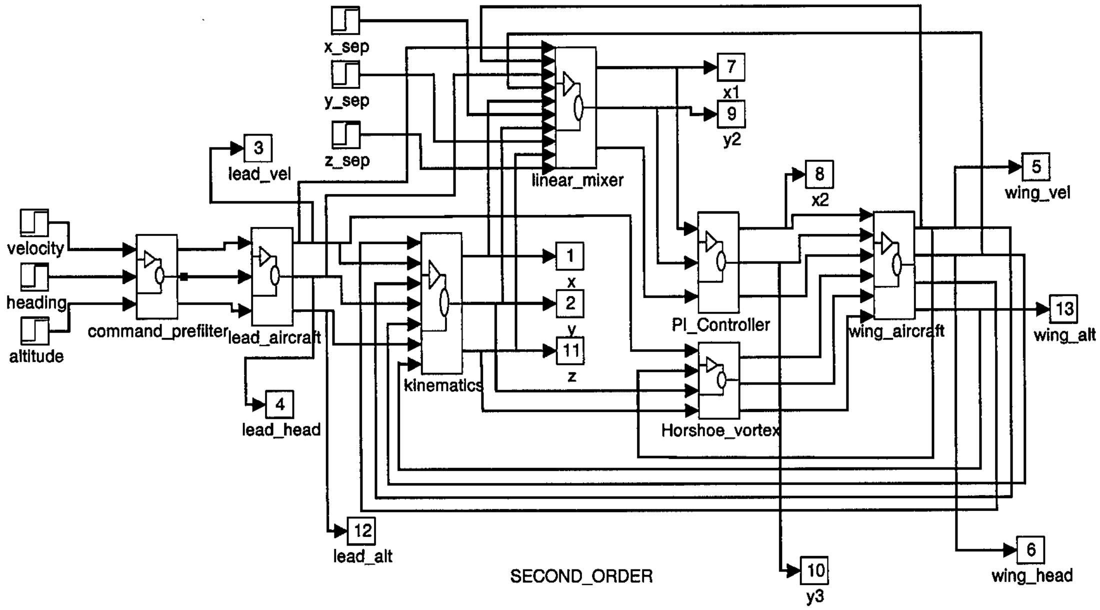

Figure A.7 Matlab Block Simulation Model

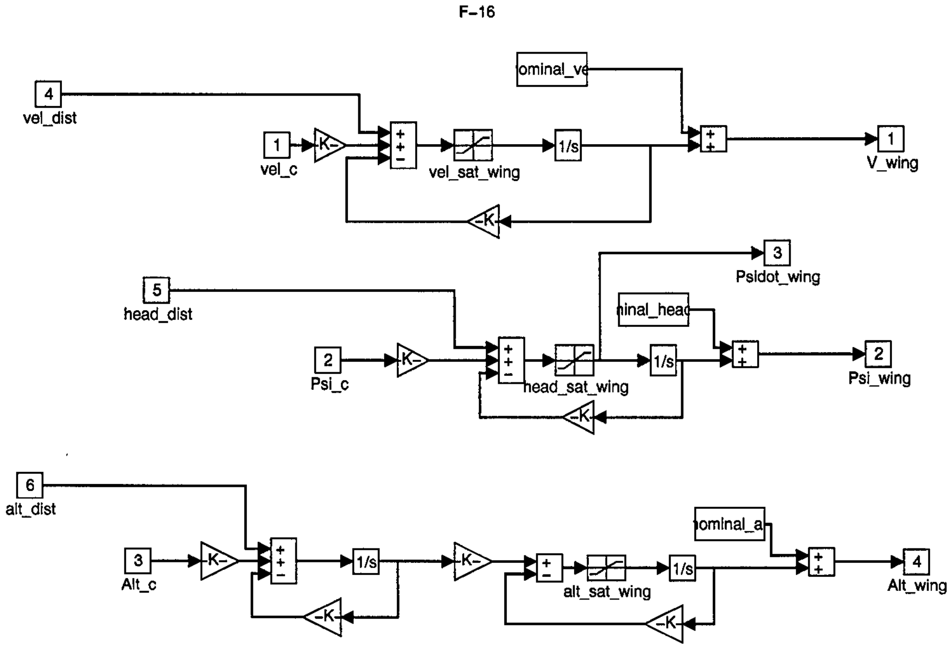

Figure A.8 Wing Aircraft Flight Control System Model

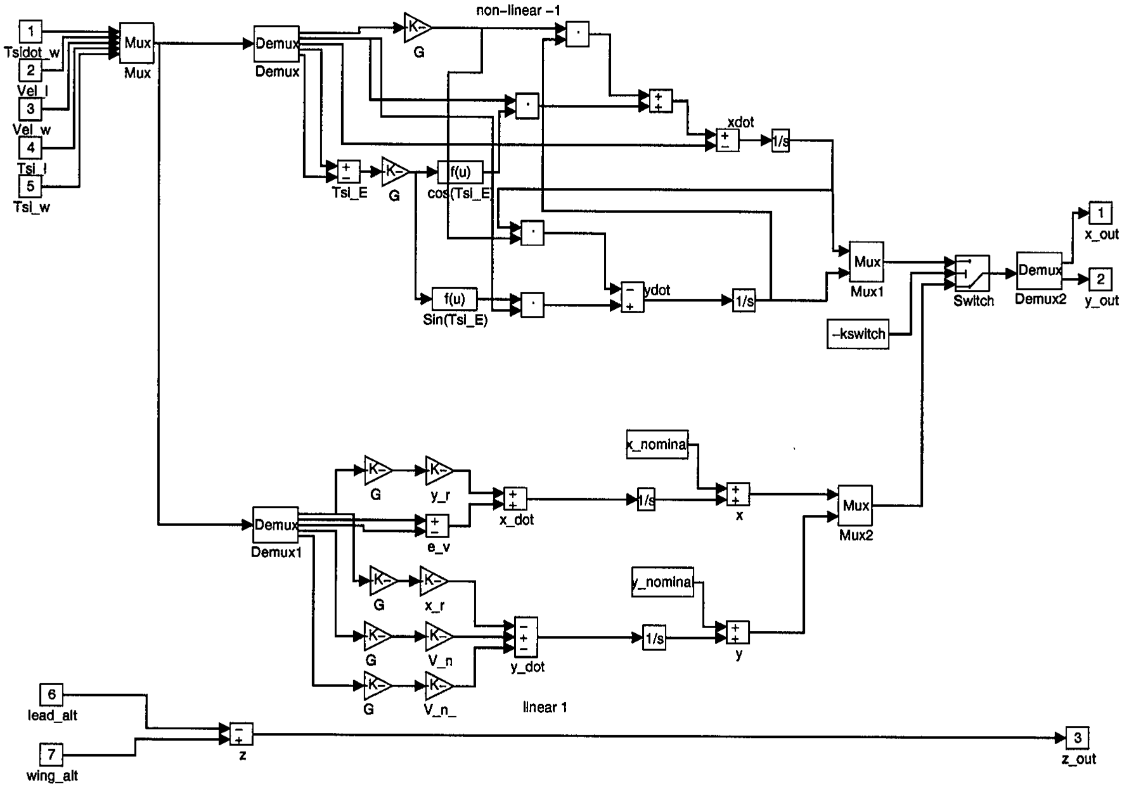

Figure A.9 Kinematic Motion Simulation Model

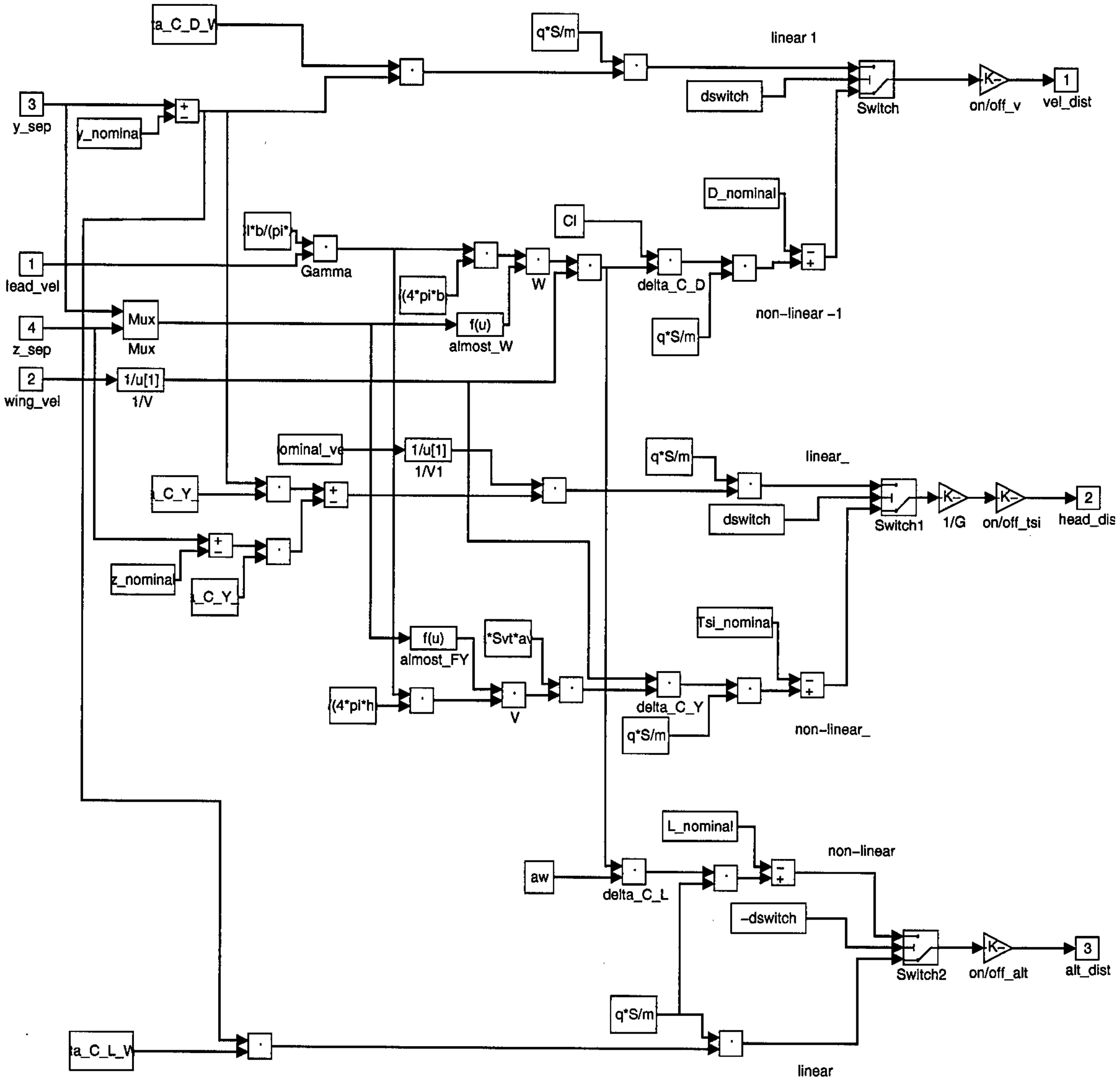

Figure A.10 Horshoe Vortex Disturbance Simulation Model

Bibliography

1. Buzogany, Louis E., *Automated Control of Aircraft in Formation Flight*, MS thesis, AFIT/GE/ENG/92D-07, School of Engineering, Air Force Institute of Technology (AU), Wright-Patterson AFB OH, December 1992.
2. Buzogany, Louis E., M. Pachter and J.J. D'Azzo, *Automated Control of Aircraft in Formation Flight*, Proceedings of the 1993 AIAA Guidance, Navigation, and Control Conference, pp 1349 - 1369, Monterey, CA, August 1993.
3. Dargan, John L., *Proportional Plus Integral Control of Aircraft for Automated Maneuvering Formation Flight*, MS thesis, AFIT/GE/ENG/91D-14, School of Engineering, Air Force Institute of Technology (AU), Wright-Patterson AFB OH, December 1991.
4. Dargan, John L., M. Pachter and J.J. D'Azzo, *Automatic Formation Flight Control*, Proceedings of the 1992 AIAA Guidance, Navigation, and Control Conference, pp 838 - 857, Hilton Head, SC, June 1992.
5. D'Azzo, John J. and Constantine H. Houpis, *Linear Control System Analysis and Design* (Fourth Edition), McGraw-Hill Book Company, 1995.
6. McCammish, Sean J., *Advanced Formation Flight Control*, MS thesis, AFIT/GE/ENG/95D-16, School of Engineering, Air Force Institute of Technology (AU), Wright-Patterson AFB OH, December 1995.
7. Miller, Russel B., *Manual Tracking Flight Control with Amplitude and Rate Constrained Dynamic Actuators*, PhD Dissertation, AFIT/DS/ENG/96-15, School of Engineering, Air Force Institute of Technology (AU), Wright-Patterson AFB OH, December 1996.
8. Pachter, M., J.L. Dargan, and J.J. D'Azzo, *Automatic Formation Flight Control*, AIAA Journal of Guidance, Control, and Dynamics, Vol 17, No. 6, May 1994.
9. Reyna, Vincent P., *Automation of Formation Flight Control*, MS thesis, AFIT/GE/ENG/94M-01, School of Engineering, Air Force Institute of Technology (AU), Wright-Patterson AFB OH, March 1994.
10. Reyna, Vincent P., *Formation Flight Control Automation*, Proceedings of the 1994 AIAA Guidance, Navigation, and Control Conference, pp 1379-1404, Scottsdale, AZ, August 1994.
11. Rohs, Paul R., *A Fully Coupled, Automated Formation Control System for Dissimilar Aircraft in Maneuvering, Formation Flight*, MS thesis, AFIT/GE/ENG/91M-03, School of Engineering, Air Force Institute of Technology (AU), Wright-Patterson AFB OH, March 1991.
12. Veth, Michael J., *Advanced Formation Flight Control*, MS thesis, AFIT/GE/ENG/94D-30, School of Engineering, Air Force Institute of Technology (AU), Wright-Patterson AFB OH, December 1994.
13. Blake, W., Dieter Multhopp, *Design, Performance And Modeling Considerations For Close Formation Flight*, AIAA Journal of Guidance, Control, and Dynamics, AIAA-98-4343, August 1998.
14. Pachter, Meir, Proffessor, Electrical Engineering, Personal interviews and Notes, Air Force Institute of Technology, Wright-Patterson AFB OH, Jan 1999.

15. Blakelock, John H., *Automatic Control of Aircraft and Missiles* (Second Edition), John Wiley & Sons, Inc., 1991.
16. Nelson, Robert C., *Flight Stability and Automatic Control* (Second Edition), McGraw-Hill, 1998.
17. *Matlab Simulink: Dynamic Simulation Software* , The MathWorks, Inc., 1994.
18. Park, Chil Ho, Korean Air Forces F-4 Pilot, Republic of Korea, Personal interview, Air Force Institute of Technology, Wright-Patterson AFB OH, Oct 1998.
19. Zumwalt, Michael, U.S. Air Force C-141 Pilot, WPAFB, Personal interview, Air Force Institute of Technology, Wright-Patterson AFB OH, Oct 1998.

REPORT DOCUMENTATION PAGE

Form Approved
OMB No. 0704-0188

1. AGENCY USE ONLY *(Leave blank)*

2. REPORT DATE
March 1999

3. REPORT TYPE AND DATES COVERED
Master's Thesis

4. TITLE AND SUBTITLE
CLOSE FORMATION FLIGHT CONTROL

5. FUNDING NUMBERS

6. AUTHOR(S)
Andrew W. Proud
Captain, USAF

7. PERFORMING ORGANIZATION NAME(S) AND ADDRESS(ES)
Air Force Institute of Technology
2950 P Street
Wright-Patterson AFB, OH 45433-6583

8. PERFORMING ORGANIZATION REPORT NUMBER
AFIT/GE/ENG/99M-24

9. SPONSORING/MONITORING AGENCY NAME(S) AND ADDRESS(ES)
Mr William Blake
AFRL/VAAD
2210 8th Street
Wright-Patterson AFB, OH 45433

10. SPONSORING/MONITORING AGENCY REPORT NUMBER

11. SUPPLEMENTARY NOTES
Dr. Meir Pachter
255-3636 x4593
meir.pachter@afit.af.mil

12a. DISTRIBUTION AVAILABILITY STATEMENT
Approved for public release; Distribution Unlimited

12b. DISTRIBUTION CODE

13. ABSTRACT *(Maximum 200 words)*

In this paper the close formation flight control problem is addressed. The formation consists of a lead and wing aircraft, where the wing flies in close formation with the lead, such that the lead's vortices produce aerodynamic coupling effects, and a reduction in the formation's drag is achieved. A controller, i.e., a formation-hold autopilot for the wing aircraft, is designed such that the formation's geometry is maintained in the face of lead aircraft maneuvers. In the formation flight control system, the wing and lead aircraft dynamics are coupled due to kinematic effects, and, in the case of close formations, additional aerodynamic coupling effects are introduced. In the paper these additional aerodynamic coupling effects are properly modeled. The most significant aerodynamic coupling effect introduced by close formation flight entails the coupling of the lateral/directional channel into the altitude-hold autopilot channel. It is shown that formation hold autopilots designed ignorin the aerodynamic coupling effects yield satisfactory performance in close formation flight.

14. SUBJECT TERMS
Close Formation Flight Control, Formation Auto-pilot, Formation Autopilot, F-16, Flight Control, Horseshoe Vortex, UAV

15. NUMBER OF PAGES
146

16. PRICE CODE

17. SECURITY CLASSIFICATION OF REPORT	**18. SECURITY CLASSIFICATION OF THIS PAGE**	**19. SECURITY CLASSIFICATION OF ABSTRACT**	**20. LIMITATION OF ABSTRACT**
UNCLASSIFIED	UNCLASSIFIED	UNCLASSIFIED	UL

Standard Form 298 (Rev. 2-89) (EG)
Prescribed by ANSI Std. 239.18
Designed using Perform Pro, WHS/DIOR, Oct 94